The Impact of Diabatic Heating on Jet Variability and Shift

A Dissertation Presented

by

Xiaoming Xia

To

The Graduate School

in Partial Fulfillment of the

Requirements

For the Degree of

Doctor of Philosophy

in

Marine and Atmospheric Sciences

Stony Brook University

December 2012

Stony Brook University

The Graduate School

Xiaoming Xia

We, the dissertation committee for the above candidate for the

Doctor of Philosophy degree, hereby recommend

acceptance of this dissertation.

Dr. Edmund K.M. Chang – Dissertation Advisor
Professor, School of Marine and Atmospheric Sciences

Dr. Sultan Hameed – Chairperson of Defense
Professor, School of Marine and Atmospheric Sciences

Dr. Minghua Zhang – Member
Dean and Professor, School of Marine and Atmospheric Sciences

Dr. Dong-Ping Wang – Member
Professor, School of Marine and Atmospheric Sciences

Dr. Kyle Swanson – Member
Professor, Atmospheric Science Group/Dept. Math Sci.
University of Wisconsin-Milwaukee

This dissertation is accepted by the Graduate School

Charles Taber

Interim Dean of the Graduate School

Abstract of the Dissertation

The Impact of Diabatic Heating on Jet Variability and Shift

by

Xiaoming Xia

Doctor of Philosophy

in

Marine and Atmospheric Science

Stony Brook University

2012

The IPCC-AR4 simulations project a robust poleward shift and slight strengthening of the mid-latitude jet and storm track in the Southern Hemisphere under global warming. In order to find out why the jet and storm track respond in this way, three important studies have been performed, as follows:

1) The quality of IPCC-AR4 climate simulations has been investigated by comparing model simulations with atmospheric reanalyses in terms of not only the mean flow but also storm track variations. Reanalyses data are separated into two time periods: before and after satellite, with the after-satellite NCEP reanalysis used as the reference. The primary patterns of mean flow and storm track variations and co-variability have been compared and model simulations are found to be consistent with before-satellite reanalyses, suggesting a reliable quality of IPCC AR4 climate simulations.

2) The jet north-south shift (or zonal index) mode, the leading mode of internal variability of the mid-latitude jets, has been found to exhibit a much longer auto-correlation timescale in idealized dry models compared to those in GCMs or in observations. One major difference between dry models and GCMs is lack of moist processes in dry models. Experiments are conducted by mimicking the missing diabatic heating due to moist processes in a dry model in two simple ways. Results suggest that moist heating provides a negative feedback to jet shift variations, reducing the timescale substantially, making it more comparable to that observed.

3) Different diabatic forcings representing the impact of global warming that are derived from projected temperature change between the end of 20th and 21st centuries found in IPCC-AR4 simulations, including the static stability forcing, temperature gradient only forcing, and tropopause height rise forcing, are imposed in our idealized model to test which mechanism may be responsible for causing the projected poleward shift of the jet and storm track. Experiments have been conducted using both a dry model and models with simple representation of moist processes. Results suggest that change in temperature gradient near the tropopause is most important, followed by tropopause height rise, whereas static stability change is not important.

Table of Contents

CHAPTER 4 DIABATIC DAMPING OF ZONAL INDEX VARIATIONS 73

CHAPTER 5 UNDERSTANDING GCM PREDICTED STORM TRACK CHANGES UNDER GLOBAL WARMING 106

List of Figures

List of Tables

.

.

.

.

Acknowledgements

I would like to take this chance to express my deep gratitude to a number of people who have helped and contributed to this work.

First and foremost, I would like to thank my advisor, Dr. Edmund Chang. I would never have been able to finish my dissertation without his excellent guidance, caring, patience, and providing me with an excellent atmosphere for doing research. The great training I've received from him has benefited and will continue benefitting me in the future career.

I would also like to thank my committee members, Dr. Sultan Hameed, Dr. Kyle Swanson, Dr. Dong-Ping Wang and Dr. Minghua Zhang, who gave me valuable advice that makes this dissertation a better work. Thanks also go to a lot of my colleagues and friends, especially Dr. Yanjuan Guo, and Minghua Zheng for their collaboration in part of this work and their help with my life and work. Also I like to thank Carol for her kind and patient help with my life and academic procedures throughout my whole Ph.D. pursuing.

Finally, I would like to thank my husband, my parents and my daughter for their love and support during my pursuit of the Ph.D. degree.

Chapter 1 Introduction

1.1 What are jet variability and shift under global warming?

In the past two decades or so, the question of whether human being is changing the global climate in a significant way through the greenhouse effect has increasingly drawn the attention of the world. The earth's surface is about 33 K warmer on average than it would be if there were none of the greenhouse gases in the atmosphere. Most scientists believe that the earth is undergoing some warming as a result of the increase in anthropogenerated emissions that absorb infrared radiation, or enhance the greenhouse effect, although there is still some debate over this issue. In this study, we will take global warming as a starting point and investigate the temperature and jet responses to increased greenhouse gas concentrations.

The jets we are interested in are located in the mid-latitudes and are usually referred to as the eddy-driven jets, and they are associated with the storm tracks. In this study, the mid-latitude storm tracks are defined as the geographic maxima in transient eddy statistics (Blackmon 1976), and this definition is widely used in the climate dynamics community. The statistical quantities that are usually used to represent the storm tracks include the meridional wind variance or momentum flux at 300 hPa, heat fluxes at 700 hPa and so on (see Chang et al, 2002). The synoptic-scale baroclinic waves in the storm tracks are associated with heavy precipitation, strong winds, and rapid temperature changes in the mid-latitudes, and are responsible for much of the weather, especially during the cool seasons. They also play an important role in climate by transporting large amount of heat, momentum, and moisture that act to drive and maintain the general circulation. Numerous studies (e.g., Karoly 1990; Branstator 1992, 1995; Robison 1991, 1994, 1996, 2006; Yu and Hartmann 1993; Hartmann 1995; Kidson and Sinclair 1995; Feldstein 1998; Feldstein and Lee 1998; Hartmann and Lo 1998; Kushner et al. 2001; Lorenz and Hartmann 2001; Gerber and Vallis 2007 and so on) have shown that changes and variations in the mid-latitude storm tracks are closely tied with those in the mid-latitude jets. Therefore, the jet variability and change under global warming are of great interests.

Many previous studies suggested that the dominant mode of interannual and day-to-day variability of the zonal wind in the Southern Hemisphere is an approximately equivalent barotropic dipole with maximum anomalies at 40^{o}S and 60^{o}S, representing the north-south fluctuations in the position of the zonal-mean mid-latitude jet about its time mean position at 50^{o}S (Kidson 1985, 1986, 1988; Nigam 1990; Karoly 1990; Hartmann and Lo 1998; Feldstein 2000a; Lorenz and Hartmann 2001). This leading mode of the midlatitude zonal flow variability observed in the Southern Hemisphere is also readily simulated in numerical models (Robinson 1991, 1996; Yu and Hartmann 1993; Lee and Feldstein 1996; Feldstein and Lee 1996, 1998; Limpasuvan and Hartmann 1999). This north-south shifting of the mid-latitude jet is referred to as the zonal index variations in this study. We will also call it the jet shift mode.

Under global warming, Yin (2005) found a poleward shift of the mid-latitude storm tracks and jet in multiple model outputs of IPCC AR4 (The fourth Assessment Report of the Intergovernmental Panel on Climate Change) experiments. In addition, a poleward shift in the eddy-driven jets has been found in a GCM experiment by Kushner et al. (2001), and several studies (Fyfe 2003; Chen and Held 2007) have suggested that the Southern Hemisphere jet has shifted poleward over the second half of the 20th Century. Lu et al (2008) also found a poleward extension of the poleward edge of the Hadley cell responding to the global warming in the greenhouse gases emission scenarios of IPCC AR4 experiments. These and other studies suggest that poleward shifting of the mid-latitude jet and the associated storm track is a robust projection under global warming.

While plenty of studies have either focused on the jet variability found in observations, reanalyses and various model experiments, or how the mean position of the jet will respond to anthropogenic greenhouse gas emissions, little emphasis has been placed on what connection there might be between the jet variability and jet changes until recently. Barnes and Hartmann (2011), based on the results of a barotropic model, have suggested that jets closer to the equator exhibit large meridional variability while jets closer to the pole do not, and Barnes and Polvani (2012) have confirmed that such a relationship between mean jet latitude and jet variability is also present in more complex CMIP5 coupled model simulations for the SH and the North Atlantic. In addition, several studies (Kidson and Gerber 2010; Barnes and Hartmann 2010b, 2010c) have suggested that the jet variability timescale is very sensitive to the latitude location of the jet in CMIP3, and Kidson and Gerber (2010) further found that under global warming, the jet tends to shift more poleward in response to global warming in models that have a longer jet variability timescale. On top of that, previous studies have suggested that jet variability in idealized dry mechanistic models – which are often used to understand how the mid latitude jets respond to changes in diabatic heating under global warming – generally have jet variability timescales that are significantly biased long (Yu and Hartmann 1993; Polvani and Kushner 2002; Kushner and Polvani 2004; Gerber and Vallis 2007; Gerber et al. 2008). In this study, we will explore why there are such biases in these dry mechanistic models, as well as whether these long jet variability timescales found in these models have any implications on the jet responses simulated by these models.

1.2 What do we mean by diabatic forcings?

Why do the mid-latitude jets move poleward when the climate becomes warmer due to increasing greenhouse gases? What are responsible for this shift? So far no consensus has been reached, although a few interesting hypotheses have been raised. Here, we will mention a few, but more detailed discussions of these hypotheses will be presented later. One hypothesis is that the shift of the mid-latitude eddy-driven jets and storm tracks corresponds to increased static stability over subtropics due to more warming in the upper troposphere than near the surface under global warming. The second one suggests that the jets or storm tracks shift primarily as the response to the rise of tropopause height when the troposphere becomes warmer and the stratosphere gets cooler. A third hypothesis suggests that the shift is due to increase in the meridional temperature gradient near the tropopause due to warming in the tropical upper troposphere and cooling in the lower stratosphere under global warming. No matter whether it is the static stability change, the rise of tropopause height or the increase in temperature gradient near the tropopause, all three mechanisms are forced by changes in diabatic heating under global warming due to increasing greenhouse gases in the atmosphere. This is the first kind of diabatic forcing we will investigate in this study. This kind of diabatic forcing will be used to force numerical model experiments for investigating the mechanisms that may be important in driving the poleward shift of the jets and storm tracks.

An idealized dry global circulation model will be used to examine the impact of the diabatic heating related to global warming. However, previous studies (Yu and Hartmann 1993; Kushner and Polvani 2004; Gerber et al., 2008) have suggested that the zonal index mode has very long auto-correlation time scale in some dry model experiments, and results of this study confirm this. Our hypothesis is that in the dry model, the lack of moist processes provides no diabatic feedback in the simulations. In various previous studies (Shiotani 1990; Karoly 1990; Hartmann 1995; Kidson and Sinclair 1995; Feldstein and Lee 1998; Hartmann and Lo 1998; Yang and Chang 2007), a positive dynamical feedback via eddy momentum fluxes has been confirmed to be able to increase the persistence and low-frequency variance of the zonal index. In this study, we will explore the possible impacts of diabatic heating related to moisture transport by storm track eddies on the persistence of the zonal index. To achieve this, we will introduce several ways in which extra diabatic heating can be imposed in a dry model. This is the second kind of diabatic forcing that we will consider.

1.3 Goals of this dissertation

To explore the reasons responsible for the projected poleward shift of the mid-latitude jets and storm tracks under global warming, we will first resolve several related problems. In this dissertation, we will try to seek answers to the following questions:

i. Can we trust the mid-latitude jet variability and shift in the prediction of IPCC AR4 multi-model simulations? How well do the models simulate the mean state and its variability, and are the transient eddies and their variability captured well? How about the relationship between the eddies and the mean flow?

ii. Why do dry model simulations frequently have an abnormally long zonal index autocorrelation timescale compared with that found in GCM simulations? What are the implications of such a deficiency? How can this deficiency be improved?

iii. Based on the ensemble mean temperature change found in the IPCC AR4 model global warming prediction, several hypotheses have been suggested to explain the projected jet and storm track shift. What are the most important reasons for the poleward shift of the jets in our modeling study? Does the model response depend on the autocorrelation time scale of the zonal index mode? What are the implications of such a dependence?

Answers to these questions should provide important new insights on the reasons behind the poleward shift of the mid-latitude jet, such that the detailed mechanism behind such a poleward shift under global warming can be further investigated in future studies.

1.4 Organization of this dissertation

In this chapter, the main goals of this dissertation have been briefly introduced.

In chapter 2, the datasets used in this dissertation, including the reanalyses, satellite observations, and GCM simulations, are described. In addition, the idealized dry model we employ in this study will be introduced.

In chapter 3, we will investigate the quality of the IPCC AR4 multi-model simulations in terms of the mean-state climate and transient eddy variability, to establish the level of confidence that can be placed on the prediction of mid-latitude jets variations and change under global warming.

The influence of diabatic heating due to moist processes on the autocorrelation timescale of the jet shift mode will be examined in chapter 4, by using an idealized dry model with extra diabatic heating added to mimic some of the impacts of the missing moist processes. The timescale of the zonal index mode in the presence of the extra diabatic feedback will be compared to the long timescale found in dry model runs.

Several hypotheses on what may be responsible for the poleward shift of mid-latitude jets under greenhouse gases emission scenarios raised by previous studies are first briefly described in chapter 5. Then numerical experiments driven by different global warming forcing will be conducted to explore which one of these is essential in forcing the projected jet shift. Results of experiments conducted with or without the extra diabatic feedback will be compared and the implications will be discussed.

Summary of the main results, as well as the conclusions and some possible future studies are presented in Chapter 6.

In this study, the terms “transient eddies”, “baroclinic waves”, and “storms” are used interchangeably. This is reasonable because the statistics of 2-10 days transient eddies that we will examine are dominated by baroclinic waves, which are closely associated with mid-latitude storms.

Chapter 2 Brief descriptions of the datasets and an idealized storm track model

The datasets used in our work presented in this dissertation include the reanalyses, satellite observations, and GCM simulations. Most of the modeling work done in this dissertation makes use of an idealized dry storm track model. Prior to showing the main results in later chapters, brief descriptions of these datasets and this idealized model will be presented in this chapter.

2.1 The reanalyses

In this study, two reanalysis datasets have been employed. One is the product from the European Center for Medium-Range Weather Forecasts (ECMWF), called the ECMWF reanalysis. The other one is from the National Centers for Environmental Prediction (NCEP) and National Center for Atmospheric Research (NCAR), we call it the NCEP/NCAR reanalysis (Kalnay et al. 1996; Kistler et al. 2001). These reanalysis datasets are global gridded covering all atmospheric fields, re-analyzing all the available observations world-wide by using a consistent and comprehensive data assimilation system. Therefore they are often regarded as the most reliable atmospheric datasets and treated as being close to observations (Kalnay et al. 1996; Stendel and Arpe 1997; Engelen et at. 1998; Trenberth and Guillemot 1998; Annamalai et al. 1999; Jakob 1999; Nigam et al. 2000; Newman et al. 2000; Kistler et al. 2001; Trenberth et al. 2001 and so on).

The forecast model for the NCEP/NCAR reanalysis is the NCEP global spectral model operational in 1995, with 28 “sigma” vertical levels and a triangular truncation of 62 waves (T62), equivalent to about 210-km horizontal resolution. The data is available from 1948 to 2007 when we started this study. And for ECMWF, there are several reanalysis products in which we only use the ECMWF 40-year reanalysis (ERA-40; Uppala et al. 2005) in this work. The forecast model used for ERA-40 is the ECMWF operational spectral model in 1999 with 60 hybrid vertical levels and a triangular truncation of 159 waves (T159), which has higher resolution than the model used for producing the NCEP/NCAR reanalysis (T62). This dataset is originally intended as a 40-year reanalysis beginning in 1957 (the International Geophysical Year), but it was later extended to cover 45 years to 2002. In this study, both NCEP and ERA40 reanalysis data used are 6-hourly and are both interpolated to the same horizontal resolution of 2.5^o by 2.5^o, and the same vertical resolution of 17 levels from 1000hPa to 10hPa. The zonal and meridional wind at 300 hPa and 700 hPa, the temperature at 700hpa, and the precipitation are the main variables we have used in this study.

After 1979, large amounts of satellite data became regularly available and these are assimilated into the reanalysis data. Because of this, climate variations could be captured better and the datasets in this time period are expected to have been improved compared with data before 1979 in terms of smaller biases, especially in regions with few in situ observations. Therefore, the reanalysis datasets after satellite are used in this study as the climatological benchmark. The data before satellite can be used for comparison to examine the uncertainty in the reanalysis.

2.2 The Global Precipitation Climatology Project (GPCP) precipitation dataset

The Global Precipitation Climatology Project (GPCP; Huffman et al. 1997) was established by the World Climate Research Program to quantify the distribution of precipitation around the globe over many years. One of the primary products of this project is the GPCP Version 2.1 Combined Precipitation Data Set (Adler et al. 2003), which is a gridded analysis optimally merging gauge measurements at over 6,000 rain gauge stations and satellite estimates of precipitation computed from microwave, infrared, and sounder data observed by the international constellation of precipitation-related satellites. This dataset provides monthly rainfall estimates on a 2.5×2.5-degree global grid from 1979 to the present. The careful combination of satellite-based rainfall estimates provides the most comprehensive analysis of rainfall available to date over the global oceans.

Another product we use in this study is the daily version of GPCP v1.1 1DD data from 1996 December to 2009 February (Huffman et al. 2001). It has 1.0×1.0 degree spatial resolution which is higher than resolution of the GPCP monthly precipitation of 2.5×2.5 degree, and is scaled to the V2.1 monthly resolution. Previous studies have established that the daily version of GPCP v1.1 data presents reasonable estimates of precipitation around mid-latitude cyclones (e.g. Chang and Song, 2006). Guo and Chang (2010) also suggested that the GPCP precipitation estimates are useful for examining the storm track variability. The GPCP data have also been found capable of revealing precipitation changes on seasonal to interannual time scales (Adler et al. 2003). It also offers the potential for studying changes of precipitation at longer time scales.

2.3 IPCC AR4 CMIP simulations

"In response to a proposed activity of the World Climate Research Programme (WCRP) Working Group on Coupled Modeling (WGCM), PCMDI (Program for Climate Model Diagnosis and Intercomparison) volunteered to collect model output contributed by leading modeling centers around the world. Climate model output from simulations of the past, present and future climate was collected by PCMDI mostly during the years 2005 and 2006, and this archived data constitutes phase 3 of the Coupled Model Intercomparison Project (CMIP3). In part, the WGCM organized this activity to enable those outside the major modeling centers to perform research of relevance to climate scientists preparing the Fourth Assessment Report (AR4) of the Intergovernmental Panel on Climate Change (IPCC)." (quoted from http://www-pcmdi.llnl.gov/ipcc/about_ipcc.php)

2.3.1 The 20th Century (20c3m) simulations

The climatology of CMIP3 simulations (total 28 runs from18 different models) we used in this work are the 20th century runs which was called 20c3m, shown in Table 2.1. Only the simulations with daily products available are used because we need to calculate the variance/covariance statistics. In this study, the daily 20c3m simulation data used cover the period from 1961 to 2000, and the variables used include the temperature and wind at 300 hPa and 700 hPa. The monthly total precipitation is also examined in this time period.

2.3.2 The global warming scenarios (A1B, A2)

Since we are interested in the variations under global warming in the future, we treated the temperature anomalies between 2081-2100 and 1981-2000 derived from CMIP3 simulations as the global warming temperature anomalies to be applied as forcing in our modeling studies (see below).

In order to increase the sample size for the analysis, two greenhouse gas (GHG) emission scenarios have been examined in this study. These include the A2 scenario, a high-emission scenario (CO_2 concentration reaches 840 ppm at the end of the 21st century) in IPCC AR4 models, as well as a less aggressive GHG forcing scenario (A1B with CO_2 stabilized at 720 ppm) (Nakicenvoic et al. 2000). For the purpose of diagnosing the storm track variability in these simulations, daily data is needed, but monthly mean data are also used to examine mean flow variability and changes.

2.4 An idealized dry storm track model

Numerical experiments have been carried out to understand what drives the changes in the mid-latitude jet under global warming. The idealized dry storm-track model used here is developed based on the dynamical core of the Geophysical Fluid Dynamics Laboratory (GFDL) global spectral model (Held and Suarez 1994). It has a horizontal resolution of T42 (approximately $2.8^o \times 2.8^o$ Gaussian grid spacing), and uses 20 evenly spaced sigma levels in the vertical. Realistic orography, smoothed to model resolution, is imposed. A land-sea mask is used, with stronger surface friction over land. The only forcing imposed to drive the model is Newtonian damping to a radiative equilibrium temperature profile. With this parameterization, the First Law of Thermodynamics can be written as:

$$\frac{D\theta}{Dt} = -\frac{\theta - \theta_E}{\tau} - \kappa\nabla^8\theta, \qquad (2.1)$$

where τ is the radiative time scale. θ_E can be split into two parts, as follows:

$$\theta_E = \theta_C + \tau Q, \qquad (2.2)$$

where θ_C is the target climate, and Q can be interpreted as the diabatic heating distribution. The novelty of this study is the ability to come up with a Q (which is fixed for each model run) such that a model climate (in terms of the mean temperature distribution) that is close to θ_C can be obtained. When a model climate that is close to θ_C has been obtained, Q is the only diabatic forcing in the model in the time mean and can be regarded as the climatological-mean net diabatic heating rate. In order to achieve the amplitude of eddies to be close to that found in the real atmosphere, the target climate is imposed with the observed temperature profile but with reduced static stability, as follows:

$$\theta_C = \theta_{obs}(x, y, p) - Az(p), \qquad (2.3)$$

where $z(p)$ is the average geopotential height of the pressure surfaces. More details concerning the model formulation can be found in Chang (2006). It should be noted that mean flow and eddy statistics that have been simulated in this storm track model can be tuned to be quite similar to those observed in the atmosphere (Chang 2006, Chang and

Zurita-Gotor 2007) by iteratively tuning the heating forcing Q , as follows. Starting with a first guess Q_o, a new heating can be obtained by the following iteration:

$$Q_N = Q_{N-1} - \frac{2}{3}\frac{\overline{\theta}_{N-1} - \theta_C}{\tau}, N = 1, 2, 3, ..., \qquad (2.4)$$

This procedure is continued until the difference between the model climate and target temperature profile becomes small. Since the model is nonlinear, there is also the possibility that one can obtain a model climate close to the target climate but have very different eddy fluxes and heating that maintain those similar temperature distributions, but Chang (2006) found that in practice quite similar final eddy fluxes are obtained even if one starts with quite different Q_o. In the appendix of Chang (2006), he found that the final Q distributions can be quite different, especially within the deep Tropics, but much of the differences in the Q forcings are balanced by differences in the mean Hadley and Walker circulations and do not appear to significantly affect the synoptic eddy distributions in the extratropics. The hypothesis that storm track structure depends only on the mean flow, and is not sensitive to the details in the forcings, seems reasonable. Meanwhile, Chang (2006), as well as Chang and Zurita-Gotor (2007) iterate the Q to simulate climate anomalies associated with ENSO and seasonal variations of the winter Pacific jet/storm track, respectively, and they find that the model not only succeeds in simulating the climatology of storm tracks, but also produces quite realistic simulations of storm track anomalies when the model climate is forced to resemble observed climate anomalies. Therefore this storm track model is an ideal platform to study eddy-mean flow interactions in midlatitude atmospheric low frequency variability.

The experiment forced with (2.3) using the observed temperature distribution (but with reduced static stability) as the target climate will be referred to as the control run hereafter. Note that this approach is quite different from other idealized model studies (e.g. Haigh et al. 2005; William 2006; Lorenz and DeWeaver 2007) since all of these previous studies used somewhat arbitrary idealized forcing and the model climate in these studies do not necessarily resemble observed climate. After we construct the control run, the target temperature profile of global warming experiments has been obtained by adding the global warming forcings, which are based on the ensemble mean change found in IPCC AR4 greenhouse gas emission prediction, onto the temperature profile of the control run. The quality of the IPCC AR4 models' output will be discussed in Chapter 3. While in Chapter 5, we will introduce the climate change experiments in more details.

Apart from the dry model simulations mentioned in the last paragraph, modified versions of the model with extra diabatic heating terms added to mimic some of the effects of moist processes have also been performed in order to examine the impact of diabatic feedback on jet variability. More details on these experiments will be provided in Chapter 4.

Model	Resolution	Runs
BCC_CM1	2.5×2.5	4
CCCMA_CGCM3_1_t63	T63L31	1
CCCMA_CGCM3_1_t47	T47L31	5
CNRM_CM3	T63L45	1
CSIRO_MK3.0	T63L18	2
CSIRO_MK3.5	T63L18	1
GFDL_CM2.0	2.5×2 L24	1
GFDL_CM2.1	2.5×2 L24	1
GISS_AOM	4×3	1
GISS_MODEL_E_H	5×4 L20	1
GISS_MODEL_E_R	5×4 L20	1
IAP_FGOALS1_0_G	128×60	1
INMCM3.0	5×4 L21	1
IPSL_CM4	2.5×3.75 L19	2
MIROC3_2_HIRES	T106L56	1
MIUB_ECHO_G	T30L19	1
MPI_ECHAM5	T63L31	2
MRI_CGCM2.3.2A	T42L30	1

Table 2.1: The IPCC AR4 models having daily data used in this study.

Chapter 3 Assessing climate model simulations of storm track variability

3.1 Introduction

In the last few decades, it has become popular to define midlatitude storm tracks based on synoptic timescale eddy variance/covariance statistics, rather than the simple geographic organization of cyclones, as an alternative way to study storm tracks which directly impact the weather and climate in mid-latitudes (see Blackmon 1976; Blackmon et al. 1977; Hartmann 1974; Randel and Stanford 1985). In this way, a three-dimensional profile of storm tracks has been documented, and the seasonal, interannual and decadal variability of storm tracks have been investigated, in terms of eddy activity. Trenberth (1981a, 1981b, 1982) quantitatively defined the main storm tracks in the SH by using 2-8 day bandpass geopotential height and meridional wind variance since these high-frequency baroclinic transient variance are the crucial contributors. Apart from geopotential height and meridional velocity variance, the transient eddy fluxes of heat and momentum are also good indicators of storm tracks because of their strong implications of baroclinic instabilities as the ultimate mechanism generating the transients (Hoskins et al. 1983). These high-frequency bandpass filtered variables linked to the baroclinic disturbances maximize at the position of storm tracks, thus the shift of these variance maximum indicates the shift of storm tracks.

With increasing greenhouse gases, it is generally accepted that global temperature will increase in the foreseeable future. However, how that impacts regional climate is still not entirely clear. Regional climate impacts, especially during the cool season in the mid-latitudes, depend critically on how the storm tracks change. Several recent studies have suggested that the mid-latitude storm tracks are predicted to shift poleward based on analyses of the IPCC AR4 experiments. Yin (2005) found a poleward shift of mid-latitude storm tracks, and Lu et al (2008) discovered a poleward extension of the polar edge of the Hadley cell responding to the global warming in the green house emission scenarios of multiple model outputs of IPCC AR4 experiments. Son et al (2008) also found a significant poleward shift of eddy-driven jets in IPCC AR4 coupled models which do not take into account the ozone recovery. How much can we trust these model simulations in terms of the poleward shift of storm tracks? Before we go further into the exploration of the real mechanisms behind such a response under global warming, it is important to assess the performance of IPCC AR4 models.

Therefore in this study the quality of IPCC AR4 20th century climate experiments has been investigated. If they are good at simulating the appropriate mean flow and storm track variations, we could have more confidence in the prediction of the climate models. Most previous attempts to assess the quality of climate model simulations focus on validating the simulation of the mean flow. For example, Reichler and Kim (2008) found significant improvement of the latest CMIP-3 models compared to their predecessors in terms of the time-mean state of climate. Whereas in our study, we are concerned not only with the mean flow, but also the transient eddy variability instead of just the storm track climatology, as well as the relationship between the mean flow and the eddies. Lau (1988) and Metz (1989) established that storm track variances and covariances are closely related to mean flow change, and further studies argued that the interaction between storm tracks and the low-frequency flow should be regarded as two symbiotic pieces: the response of storm track transients to changes in the planetary-scale flow, and consequent transient feedback onto that planetary-scale flow itself (reviewed by Chang et al. 2002). Therefore, investigating the relationship between storm tracks and the mean flow in model outputs could be an effective way to verify the credibility of IPCC AR4 experiments regarding storm track variability. Since both the eddy momentum and heat fluxes are indicators of the exchange of potential and kinetic energy between storm tracks and the mean flow, these two quantities will be investigated in this study.

In this paper, the reanalysis data and outputs of IPCC AR4 20th century climate experiments will be investigated in several statistical ways, in order to assess the model performance in terms of storm track variability. Section 3.2 will introduce the datasets used in this paper and some analysis tools applied here. The detail analysis of the characteristics of individual fields will be discussed in section 3.3 for both the reanalysis and IPCC AR4 model outputs. In section 3.4, we will explore the relationship between mean flow and storm track variability in the datasets. Summaries and discussion will be presented section 3.5.

3.2 Methodology and data

3.2.1 Empirical Orthogonal Function (EOF) and Singular Value Decomposition (SVD) analyses

The analysis tool which one applies in the research plays an important role in data analysis. Empirical orthogonal function (EOF) decomposes a field into eigenvectors and corresponding time series. Frequently the leading modes account for the majority of the variance of the original field, and occasionally these modes can have physical significance. It is useful for the exploration of single field. In section 3.3, EOF analysis will be applied to assess reanalysis and IPCC AR4 models daily data in terms of individual fields. However for the relationship between two fields, Bretherton et al. (1992) assessed several methods including combined principle component analysis (CPCA), canonical correlation analysis (CCA), and singular value decomposition (SVD), comparing their coupled patterns and time series in climate data. Each method has its own characteristics, shortcomings and advantages, depending on the purpose of the study.

In recent twenty years, a number of studies have investigated the characteristics of the mean flow and storm track variability, and the relationship between these two. Lau (1988) used PCA to show that the leading patterns of storm track variability are strongly linked to low-frequency variability in monthly averaged flow. Metz (1989) investigated the relationship between the mean flow change and eddy flux convergence by using canonical correlation analysis (CCA) and found several robust modes. Wallace et al. (1992) applied PCA, CCA, SVD and CPCA to investigate the relationship between the seasonal mean, wintertime sea surface temperature (SST) and 500-hPa height fields over the North Pacific, as well as compared the performance of each method. Chang and Fu (2003) inferred storm track variations from mean flow anomalies using CCA to explore the link between storm tracks and mean flow and found that the CCA results are consistent with reanalysis data over most storm track regions except northeastern North America where CCA predictions are generally poor.

One of the purposes of this study is to assess the performance of IPCC AR4 multi-model outputs in terms of storm track variability and the mean flow. We use SVD rather than CCA analysis in this study since the leading SVD modes explain more of the squared covariance between the two fields than any of the CCA pairs (Wallace et al. 1992; Bretherton et al. 1992) and are generally less noisy. As in many climate applications of these techniques, we will be dealing with fields in which the number of degrees of freedom is far less than the number of grid points because of a rather small number in the time domain (86 or 120 time slices vs. 64×16 spatial grid points).

One note here is that in order to make the mathematical results more physically meaningful, all the fields have been processed with the geophysical weight [latitude weighting by cosine(latitude) to account for changes in the area of each grid box with latitude] before they are used as input for the EOF and SVD calculations.

3.2.2 Dataset examined

The primary "observation" data for this study consists of 6-hour daily grid point reanalysis data produced by NCEP/NCAR and ECMWF. The variables selected include zonal wind u and meridional wind v at 300 hPa, v and temperature T at 700 hPa, for both NCEP/NCAR and ERA40 reanalysis. The data sets are separated into two periods by the year 1979, before that the coverage started from January 1958 to December 1978, called before-satellite; the second period extended from January 1979 to February 2002 for ERA40, and to February 2007 for NCEP reanalysis data, called after-satellite. The winter season is taken to be 3-month period from December, January to February (DJF), thus, there are 63 individual months in the dataset for the period of before-satellite, 71 months for ERA40 after-satellite, and 86 months for NCEP after-satellite. In this study, the NCEP reanalysis after-satellite is treated as the reference.

The Intergovernmental Panel on Climate Change (IPCC) Fourth Assessment Report (AR4) provides 28 20th century climate experiment (20c3m) runs of 18 coupled models which all contain daily zonal wind velocity and meridional wind velocity at 300 hPa as well as daily meridional velocity and temperature at 700 hPa. Some details of these 18 coupled models have been listed in Table 2.1. The time period of these model outputs used here is from 1961 to 2000, the same winter season (DJF), thus totally, there are 120 individual months. Another dataset used in this study is a 100-yr GFDL GCM run, which is forced by prescribed climatological solar forcing, sea surface temperature, and sea ice, with the full seasonal cycle, but without any interannual variations (Chang 2001). This run was made using an older version of the GFDL climate model (see Ting and Lau 1993) run at R30 horizontal resolution and is used as a reference to compare with the more recent CMIP3 model experiments. This run is called the GFDL-R30 run.

Daily average of reanalysis data is used to compare with CMIP3 model outputs, since CMIP3 only provides daily averaged field. However, the GFDL-R30 run provides instantaneous output daily at 00z consisting of 297 DJF months. Monthly mean streamfunction at 300 hPa is considered as the mean flow in this paper since there are very few models providing daily geopotential height data. It is derived from the u and v winds at 300 hPa using Spherepack 2.0 provided by UCAR. With respect to the storm track variability, it is indicated by monthly mean high-pass-filtered variance/covariance statistics, filtered by a 24-hour difference filter (Wallace et al. 1988). In their study, this 24-hour difference filter was suggested to be capable of isolating the high-frequency fluctuations similar to the periods ranging from 1.2-6.0 days in the geopotential height field. Moreover Chang and Fu (2002) showed that interannual variations of storm track statistics based on this filter behave very similarly to those computed using broader bandpass filters. The main storm track variability will be identified by filtered meridional velocity variance (v'^2) at 300 hPa, poleward momentum flux (u'v') at 300 hPa and poleward heat flux (v'T') at 700 hPa. As an example, the eddy heat flux at 700 hPa is computed as follows:

$$v'T'_{700-1df} = \overline{[v(t+24h) - v(t)][T(t+24h) - T(t)]} \qquad (3.1)$$

where v and T are the meridional velocity and temperature at 700 hPa, respectively, and the overbar denotes averaging over a month. Hereafter we will use sf300 to represent the mean flow, and use uv300, vsq300 and vt700 to stand for eddies.

The climatological seasonal cycle is first removed from both mean flow and storm track fields. Only Northern Hemisphere data are analyzed, and all fields are truncated to T32 resolution (64×16) prior to the EOF and SVD analyses to reduce noise.

3.3 Individual fields analysis

Prior to exploring the relationship between low-frequency flow and storm tracks found in reanalysis and model outputs, it is necessary to first examine the performance of these two individual fields in both datasets by applying empirical orthogonal function

(EOF) analysis. Since the reanalysis data are expected to have much higher quality after the late 70's because of assimilation of the satellite data, so in this study, the NCEP reanalysis data covering 1979 to 2007 is considered as the reference.

3.3.1 Comparing reanalysis data from the two periods

Both NCEP and ERA40 have been separated into two time periods, the first started from 1958 to 1978, the same for both NCEP and ERA40 (referred to ncepb and era40b), the second one extended from 1979 to 2002 for ERA40 (era40a), and to 2007 for NCEP (the reference, referred to as ncepa). Empirical orthogonal function is applied to decompose the grid field of streamfunction (sf300), momentum flux (uv300) and meridional velocity variance (vsq300) at 300 hPa, and heat flux at 700 hPa (vt700) into various modes, respectively. To reiterate, all the results we will show are based on the Northern Hemisphere anomalies with the climatological seasonal mean removed.

Table 3.1 lists the variance and variance percentage of the first 3 EOF modes for the 4 variables introduced before for each of the reanalysis datasets, in the different time periods, respectively. The results shown in this Table indicate that, in the period of before-satellite, either the total variance or the variance distribution of EOF modes of ERA40 and NCEP reanalysis are quite close, for both mean flow and storm track variability. This is also the case in the period of after-satellite, however the variances mostly have larger magnitude in the after-satellite period. This is reasonable because in both reanalysis datasets, more variations are expected to be captured by assimilating the satellite data, even though these two reanalysis datasets are processed in different ways.

Therefore we expect that the reanalysis after-satellite has improved compared to data before-satellite, at least in terms of much larger variance.

For the mean flow, the variance and variance percentage between two time periods are also different for both NCEP and ERA40, even though the difference is not as large. From Table 3.1 we can also see that the percentage of variance explained by the leading EOFs are different between the two different time periods, even for mode 1 of sf300. Since we expect that the mean flow field in the Northern Hemisphere to be relatively well constrained by observations even in the before-satellite era, we believe that much of these differences are likely due to climate variability rather than the deficiency of the reanalysis in the before-satellite period. Note that in some cases, the first and second EOFs are not well separated (e.g. uv300 before-satellite), thus the leading modes could be mixed, making direct comparisons of the modes between the different periods difficult. We will come back to this point later. In the discussions below, we will mainly focus on the leading EOF.

The spatial patterns of the first leading EOF mode for streamfunction at 300 hPa of NCEP reanalysis after satellite is shown in Fig 3.1. Based on the geostrophic relationship, streamfunction is roughly equal to geopotential height divided by *f* (the Coriolis parameter). Wallace and Gutzler (1981) presented 5 teleconnection patterns in 500 hPa geopotential height during the Northern Hemisphere winter. In some regions such as over the Atlantic or the Pacific ocean which are the main paths of storm tracks, there are some similarities between their patterns and the leading EOFs. The monthly mean circulation corresponding to the 1st EOF mode is dominated by a nearly zonally symmetric pattern which bears little resemblance to any teleconnection patterns described in Wallace and Gutzler, except for a dipole like structure over the eastern Pacific. However, the other modes (not shown) do bear some resemblance to the PNA and NAO modes as documented by Wallace and Gutzler.

Before we examine the EOF characteristics of storm track variability, the climatological storm track distribution is shown in Fig. 3.2. All three variables, uv300, vsq300 and vt700 exhibit a rather zonally symmetric maximum at mid-latitudes around 30^o to 60^o in the Southern Hemisphere, indicating the storm track climatology. In the Northern Hemisphere, the monthly mean of eddy momentum flux at 300-hPa in boreal winter shows dipole patterns over both the Pacific and Atlantic ocean. Where the eddy momentum flux converges is the position of mid-latitude jet stream which is highly related with the storm track. Meanwhile the vsq300 and vt700 also maximize over the Pacific and Atlantic, demonstrating where the mid-latitude cyclones develop the storm track. Especially for the eddy heat flux, the peaks are located at the entrance of mid-latitude jet stream, then decrease gradually towards the exit.

Storm track variability including 300 hPa momentum flux and meridional velocity variance, as well as 700 hPa heat flux, have been decomposed by EOF analysis, and the EOF patterns are shown in Fig. 3.3. The first EOF mode of 300 hPa momentum flux explains 12% variance to the total. EOF1 for meridional velocity variance explains 17.6%, and for heat flux at 700 hPa it explains 15.7%. These three EOF spatial patterns all show some resemblance to their respective climatological distribution. The maxima are located over the north Pacific and the north Atlantic where the storm tracks are, meanwhile the variability over these regions show the same sign, consistent with the positive correlation between winter time storm track over the Pacific and the Atlantic (Chang 2004), suggesting the storm track in the entire hemisphere is strengthening or weakening at the same time. Another point maybe interesting here is that the link between the first pattern of 300 hPa momentum flux and 700 hPa heat flux. The correlation of the two PCs is about 0.57, which implies that they are significantly correlated. Therefore it is possible to say that the structure of the transient eddy fluxes of heat and momentum here (Fig. 3.3a, 3.3c), marked by the downstream (eastward) rapid growth in transient variance to the heat fluxes off the east coasts of Asia and North America, is consistent with the Fig. 3.3b of Chang et al. (2002) and Blackmon et al. (1977).

3.3.2 Mean flow and storm track variability in model simulations

In Table 3.1 it is apparent that in each time period the variance of both reanalyses are very close in terms of not only the mean flow but also the storm track variability, and the variance has been significantly increased after satellite data became available. How about CMIP3 model outputs compared with reanalysis data? The bar graphs comparing the total variability of model runs to the reanalysis for different variables in Fig. 3.4 give a brief picture of the performance of each experiment with respect to NCEP reanalysis after satellite, at least in terms of variability. The red column represents the performance of the GFDL R30 model (as mentioned above, this is a model from an earlier generation) which has a significantly lower variability compared with ncepa and other reanalysis data, as well as most of IPCC AR4 model outputs. The smaller and weaker variations of storm track variability and wave activity such as the momentum flux and heat flux were already noted in many previous studies, such as Boville (1991), Senior (1995), Sheng et al. (1998), and Chang (2001). Fig. 3.4 suggests that CMIP3 models show a substantial improvement in this respect compared with their predecessor. Because prior to CMIP3 there were no publicly available archives of daily (or higher frequency) GCM outputs, we were not able to compare our results with more models except for this GFDL-R30 run. This result shows that the improvement of coupled model not only could be seen in the time mean composite climate, but is also reflected in the transient eddy variability, at least in terms of the amplitude. The improvement of the variance might be partly due to more sophisticated model parameterizations and general increase in computational resources which allows for higher model resolution, consistent with the results of Boville (1991) and Kageyama et al. (1999). Note that 1 model that provided 4 ensemble members (BCC-CM1 model, the first 4 columns in Fig. 3.4) clearly has unrealistically weak storm tracks, and this model will not be considered in the discussions below.

To compare the variability found in reanalysis data and model simulations in more details, we need to compare the patterns. This can be done quantitatively using the Taylor diagram (Taylor 2001). The Taylor diagram can provide a concise statistical summary of how well patterns match each other in terms of their pattern correlation, their root-mean-square difference, and the ratio of their variances. In the Taylor diagram, the radial distance from the origin to the points are the standard deviation of the model regression normalized by the NCEP reanalysis after satellite, which indicates the model amplitude difference compared with the reference. The azimuthal positions give the correlation coefficient between two patterns (see the dashed lines in Fig. 3.5). So the point of 1 standard deviation and 100% correlation is the reference point. The distance between the points and the reference point gives the relative RMS difference between the two patterns. Therefore the Taylor diagram can inform us the relationship between the model EOF modes and ncepa EOF mode in terms of their correlation and their amplitude difference.

In this study, we have used a total of 28 individual runs from 18 IPCC AR4 models to examine the quality of these datasets compared to reanalysis data. The different colors and symbols representing the different runs are shown in Table 3.2. And as we mentioned before that for the storm track fields, the variance that each mode accounts for is not that different. So we will only show the regressions of mean flow and transient eddies related to the 1st EOF. In Fig. 3.5, the first EOF patterns between model output and reanalysis for 300-hPa streamfunction, 300-hPa momentum flux, 300-hPa meridional velocity variance and 700-hPa heat flux have been compared, respectively. For each field, there are several models bearing very poor correlation with ncepa for the 1st EOF mode which appears to be well separated from the other EOFs in ncepa. And for the uv300 field, even the reanalysis data before satellite has quite different 1st EOF pattern from that of ncepa, and for some models, the pattern correlation between their leading EOF and that of ncepa is nearly 0. It is not surprising that directly comparing the leading EOFs can be problematic since all the EOFs are constrained to be orthogonal and uncorrelated to each other, and they are not necessarily well separated and in the same sequence. Any mixing between different EOFs, or difference in the sequencing of EOFs, could result in large differences between the EOF patterns. Thus in this study, instead of comparing the EOFs directly, we examine whether each model exhibits similar variability as that found in ncepa using the methodology described below. In this methodology, the model output regressed on ncepa EOF patterns for each variable has been computed to compare to the EOFs of ncepa. Note that since we are regressing based on ncepa EOF patterns which are orthogonal, the model field could be decomposed based on that orthogonal characteristic and the total variance is still equal to the sum of the variance for each pattern due to the fact that the patterns are all orthogonal.

The mathematical procedure is as follows. To examine whether the variability found in the NCEP reanalysis data is also present in the model simulations, we use the EOF computed from the NCEP data after satellite as reference. We can write down the EOF analysis about the reference (D_{ref}) and model outputs (D_{out}) as follows:

$$D_{ref}(i,j,k) = \sum_{m=1}^{M} a_{ref}^{m}(k) P_{ref}^{m}(i,j)\,, \qquad (3.2)$$

$$D_{out}(i,j,k) = \sum_{m=1}^{M} a_{out}^{m}(k) P_{out}^{m}(i,j)\,, \qquad (3.3)$$

where i, j represent the spatial dimension, and k represents the time dimension. The subscript m denotes that there are M independent modes of patterns, here determined by the time dimension since in our application the number of time slices is smaller than the number of spatial grid points. Based on the characteristic that EOF patterns are orthogonal, the time series *a* can be derived by projecting the EOF patterns onto the original field:

$$D_{ref}(i,j,k) P_{ref}^{l}(i,j) = \sum_{m=1}^{M} a_{ref}^{m}(k) P_{ref}^{m}(i,j) P_{ref}^{l}(i,j) = a_{ref}^{m}(k) P_{ref}^{m\,2}(i,j)\Big|_{m=l}\,, \qquad (3.4)$$

In a similar manner, the model data can also be expanded in the EOF base computed from the NCEP reanalysis data. The time series for each mode in the model data can be obtained by projecting each NCEP reference EOF pattern onto the analogous model field:

$$S_{EOF}^{m}(k) = \frac{D_{out}(i, j, k) P_{ref}^{m}(i, j)}{P_{ref}^{m}(i, j) P_{ref}^{m}(i, j)}, \qquad (3.5)$$

In general, since the P_{ref}^{m} patterns are not the EOFs of the model data, the time series S_{EOF}^{m} for different m's are not independent of each other. The regression of the model field (D_{out}) based on this time series (S_{EOF}^{m}) is then computed, as follows:

$$R_{out}(i, j) = \frac{\sum_{k=1}^{T} S_{EOF}^{m}(k) D_{out}(i, j, k)}{\sqrt{\sum_{k=1}^{T} S_{EOF}^{m}{}^{2}(k)}}, \qquad （3.6）$$

This regressed pattern is then compared with the NCEP EOF pattern (P_{ref}^{m}) to examine whether model variability is close to variability found in the reanalysis data. Since the time series S_{EOF}^{m} are not independent with each other, the regressed patterns will in general not be the same as the original ncepa EOF pattern that the time series is derived from. If the pattern correlation between the regressed pattern and P_{ref}^{m} is high, and relative amplitude is close to 1, then model variability is close to observed variability for this particular mode. Note that in our application of EOF analysis, the time series (or PCs) are normalized to have unit variance, hence the spatial patterns carry the dimension of the field being analyzed together with the amplitude information.

In Fig. 3.6, the Taylor diagrams comparing the original ncepa 1st EOF and the regressed model patterns are shown for IPCC model run's 300-hPa streamfunction regression on NCEP reanalysis after-satellite EOF patterns of 300-hPa streamfunction. The relationship between the other reanalysis and ncepa is also plotted in Fig. 3.6. The green pentagram is for the ERA40 reanalysis after satellite (1979-2002), the other two pentagrams are for NCEP before satellite (black) and ERA40 before satellite (red). As we see, the green one which is the closest point to the reference point (1, 0) has the highest correlation and a close magnitude with NCEP reanalysis after satellite, which is what we expected. The two reanalysis from the other time period are also highly correlated with NCEP after satellite and have a little weaker amplitude. The remaining points show the results for the different IPCC models: the points distribute where the pattern correlation ranges from about 0.8 to above 0.9, meanwhile the amplitude is from 0.7 to 1.4 times of NCEP. More than half of these 28 IPCC models regression have larger magnitude than that of NCEP 1st EOF pattern itself, and all the data have high pattern correlation with the reference. Another point to note is that four points located far away from the main cluster are from the four runs of the BCC-CM1 model which do not perform well in terms of storm track discussed above. Just looking at the model results, it is hard to judge whether the model output is good or not. Therefore, a role of the reanalysis from different time periods used here is to represent the uncertainty of the pattern derived from NCEP reanalysis after satellite. In Fig. 3.6, the reanalysis before satellite are found to be always located among the model cluster which is contributed by the IPCC model outputs (although generally on the side closer to the reference point), which implies that those

IPCC model outputs can be considered acceptable because they share similar uncertainties with the reanalysis data without satellite.

Besides the low-frequency mean flow, we have also investigated how the transient eddies perform in the same experiments. Thus the three storm track fields, the 300-hPa momentum flux, 300-hPa meridional wind square and 700-hPa heat flux, have been investigated using the Taylor diagram in Fig. 3.7, Fig. 3.8 and Fig. 3.9, respectively. Results from the ERA40 after satellite reanalysis is always close to the reference point, but the other reanalysis data are generally still among the model cluster, implying these IPCC models are performing well in terms of storm track variability as well.

However, results from these three fields are not exactly the same. While the correlation range for 300-hPa wind square and 700-hPa heat flux are quite similar, the amplitude of the latter seems a little bit larger than that of the former (Fig. 3.8 and Fig. 3.9). For 700-hPa heat flux field, most models form a cluster except for two models, FGOALS1.0_g model and GISS_ModelE20/HYCOM, which have larger amplitude and lower correlation (Fig. 3.9). For heat flux, about half of the models have smaller amplitude compared with NCEP and half of them have larger magnitude. However for the meridional velocity variance, which is proportional to the eddy kinetic energy (Fig. 3.8), most models exhibit a smaller magnitude but similar correlation ranging from 0.8 to above 0.9 for the 1st mode. For the momentum flux, the average correlation is the lowest among these three fields while the magnitude seems smaller than that in heat flux field (Fig. 3.6). But note that the pattern correlation for the two before satellite reanalysis are also lower and the model results still cluster around those reanalysis results.

From the Taylor diagrams we have examined so far, it is clear that for the individual fields, regardless of whether we consider mean flow or storm track variability, results from the IPCC AR4 model outputs are mostly clustered around those based on the two reanalysis datasets before satellite, suggesting that the difference between the variability simulated by these models and ncepa might be similar to the uncertainty of the variability derived from reanalysis data from different time periods. Later in this chapter, we will show that the spread between the results computed based on different models are consistent with the spread between the results based on different ensemble runs from a single model, suggesting that much of that spread could have arisen from uncertainties related to climate variability.

The results shown in the Taylor diagrams can be summarized by calculating the Root-Mean-Square (rms) difference between each symbol and the reference point, and the results are shown in Table 3.4. The first two rows of black bold numbers are the rms difference between reanalyses before satellite (era40b and ncepb) and ncepa, they are much larger than that between ERA40 and NCEP reanalysis after satellite. The IPCC AR4 models exhibit relatively similar rms difference from ncepa compared with reanalyses before satellite. We also list a rank for the performance of each model relative to the ncepa for both mean flow and transient eddies shown in Table 3.4. The overall rank (last column) is the rank of the average of the 4 ranks. Run 2 of the MPI-ECHAM5 model behaves consistently well in terms of both mean flow and storm tracks and it is overall the best one among CMIP3 models. It also compares favorably with the reanalysis before satellite. However, run 1 of the same model does not perform as well and is only ranked #14 overall. For the others , they are good at some variables but not all of them, such as the MRI model which performs very well in mean flow but poorly in storm tracks. And among different runs of the CCCMA_t47 (which provided 5 runs), the rank can be very different, ranging from #3 to #18. Overall, given the spread in performance among different runs of the same model, one has to conclude that the differences between the models may not be significant.

3.4 Relationship between storm tracks and mean flow

In this section, SVD analysis is used to investigate the covariance relationship between mean flow and eddies. The singular value decomposition (SVD) is a fundamental matrix operation that can be performed to matrices that are not square or symmetric. From two data fields, the singular value decomposition of the cross-covariance matrix identifies pairs of spatial patterns which account for as much as possible of the mean-squared temporal covariance between the two fields. For patterns in each group, each one is spatially orthonormal to the rest. The singular values decomposed from the cross-covariance matrix are the covariances for each pair of patterns. Given that the patterns are orthonormal, the time series for each pattern can be reconstructed by projecting each of the original data field onto the pattern. SVD was used in several meteorological studies to document the relationship between two atmospheric or ocean fields (Prohaska 1976; Lanzante 1984; Dymnikov and Filin 1985; Wallace et al. 1992), and Bretherton et al. (1992) systematically compared several methods for finding coupled patterns in climate data.

Here, SVD analysis gives us two groups of spatial patterns and time series for the mean flow (subscript *mean*, i.e., 300-hPa streamfunction) and storm track variability (subscript *eddy*, i.e., 300-hPa momentum flux, meridional wind variance, and 700-hPa heat flux) for reference,

$$D_{ref\_mean}(i,j,k)=\sum_{m=1}^{M}b_{ref\_mean}^{m}(k)Q_{ref\_mean}^{m}(i,j)\,, \qquad (3.7)$$

$$D_{ref\_eddy}(i,j,k)=\sum_{m=1}^{M}b_{ref\_eddy}^{m}(k)Q_{ref\_eddy}^{m}(i,j)\,, \qquad (3.8)$$

where $Q_{ref\_mean}^{m}$ is orthogonal to other Q_{ref_mean}, and $Q_{ref\_eddy}^{m}$ is also orthogonal to other Q_{ref_eddy}. The "leading" patterns $Q_{ref\_mean}^{1}$ and $Q_{ref\_eddy}^{1}$ are chosen to account for the maximum covariance between the two fields. Successive pairs are chosen to account for the maximum covariance of the residual. The comparison between reanalysis and model outputs is done through computations of homogeneous and heterogeneous maps. For the reanalysis (ncepa) which is taken to be the reference, the homogeneous map is the regression of mean flow field on the time series in the same group for each mode, defined as the regression of $D_{ref\_mean}(i,j,k)$ on $b_{ref\_mean}^{m}(k)$. Whereas the heterogeneous map is the regression of storm track variability field (D_{ref_eddy}) based on the time series in the other group ($b_{ref\_mean}^{m}$) for each mode. As in the EOF analysis, there is again the possibility that the ordering of the modes may be different in the different datasets, so direct comparison between SVD patterns may be misleading. Hence for the IPCC AR4 model outputs, as well as for the other reanalysis datasets, we computed the time series

(S_{SVD}^{m}) by projecting the reference SVD pattern of 300-hPa streamfunction ($Q_{ref\_mean}^{m}$) computed based on ncepa onto the analogous model field (D_{out_mean}). The model regression of 300-hPa streamfunction field (D_{out_mean}) on this time series (S_{SVD}^{m}) is considered the homogeneous map of the models, and the model regression of storm track variability (D_{out_eddy}) on this time series (S_{SVD}^{m}) is the heterogeneous map of the models. Comparison of the homogeneous maps for the streamfunction demonstrate whether the models exhibit similar mean flow changes as those exhibited by the reanalysis, while comparisons of the heteorogeneous maps for the eddy fields show whether the models simulate similar eddy response to those found in the reanalysis in response to similar mean flow variability.

In Fig. 3.10, the 1st SVD pair of spatial patterns between the mean flow and storm track variability for ncepa are plotted, the patterns of the 300-hPa streamfunction are shown in (a), (c) and (e), while the associated patterns of 300-hPa momentum flux, 300 hPa meridional wind variance, and 700-hPa heat flux are shown in (b), (d) and (f). Each pair shares the largest covariance between two fields. For all the mean flow patterns, they share a lot of similarity with two positive maxima over the Pacific and Atlantic ocean at around 40^{o} - 50^{o}N where the mid-latitude jet locates. These patterns are very close to the EOF1 of the streamfunction field, with an average pattern correlation of 0.82. In (b), increase of the eddy momentum flux peaks at the same latitude of the streamfunction, and over the Pacific it also starts to decrease at the latitude where the jet is. With respect to vsq300 and vt700 (shown in (d) and (f)), they both exhibit a positive maximum at 50^{o}N and negative one equatorward over the Pacific. While over the Atlantic, the maximum center is extending a little poleward. The patterns of all three 1^{st} SVD pairs between mean flow and storm track fields indicate that the jet and storm track both shift poleward, perhaps with some enhancement given the larger positive centers than negative ones. Also the square covariance percentage for each pair is calculated in Table 3.3. For all three cases, the 1^{st} SVD pair accounts for around 50% of the squared-covariance and is clearly the dominant mode, and the first 4 modes account for about 80% of the total.

The Taylor diagram is again used here to compare the homogeneous and heteorogeneous maps computed based on IPCC models and reanalysis. But the difference here is that there are two patterns for each mode: there is a spatial pattern for the low-frequency flow (the homogeneous map), and a spatial pattern for the storm track (the heteorogenous map). Fig. 3.11 to Fig. 3.16 demonstrate the comparison between IPCC models output and reanalysis data for both mean flow and storm track fields.

The spatial patterns of the mean flow have been compared in Fig. 3.11, Fig. 3.13, and Fig. 3.15. In these figures, the regression map of the NCEP reanalysis is the homogeneous regression map of 300-hPa streamfunction based on SVD analysis of the covariance between the streamfunction and each of the eddy fields (i.e., 300-hPa momentum flux, 300-hPa meridional velocity variance and 700-hPa heat flux, in Fig. 3.11, Fig. 3.13 and Fig. 3.15 respectively) for NCEP reanalysis after satellite, which is the reference in these figures. While the interaction between the mean flow and storm track transients is in two ways: the response of the storm track transients to the mean flow changes, and the consequent transient feedback onto that mean flow itself. It is hard to separate these two distinct pieces since the interaction is nonlinear and complicated. In this study, we focus on the comparison between model performance and reanalysis in terms of the mean flow, storm tracks and their relationship, regardless of whether mean flow or eddies are the forcing or the response. Therefore the heterogeneous regression map of eddy variability based on mean flow time series has been compared with NCEP after-satellite reanalysis in Fig. 3.12, Fig. 3.14 and Fig. 3.16.

The relationship between IPCC model outputs and NCEP after-satellite reanalysis for mean flow spatial patterns produced by the SVD analysis of 300-hPa streamfunction and momentum flux has been shown in Fig. 3.11. For the first and third mode, most IPCC models perform quite similar on the mean flow related to the storm tracks for these two modes. For the second, there is a large spread in pattern correlation between model variability and NCEP reanalysis, suggesting that some models do not exhibit mean flow variability that is similar to that found in ncepa for that mode. In contrast, for the fourth mode, the models have patterns that show good correlation with that based on ncepa, but exhibit a broad range of amplitude. The ERA40 reanalysis after satellite is still the closest to the reference point, and the other two before satellite reanalyses are within the cluster of IPCC models implying the reasonable performance of these models.

In Fig. 3.12, the statistical characteristics of heterogeneous map of the 300-hPa momentum flux normalized by the reference are compared among all IPCC runs and reanalyses. Lower correlation and a broader range of amplitude are found for the IPCC AR4 model cluster of eddy momentum flux than those found for the mean flow (Fig. 3. 11). The after-satellite ERA40 reanalysis (green pentagram) has a very high correlation (higher than 0.9) with the reference and exhibits a larger magnitude than ncepa in all 4 leading modes. Whereas both the NCEP and ERA40 reanalysis before satellite (black and red stars) are of a smaller magnitude compared to the ncepa in the first 3 modes and lie within the cluster of model points, indicating the difference between the models and ncepa is consistent with the difference between the pre-satellite analysis and ncepa.

Fig. 3.13 shows the results for the mean flow for the SVD analysis between mean flow and 300-hPa meridional wind variance. It seems that the mean flow produced by IPCC models related to the meridional wind square is more similar to the NCEP reanalysis after satellite than that related to the momentum flux at the same level (Fig. 3.11), the cluster is more compact compared with Fig. 3.11, especially for the third and fourth mode. The ERA40 reanalysis after satellite is closer to the reference than it shown in Fig. 3.11, and the reanalyses before satellite are both at the edge of the cluster with higher correlation although they are still located within the cluster of GCM runs. The Taylor diagrams for the heterogeneous map of vsq300 are plotted in Fig. 3.14. The lower correlation and broader range of the magnitude compared to the mean flow regression are also exhibited here. Results are consistent with what shown in Fig. 3.12 except that the average correlation of the cluster generating by GCM runs in vsq300 map is a little bit higher than that in uv300 map. These results may indicate that the relationship of mean flow and v variance is captured better than that of mean flow and momentum flux since momentum flux is generally a noisier field.

With respect to the SVD analysis between the mean flow and 700-hPa heat flux (Fig. 3.15), the mean flow related to the heat flux provided by IPCC models performs very similar to the NCEP reanalysis for the first three modes in terms of close amplitude and high correlation. So far, as demonstrated in these three figures (Fig. 3.11, Fig. 3.13 and Fig. 3.15), the behaviors of mean flow of the first SVD pair in terms of comparison with ncepa for IPCC model runs and reanalysis datasets are very similar. Most models have larger magnitude than the reference in this mode, which implies the bigger variance of the mean flow in IPCC models than that of NCEP reanalysis. While in Fig. 3.15, for all the first 4 modes, it is evident that the mean flow field related to 700-hPa heat flux is better simulated by the IPCC AR4 models compared with the mean flow related to other storm track variables, especially the momentum flux. The heterogeneous map of heat flux related comparison is shown in Fig. 3.16, with the consistent results as the other storm track fields. However the amplitude of the heat flux seems to be captured well by IPCC models, in terms of the relatively small range of magnitude for first three modes compared to the momentum flux and v variance. The heat flux field for the 4th SVD mode seems to be poorly captured by the models, but the model results are still consistent with reanalysis before-satellite.

Overall, for 300-hPa momentum flux linked to the mean flow (Fig. 3.12), it seems that most models show smaller amplitude and lower correlation compared with ncepa for momentum flux variations than for the mean flow related to the momentum flux. For the other two storm track variables, 300-hPa meridional velocity variance and 700-hPa heat flux , it is apparent that they both show higher correlation than that displayed by the momentum flux, especially for the heat flux that have clusters showing good agreement in amplitude and high correlations, except for the fourth SVD mode.

Similar to the results for individual fields, the results for comparing the SVD patterns presented in the Taylor diagrams can be summarized by computing the rms difference between each symbol and the reference point (ncepa) in each Taylor diagram. Here, we will show the results for the 1^{st} SVD pair for each variable in Table 3.5. The first Table shows model performances in terms of the mean flow SVD homogeneous regressions, while the second one is in terms of the transient eddies SVD heterogeneous regressions related to the mean flow. Comparing to Table 3.4, the gap between reanalysis before and after satellite is not that large in the first Table, but with a larger difference in the second Table. All the models are also not very far away from the reanalysis before satellite. Similar to the single field comparison shown in Table 3.4, run 2 of the MPI ECHAM5 model also does a good job here, with an overall ranking of No.1, and also compares well with the reanalyses before satellite, especially for the storm track fields. Again run 1 of the same model does not perform as well, with an overall rank of #14. The CNRM model is also good at catching the relationship between the mean flow and storm tracks (No.2). The 5 runs of the CCCMA_t47 model again display a broad range of overall ranking, ranging from #8 to #22.Given such ranges between different runs made by the same model, one again has to conclude that the differences between the models may not be significant.

As mentioned above, Fig. 3.12 shows large spreads in amplitude among the model momentum flux variability. However, Fig. 3.11 also indicates large spreads in the amplitude of the mean flow variability. To see whether the two are related, we normalize the eddy variability by the amplitude of the mean flow variability for IPCC runs to be compared with the reference, to see if the broad amplitude range could be improved. In

Fig. 3.17, we show the momentum flux case only. Compared with Fig. 3.12, the range in magnitude of each normalized cluster is smaller, and the clusters tend to be more compact for all 4 leading modes, implying the improvement of amplitude behaviors for eddy momentum flux case. However, similar improvements are not found for the other storm track fields (not shown).

It is of interest to point out that among all the runs of different models used in this study, there is one model group, CCCMA_CGCM3_1_t47, containing 5 individual runs provided by Canadian Center for Climate Modeling and Analysis. These runs are indicated by the square symbols in Fig. 3.11 to Fig. 3.16. To put the spread exhibited by the IPCC AR4 models in Fig. 3.11 to Fig. 3.16 in proper context, we think it could be suggestive to investigate the spread among the different runs from experiments made with the same model to compare with the spread shown above. Here we choose the 300-hPa momentum flux field pattern in the SVD analysis with 300mb streamfunction to present the spread in Fig. 3.18. In Fig. 3.18, each run has been treated as a reference and four points for the four other runs could be plotted based on that reference run. We have five different runs, thus there are 20 points plotted in each Taylor diagram for the first 4 leading modes. Different color of points demonstrates comparison based on different reference run. Apparently, the average correlation of the cluster is pretty high compared with that in Fig. 3.12, which is what we expect since for the same model, different runs share the same forcing and same dynamic core, their relationship should be more robust than that for different models. However the spread of the amplitude in Fig. 3.18 is quite broad around the reference point, which is similar to or even broader than the amplitude spread shown in Fig. 3.12. This implies that the amplitude spread found in the coupled model results when compared with ncepa might not necessarily indicate model amplitude bias.

3.5 Conclusions

In this chapter, an attempt has been made to investigate not only the mean flow, but also the midlatitude transient eddy variability for both IPCC AR4 coupled models' climate outputs and reanalysis data from different time periods using the empirical orthogonal function (EOF) and singular value decomposition (SVD) analysis. The purpose of this study is to know how much confidence we can have in the model simulated relationship between the eddies and the mean flow for the CMIP3 coupled GCM models before we proceed to further examine model results for global warming research.

The reanalysis data has been separated into two time period, one is for the period of before-satellite, and the other is for after-satellite. Results suggest that no matter for before or after satellite, both the total variance or the variance distribution of EOF modes in both ERA40 and NCEP are quite close, for both the mean flow and storm track variability. However the reanalysis after-satellite carries larger magnitude of variations than reanalysis before-satellite. This is reasonable because in both reanalysis data, more climate variation could be captured by assimilating the satellite data into original analysis data, even though these two reanalysis datasets are processed in different ways. Therefore we expect that the reanalysis after-satellite has been improved compared with data before-satellite.

To increase the level of confidence that can be placed in model-based climate forecasts, apart from the time-mean state of climate, assessing how models perform in simulating temporal variability is also important. By using the mid-latitude transient eddy variability as the temporal variability, and diagnosing the relationship between temporal variability of the eddies and the time-mean state of climate, we find that the improvement of coupled model not only could be seen in the mean-time composite climate, also could be reflected in the transient eddy variability, at least in terms of the magnitude of the variability. The comparison between the GFDL R30 runs (which was from an earlier generation of model) and the CMIP3 model outputs suggests that most of the new runs have larger variance than the old ones, which might be partly due to more sophisticated model parameterizations and general increase in computational resources which allows for higher model resolution.

The reanalysis before satellite data is different from the reanalysis after satellite, which causes a spread between these reanalysis from different time periods. For individual mean flow field or the storm track variability, the IPCC AR4 model outputs are mostly clustered around the reanalysis before satellite, suggesting that the uncertainty of these coupled models in simulating either low-frequency mean flow or transient eddy variability might be at the similar level with the uncertainty of the reanalysis data before satellite relative to that after. The same conclusion could be obtained for the SVD analysis studying the interaction between the mean flow and storm track variability since the model outputs and reanalysis before satellite are also in a cluster. These results can be interpreted two ways: either 1) the reanalysis data before satellite could be quite far from observations, or 2) if we believe that the pre-satellite reanalysis data are of high quality, pretty high confidence could be placed in simulation results of these coupled models. We believe that the second interpretation is more likely (at least for the Northern Hemisphere) because the reanalysis datasets use a consistent and comprehensive data assimilation system to re-analyze all the available observations world-wide, no matter if the satellite data is involved.

Since some models have several individual runs, this gives us an opportunity to examine the uncertainty in our analyses based on results made with the same model. Thus the spread in the results computed based on one model, CCCMA_CGCM3_1_t47, containing 5 individual runs has been investigated. The spread of the amplitude for the 5 individual runs in this model is quite broad around the reference point. It is similar with or even broader than the amplitude spread in the multiple model runs. This implies that for these coupled IPCC AR4 models, the amplitude in the variability within one model could be a big uncertainty with a magnitude comparable to the spread among different models. Thus the spread in amplitude found in Figs. 3.11 to 3.16 does not necessarily indicate model bias compared to ncepa, but could just be indicative of the spread due to the limited number of months of data included in each sample This is supported by results shown in Tables 3.4 and 3.5, which show that different runs made by the same models display a broad range of performance, suggesting that the differences in performance between the different models may not be significant.

Variables	piece	Mode 1	Mode 2	Mode 3	Total
sf300	**refer**	**9.60E+12 (0.287)**	**4.51E+12 (0.135)**	**3.08E+12 (0.092)**	**3.34E+13**
	ncepb	7.12E+12 (0.22)	4.64E+12 (0.144)	3.58E+12 (0.11)	3.22E+13
	era40b	7.48E+12 (0.226)	4.67E+12 (0.141)	3.64E+12 (0.11)	3.31E+13
	era40a	1.07E+13 (0.30)	5.21E+12 (0.15)	3.12E+12 (0.088)	3.55E+13
uv300	**refer**	**61.52 (0.12)**	**41.52 (0.081)**	**35.37 (0.069)**	**512.65**
	ncepb	39.49 (0.094)	34.45 (0.082)	29.41 (0.07)	420.08
	era40b	50.10 (0.10)	39.78 (0.081)	32.91 (0.067)	491.14
	era40a	60.87 (0.11)	44.85 (0.081)	40.05 (0.072)	533.97
vsq300	**refer**	**372.43 (0.18)**	**192.56 (0.091)**	**173.52 (0.082)**	**2116.07**
	ncepb	350.00 (0.19)	190.26 (0.11)	157.95 (0.088)	1794.86
	era40b	333.86 (0.17)	208.91 (0.11)	173.77 (0.089)	1952.42
	era40a	338.20 (0.16)	213.26 (0.099)	185.26 (0.086)	2154.15
vt700	**refer**	**2.04 (0.16)**	**1.18 (0.091)**	**0.89 (0.068)**	**13.02**
	ncepb	1.95 (0.16)	1.43 (0.12)	0.85 (0.071)	12.03
	era40b	1.92 (0.15)	1.63 (0.13)	0.93 (0.072)	12.91
	era40a	1.99 (0.15)	1.35 (0.099)	0.98 (0.072)	13.61

Table 3.1: Variance of the leading 3 EOF modes for the 4 fields: 300-hPa streamfunction (sf300), 300-hPa momentum flux (uv300), 300-hPa meridional velocity square (vsq300) and 700-hPa heat flux (vt700). The right column is the total variance for each of the 4 reanalysis datasets. The number in the bracket is the contribution of each mode to the total variance.

Model I.D.	Marker symbol
NCEP_before	☆
ERA40_before	☆
ERA40_after	☆
1. BCC_CM1_1	◇
2. BCC_CM1_2	◇
3. BCC_CM1_3	◇
4. BCC_CM1_4	◇
5. CCCMA_CGCM3.1_T63	□
6. CCCMA_CGCM3.1_T47_1	□
7. CCCMA_CGCM3.1_T47_2	□
8. CCCMA_CGCM3.1_T47_3	□
9. CCCMA_CGCM3.1_T47_4	□
10. CCCMA_CGCM3.1_T47_5	□
11. CNRM_CM3	+
12. 15. CSIRO_Mk3.0_1	*
13. 16. CSIRO_Mk3.0_2	*
14. 17. CSIRO_Mk3.5	*
15. 18. GFDL_CM2.0	○
16. 19. GFDL_CM2.1	○
17. 20. GISS_AOM	×
18. GISS_EH	×
19. GISS_ER	×
20. IAP_FGOALS1.0g	△
21. INM_CM3.0	▽
22. IPSL_CM4_1	▷
23. IPSL_CM4_2	▷
24. MIROC3.2(hires)	◁
25. MIUB_ECHO_G	+
26. MPI_ECHAM5_1	⬡
27. MPI_ECHAM5_2	⬡
28. MRI_CGCM2.3.2a	*

Table 3.2: The symbols for the 28 runs of IPCC AR4 models and the reanalysis datasets from different periods shown in the Taylor diagrams.

	Square covariance percentage (%)			
SVD pairs	1st mode	2nd mode	3rd mode	4th mode
sf300-uv300	47.8%	13.3%	10.5%	8.6%
sf300-vsq300	49.5%	12.8%	11.7%	7.0%
sf300-vt700	50.2%	10.9%	9.5%	8.1%

Table 3.3: The square covariance percentage that each SVD pair accounts for in NCEP after-satellite data.

	sf300		uv300		vsq300		vt700		
NCEPb	**0.40**		**0.50**		**0.38**		**0.41**		
ERA40b	**0.37**		**0.49**		**0.35**		**0.41**		
ERA40a	**0.14**		**0.18**		**0.16**		**0.18**		
MODEL		rank		rank		rank		rank	Overall rank
bcc_1	0.70	#25	0.92	#26	0.87	#25	0.98	#25	#25
bcc_2	0.70	#25	0.92	#26	0.87	#25	0.98	#25	#25
bcc_3	0.80	#28	0.92	#26	0.87	#25	0.98	#25	#28
bcc_4	0.75	#27	0.91	#25	0.87	#25	0.98	#25	#27
cccma_t63	0.60	#23	0.57	#11	0.37	#5	0.51	#15	#15
cccma_t47_1	0.58	#21	0.63	#20	0.38	#8	0.45	#11	#18
cccma_t47_2	0.56	#17	0.66	#22	0.37	#5	0.43	#7	#13
cccma_t47_3	0.56	#17	0.59	#17	0.37	#5	0.43	#7	#11
cccma_t47_4	0.49	#10	0.54	#8	0.33	#3	0.41	#6	#4
cccma_t47_5	0.50	#11	0.53	#7	0.34	#4	0.40	#4	#3
cnrm	0.47	#7	0.59	#17	0.52	#17	0.39	#2	#9
csiro_mk3.0_1	0.48	#8	0.57	#11	0.46	#13	0.46	#12	#10
csiro_mk3.0_2	0.56	#17	0.57	#11	0.48	#14	0.51	#17	#16
csiro_mk3.5	0.46	#6	0.51	#4	0.49	#15	0.40	#4	#5
gfdl_cm2.0	0.40	#3	0.51	#4	0.45	#11	0.43	#7	#2
gfdl_cm2.1	0.52	#15	0.47	#1	0.45	#11	0.43	#7	#7
giss_aom	0.62	#24	0.64	#21	0.66	#23	0.61	#22	#24
giss_e_h	0.48	#8	0.57	#11	0.53	#19	0.50	#17	#16
giss_e_r	0.50	#11	0.59	#17	0.63	#20	0.49	#13	#19
iap	0.59	#22	0.69	#24	0.52	#17	0.82	#24	#23
inm	0.51	#13	0.58	#15	0.63	#20	0.51	#17	#22
ipsl_1	0.54	#16	0.55	#9	0.64	#22	0.51	#17	#20
ipsl_2	0.42	#4	0.50	#3	0.72	#24	0.59	#21	#14
miroc3_2_hires	0.56	#17	0.56	#10	0.39	#9	0.38	#1	#8
miub_echo_g	0.51	#13	0.52	#6	0.29	#1	0.49	#13	#6
mpi_1	0.44	#5	0.58	#15	0.39	#9	0.53	#20	#12
mpi_2	0.34	#1	0.49	#2	0.32	#2	0.39	#2	#1
mri	0.38	#2	0.68	#23	0.50	#16	0.63	#23	#20

Table 3.4: The root-mean-square differences of the 1st EOF regression between IPCC AR4 model simulations (colorful signs), other reanalyses of different time period (pentagrams) and post-satellite NCEP reanalysis (reference point) shown in Taylor diagrams.

	sf300-uv300		sf300-vsq300		sf300-vt700	
NCEPb	**0.48**		**0.46**		**0.45**	
ERA40b	**0.48**		**0.46**		**0.46**	
ERA40a	**0.31**		**0.32**		**0.31**	
MODEL		rank		rank		rank
cccma_t63	0.84	#24	0.87	#24	0.81	#24
cccma_t47_1	0.83	#23	0.82	#23	0.78	#22
cccma_t47_2	0.82	#22	0.79	#19	0.75	#17
cccma_t47_3	0.81	#20	0.80	#21	0.77	#21
cccma_t47_4	0.67	#9	0.69	#11	0.64	#10
cccma_t47_5	0.71	#13	0.70	#13	0.66	#12
cnrm	0.54	#3	0.53	#3	0.53	#4
csiro_mk3.0_1	0.47	#2	0.46	#2	0.47	#2
csiro_mk3.0_2	0.46	#1	0.45	#1	0.43	#1
csiro_mk3.5	0.75	#16	0.71	#14	0.75	#17
gfdl_cm2.0	0.70	#11	0.68	#10	0.65	#11
gfdl_cm2.1	0.78	#18	0.77	#17	0.74	#16
giss_aom	0.72	#14	0.75	#16	0.72	#15
giss_e_h	0.67	#9	0.64	#9	0.62	#9
giss_e_r	0.56	#5	0.56	#6	0.54	#5
iap	0.77	#17	0.81	#22	0.79	#23
inm	0.62	#8	0.60	#7	0.60	#7
ipsl_1	0.74	#15	0.74	#15	0.71	#14
ipsl_2	0.61	#7	0.61	#8	0.61	#8
miroc3_2_hires	0.81	#20	0.79	#19	0.75	#17
miub_echo_g	0.78	#18	0.77	#17	0.76	#20
mpi_1	0.70	#11	0.69	#11	0.66	#12
mpi_2	0.56	#5	0.53	#3	0.52	#3
mri	0.55	#4	0.53	#3	0.59	#6

	uv300-sf300		vsq300-sf300		vt700-sf300		
NCEPb	**0.80**		**0.71**		**0.65**		
ERA40b	**0.82**		**0.70**		**0.61**		
ERA40a	**0.28**		**0.28**		**0.33**		
MODEL		rank		rank		rank	overall rank
cccma_t63	0.98	#21	0.81	#20	0.72	#15	#24
cccma_t47_1	0.98	#21	0.79	#18	0.75	#17	#21
cccma_t47_2	1.15	#24	0.89	#24	0.77	#20	#22
cccma_t47_3	1.09	#23	0.81	#20	0.80	#21	#22
cccma_t47_4	0.89	#17	0.59	#2	0.60	#6	#8
cccma_t47_5	0.86	#13	0.76	#16	0.58	#4	#13
cnrm	0.72	#2	0.66	#7	0.59	#5	#2
csiro_mk3.0_1	0.84	#10	0.60	#3	0.62	#9	#3
csiro_mk3.0_2	0.81	#8	0.63	#6	0.68	#12	#4
csiro_mk3.5	0.78	#7	0.66	#7	0.48	#1	#11
gfdl_cm2.0	0.69	#1	0.61	#5	0.64	#11	#6
gfdl_cm2.1	0.91	#19	0.66	#7	0.71	#14	#16
giss_aom	0.87	#14	0.79	#18	0.76	#18	#18
giss_e_h	0.85	#12	0.68	#11	0.60	#6	#9
giss_e_r	0.75	#3	0.75	#15	0.60	#6	#5
iap	0.84	#10	0.85	#23	1.04	#24	#20
inm	0.77	#5	0.68	#11	0.72	#15	#7
ipsl_1	0.83	#9	0.82	#22	0.76	#18	#17
ipsl_2	0.76	#4	0.77	#17	0.81	#22	#12
miroc3_2_hires	0.87	#15	0.66	#7	0.51	#2	#15
miub_echo_g	0.88	#16	0.58	#1	0.84	#23	#18
mpi_1	0.97	#20	0.72	#14	0.63	#10	#14
mpi_2	0.77	#5	0.60	#3	0.57	#3	#1
mri	0.89	#17	0.70	#13	0.69	#13	#9

Table 3.5: Same as Table 3.4 except SVD regression. The first table is for the mean flow homogeneous regression, and the second one shows the storm track heterogeneous regression. There are no BCC runs in these Tables because of their very poor storm track variances. The overall rank in second table is the total rank for both tables.

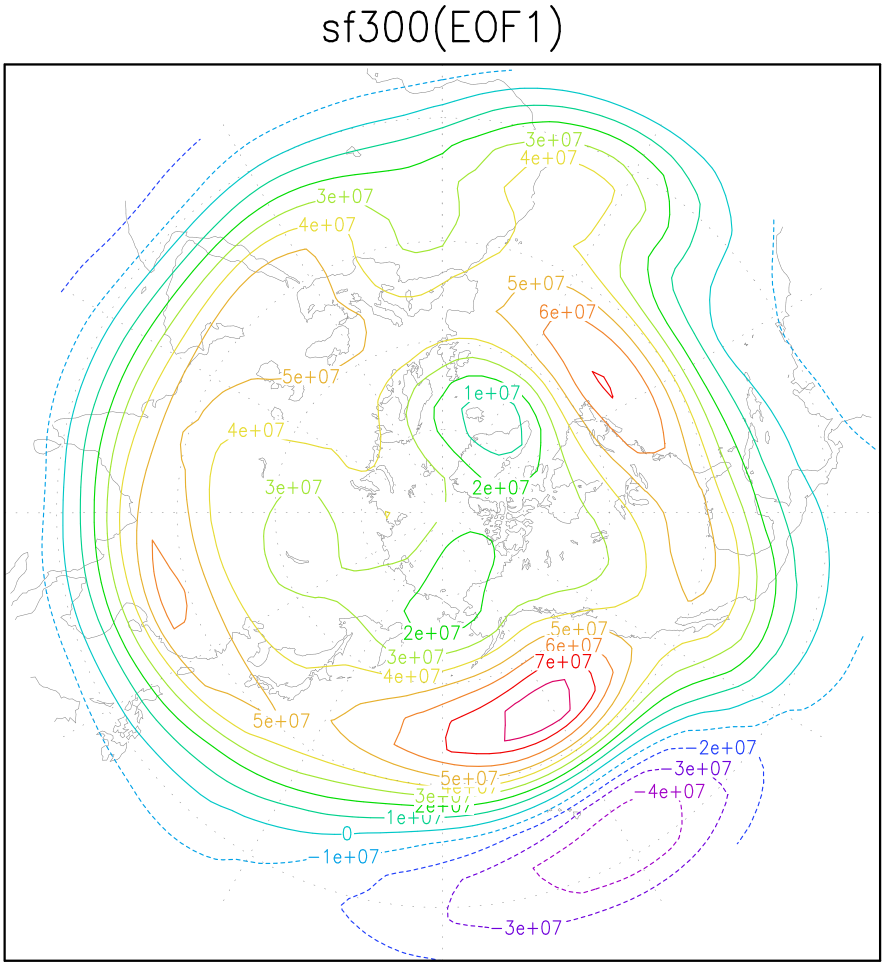

Figure 3.1: The leading EOF mode of 300-hPa streamfunction anomalies of NCEP reanalysis after satellite.

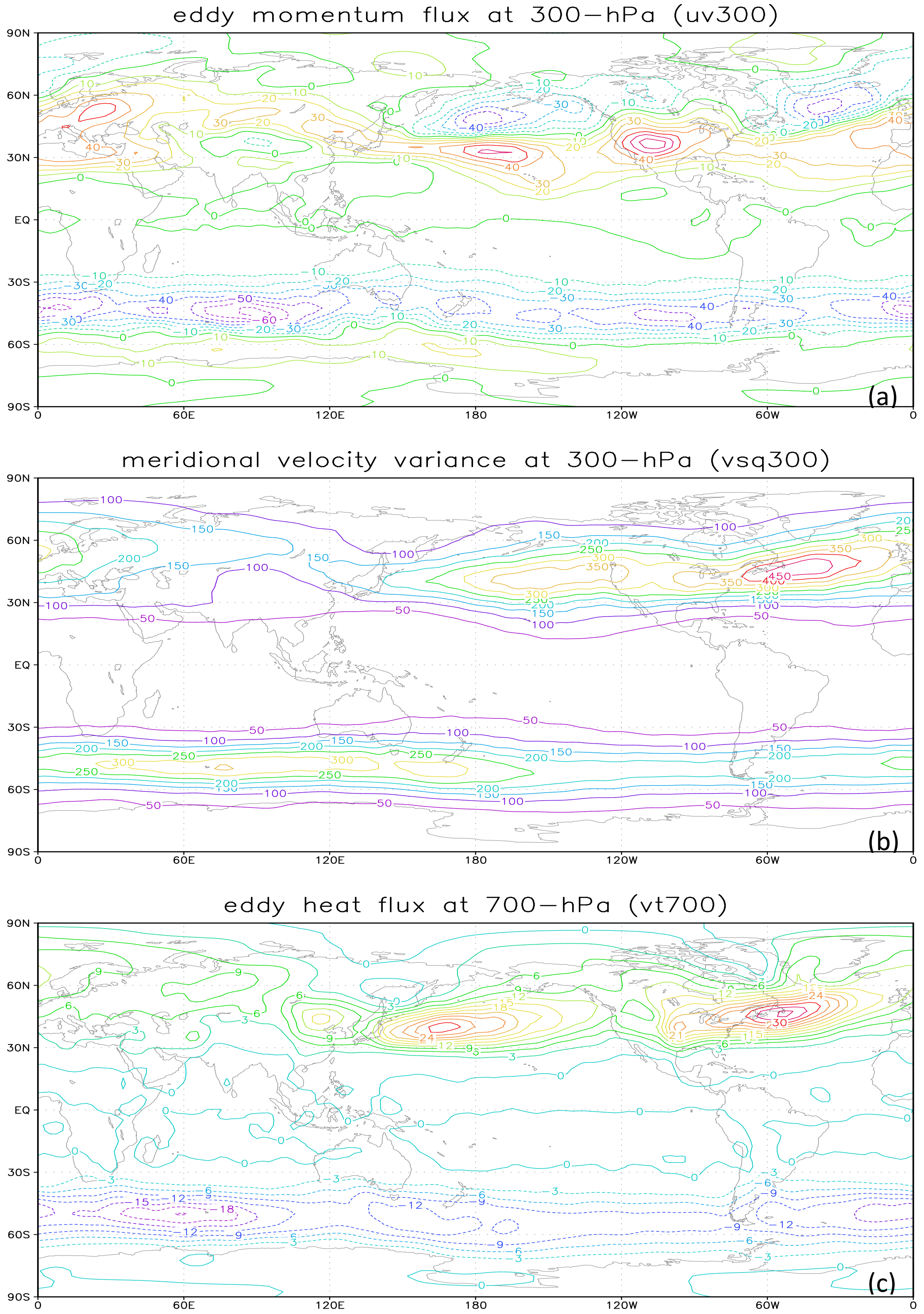
eddy momentum flux at 300−hPa (uv300)

meridional velocity variance at 300−hPa (vsq300)

eddy heat flux at 700−hPa (vt700)

Figure 3.2: The DJF (December, January and February) climatology of (a) 300-hPa eddy momentum flux, (b) 300-hPa meridional velocity variance, and (c) 700-hPa eddy heat flux in NCEP reanalysis from 1979 to 2007.

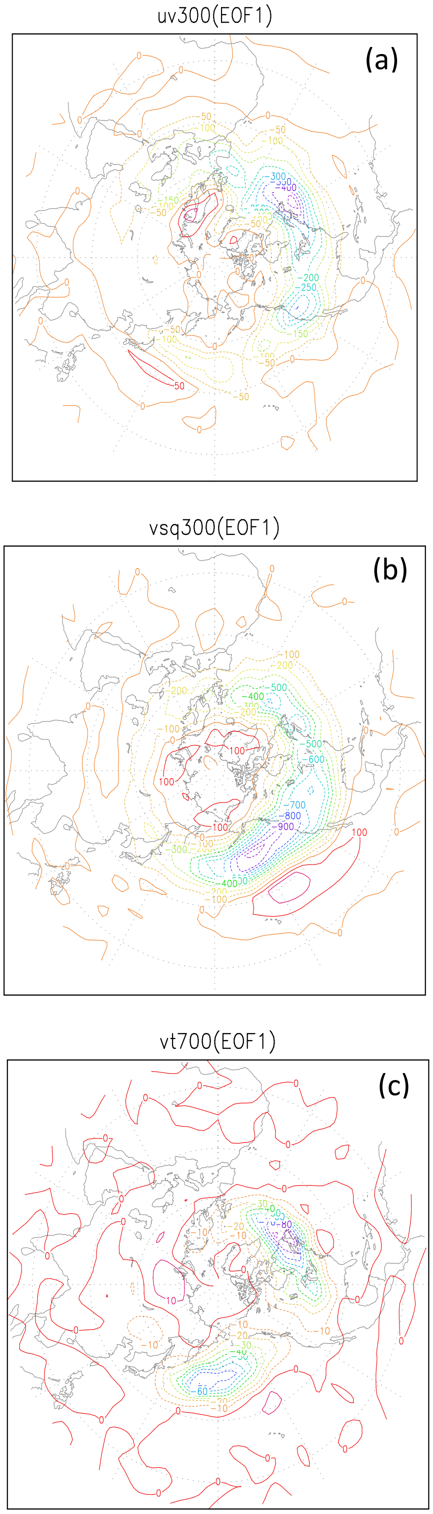

Figure 3.3: The leading EOF modes of NCEP reanalysis after satellite for anomalies of 300-hPamomentum flux (a), 300-hPa meridional velocity variance (b) and 700-hPa heat flux (c), respectively.

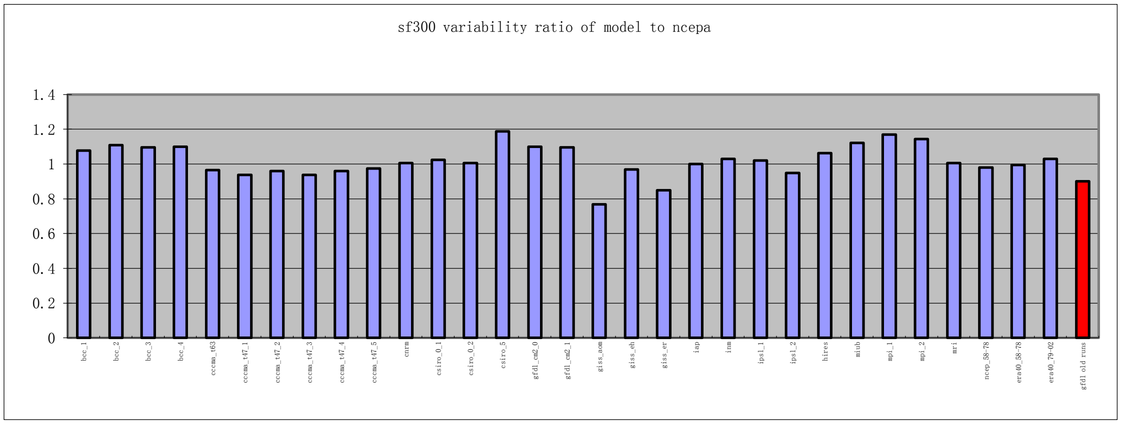

sf300 variability ratio of model to ncepa

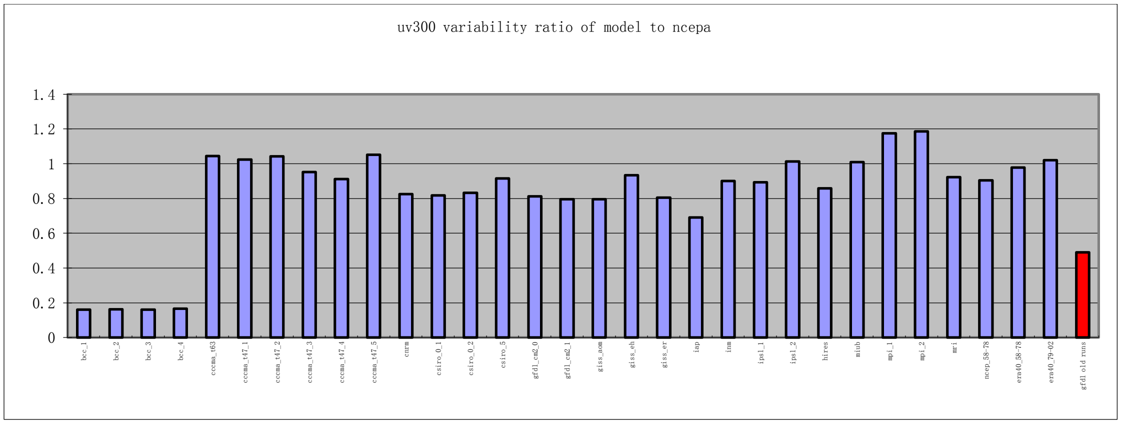

uv300 variability ratio of model to ncepa

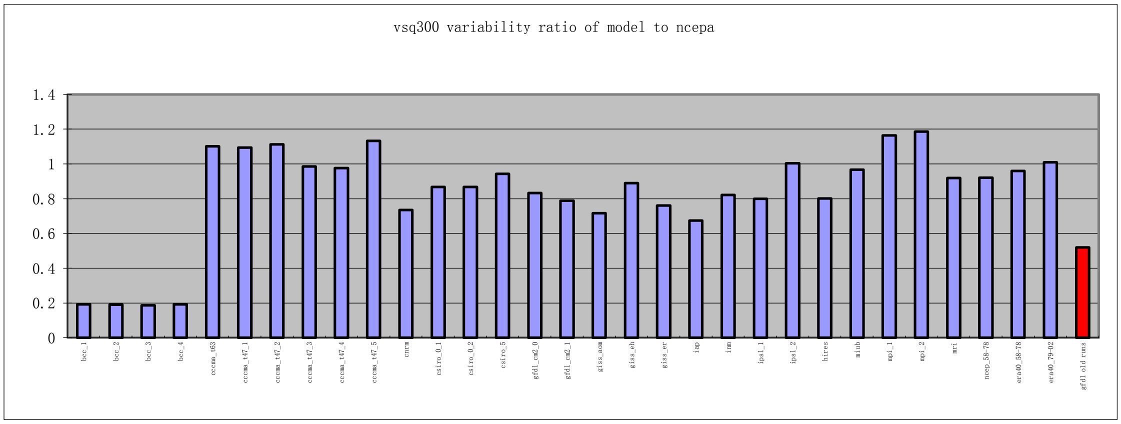

vsq300 variability ratio of model to ncepa

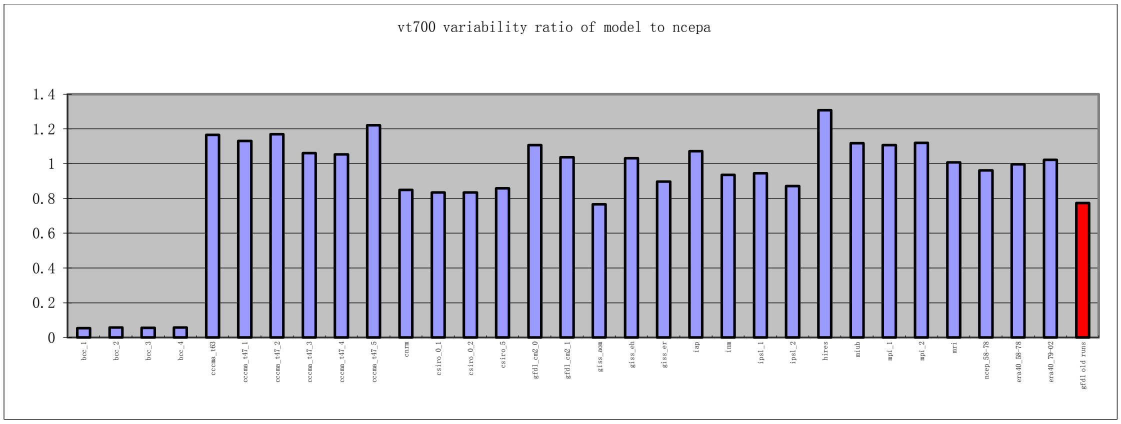

Figure 3.4: Bar graph comparing the total variability of the model runs to the NCEP reanalysis after satellite for 4 variables. The variability is the square root of the total variance normalized by NCEP variance. Red column represents GFDL-R30 runs.

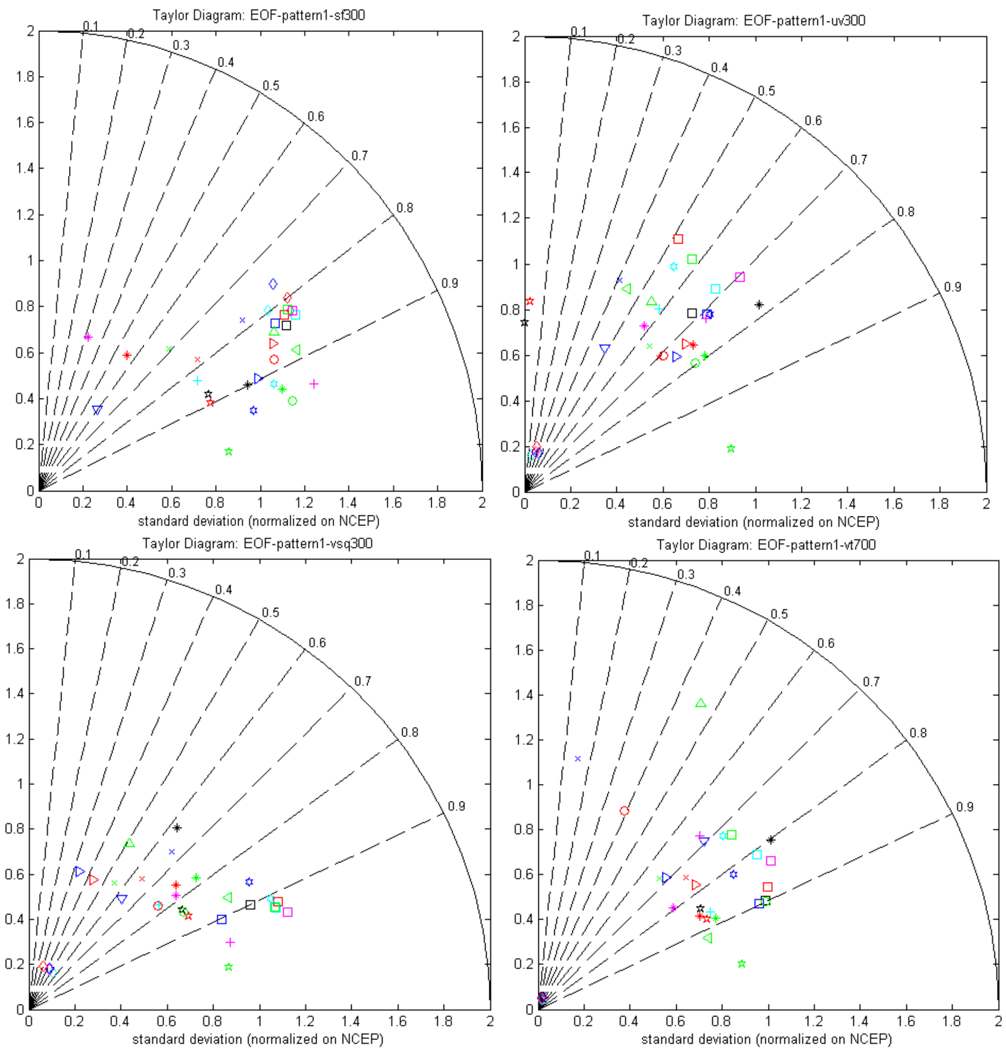

Figure 3.5: Pattern statistics describing the 1st EOF pattern simulated by 28 IPCC model runs and three reanalysis datasets compared with the 1st EOF pattern of NCEP reanalysis after satellite. The correlation between the two fields is given by the azimuthal position of each symboll, the radial distance from the origin is the standard deviation of the model pattern normalized by NCEP standard deviation after-satellite. The normalized RMS error is the distance between each symbol and the reference point (1, 0).

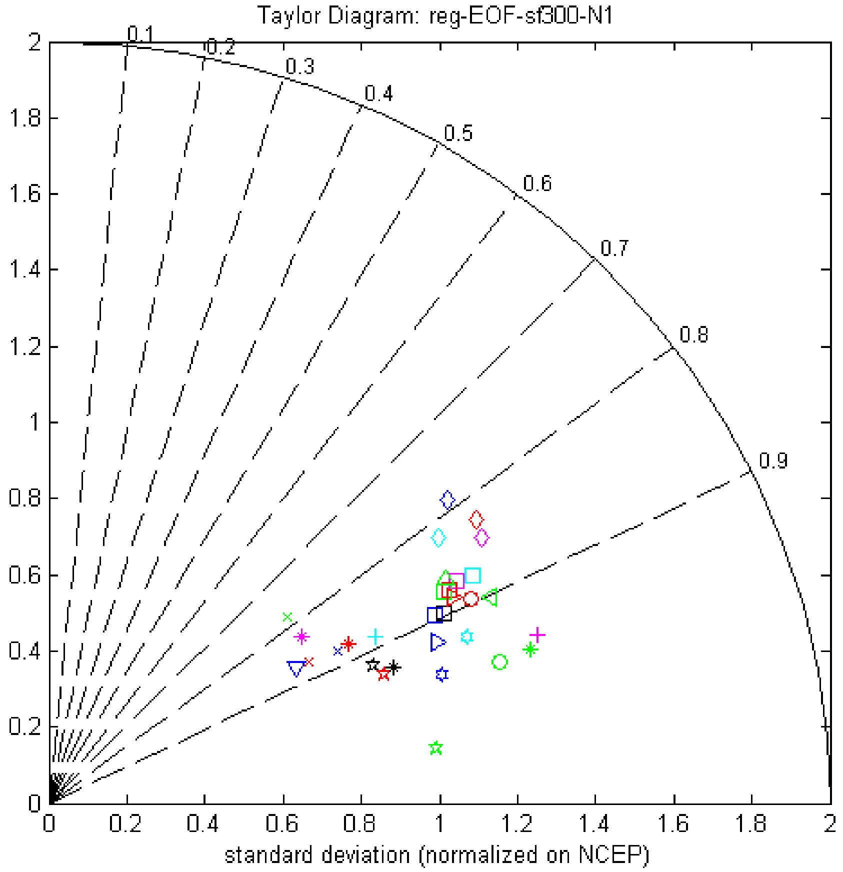

Figure 3.6: Same as Fig. 3.5, but for regression pattern computed based on the 1st EOF of sf300 of NCEP after satellite reanalysis.

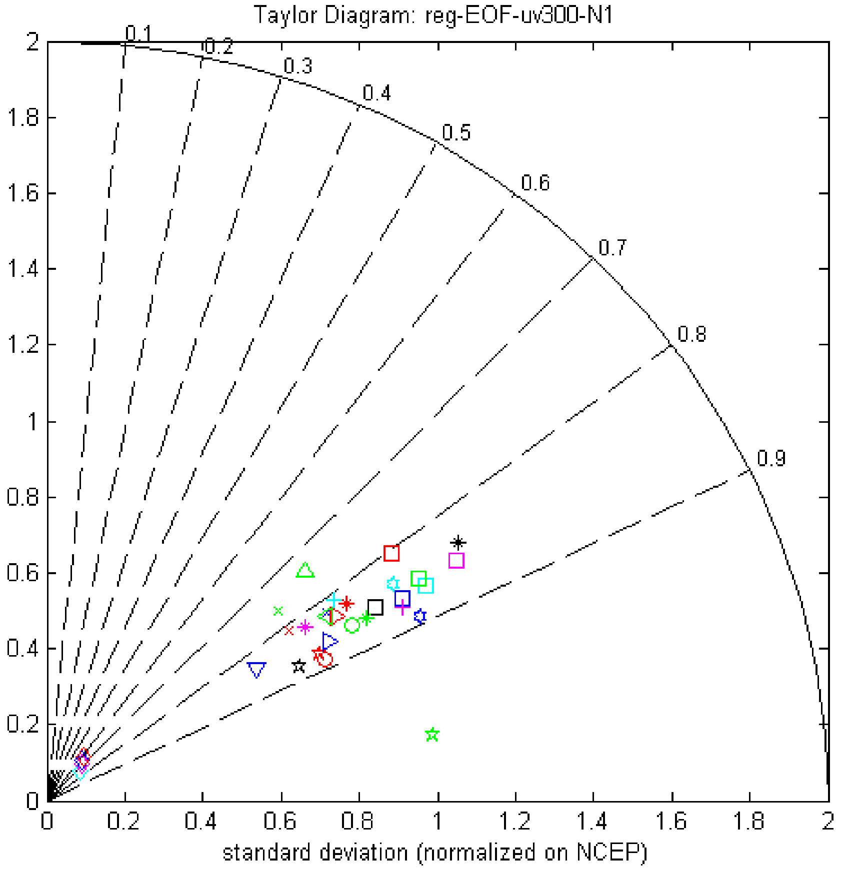

Figure 3.7: Same as Fig. 3.6 except for 300-hPa momentum flux.

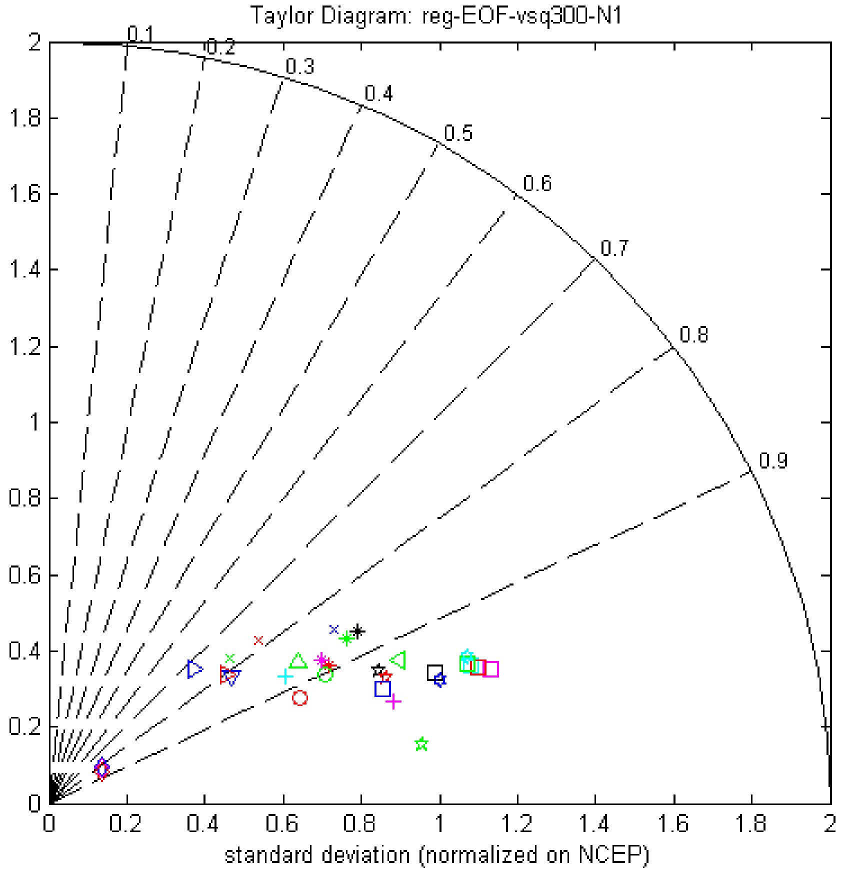

Figure 3.8: Same as Fig. 3.6 except for 300-hPa meridional velocity variance.

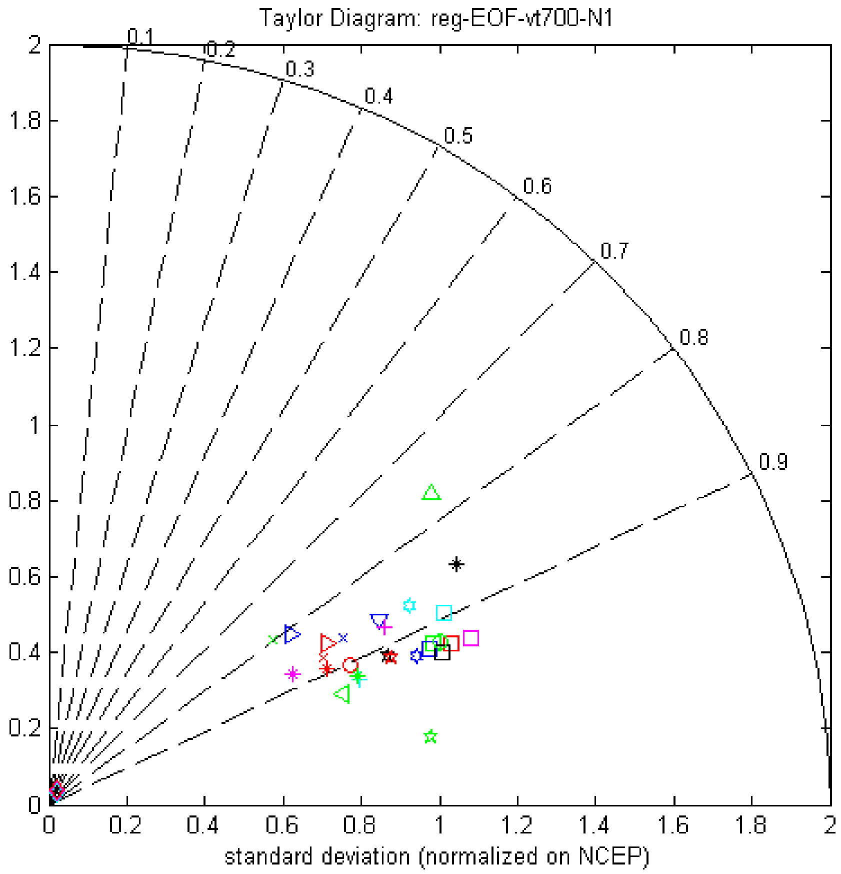

Figure 3.9: Same as Fig. 3.6 except for 700-hPa heat flux.

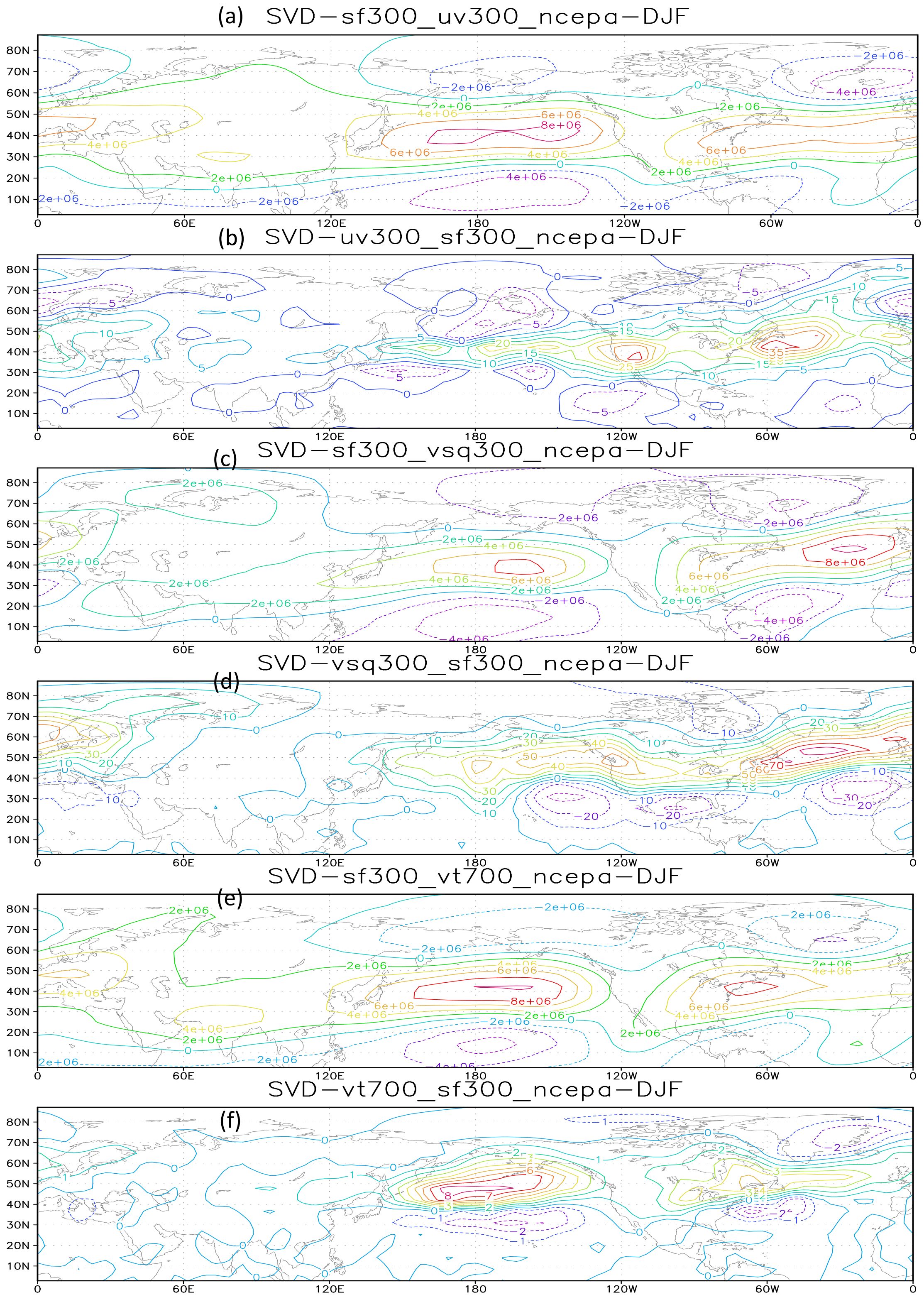

Figure 3. 10: The leading 1st pair of SVD patterns of the streamfunction and eddy variability for NCEP reanalysis from 1979 to 2007.

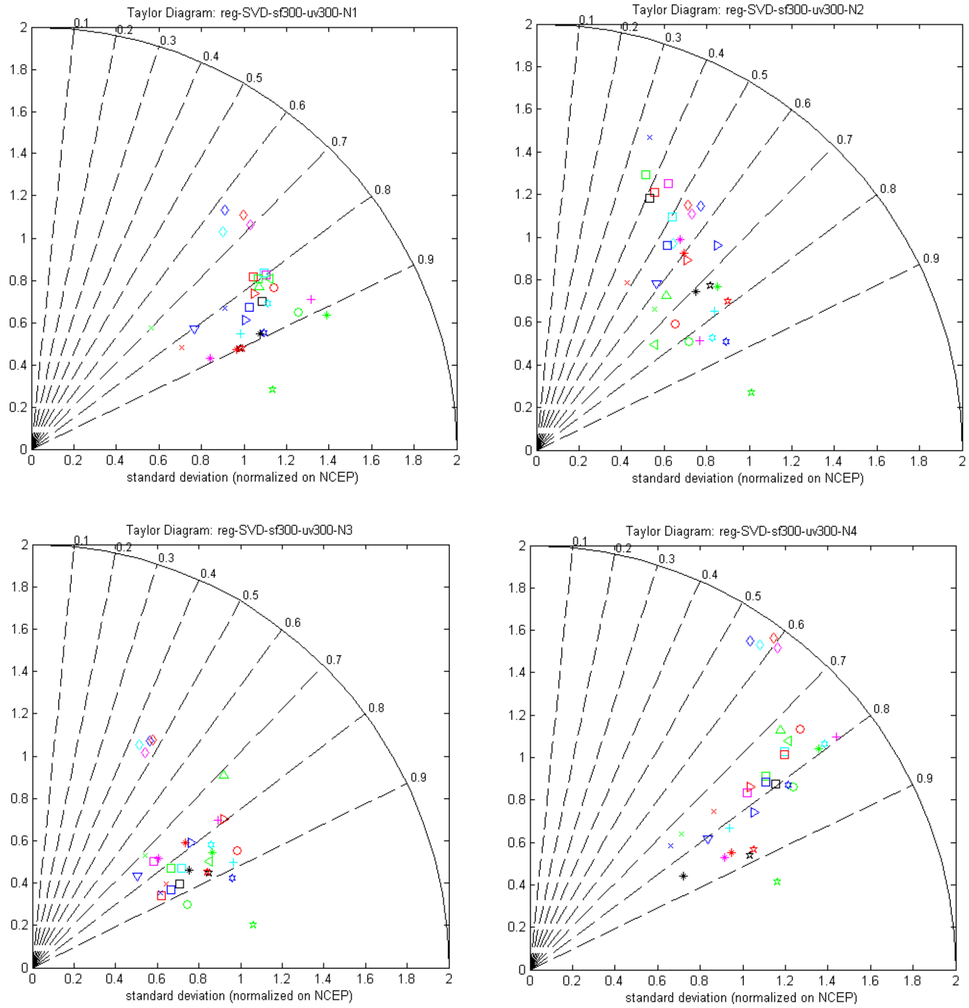

Figure 3.11: Pattern statistics describing the comparison between the regression of 300-hPa streamfunction simulated by 28 IPCC model runs (based on a time series described below) and the homogeneous regression of the NCEP reanalysis after satellite. This time series is produced from the projecttion of model sf300 onto after-satellite NCEP SVD mode of 300-hPa streamfunction based on two fields: sf300 and uv300.

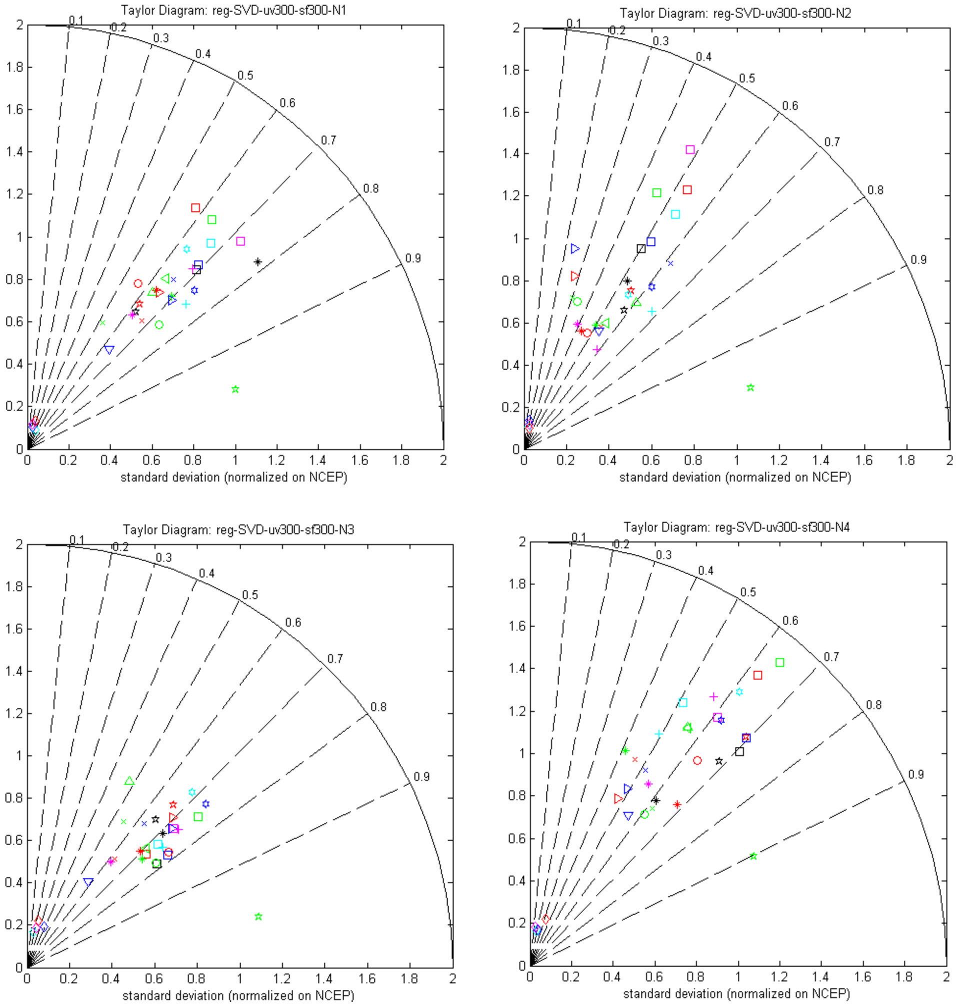

Figure 3.12: Pattern statistics describing the comparison between the regression of 300-hPa momentum flux simulated by 28 IPCC model runs (based on a time series described below) and the heterogeneous regression of the NCEP reanalysis after satellite. This time series is produced from the projection of model sf300 onto after-satellite NCEP SVD mode of 300-hPa streamfunction based on two fields: sf300 and uv300.

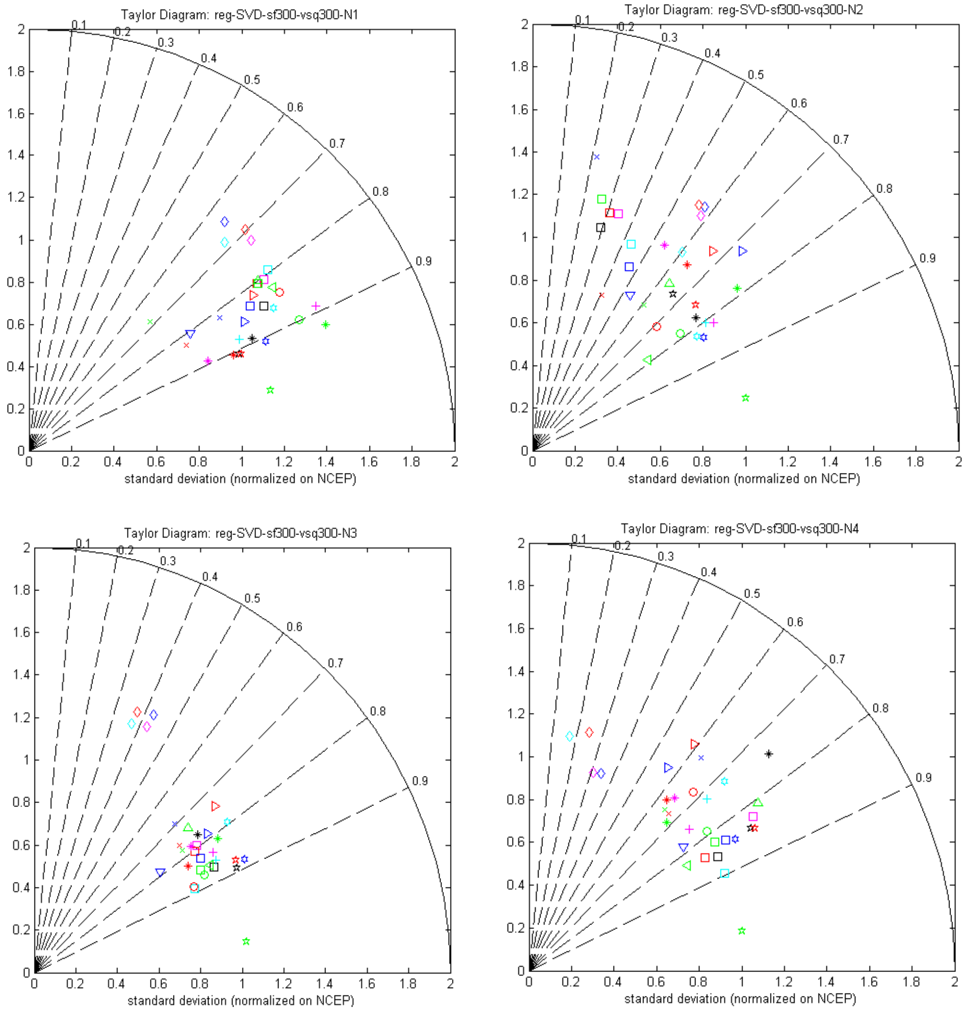

Figure 3.13: Same as Fig. 3.11 but for SVD mode based on sf300 and vsq300.

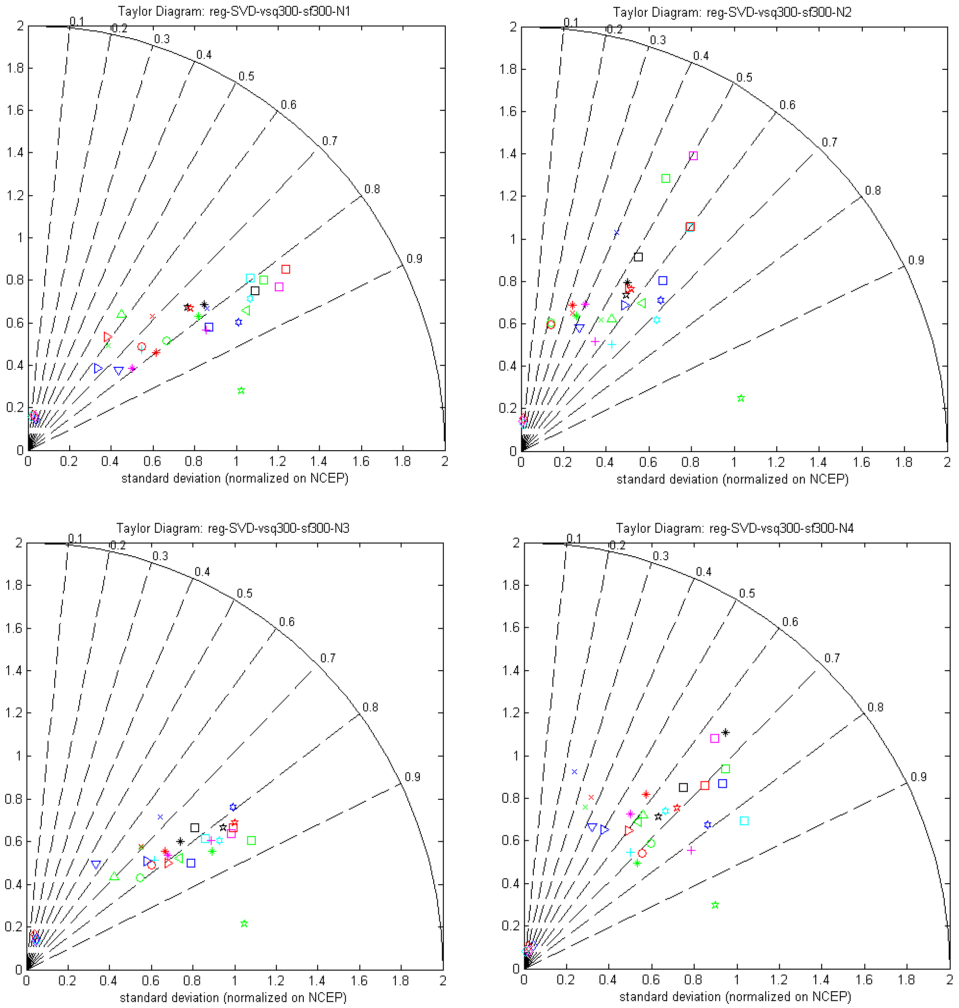

Figure 3.14: Same as Fig. 3.12, but for vsq300.

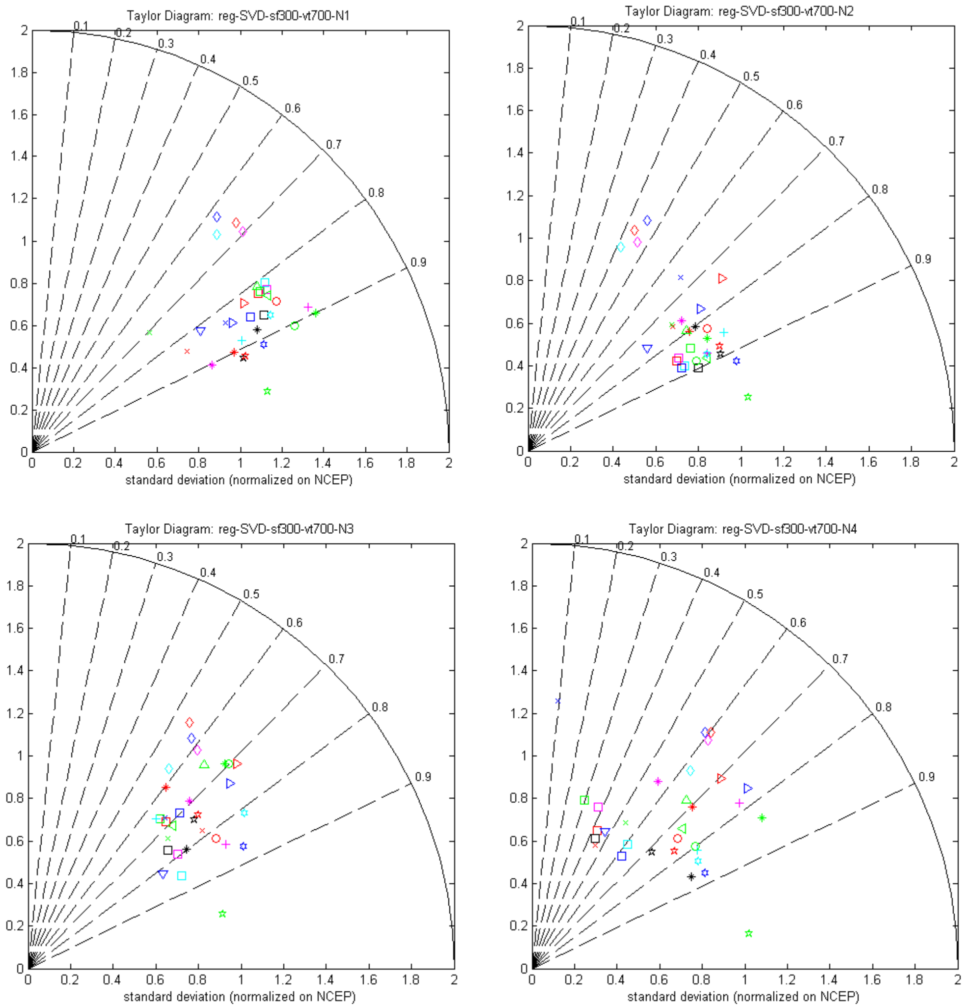

Figure 3.15: Same as Fig. 3.11 except for SVD between sf300 and vt700.

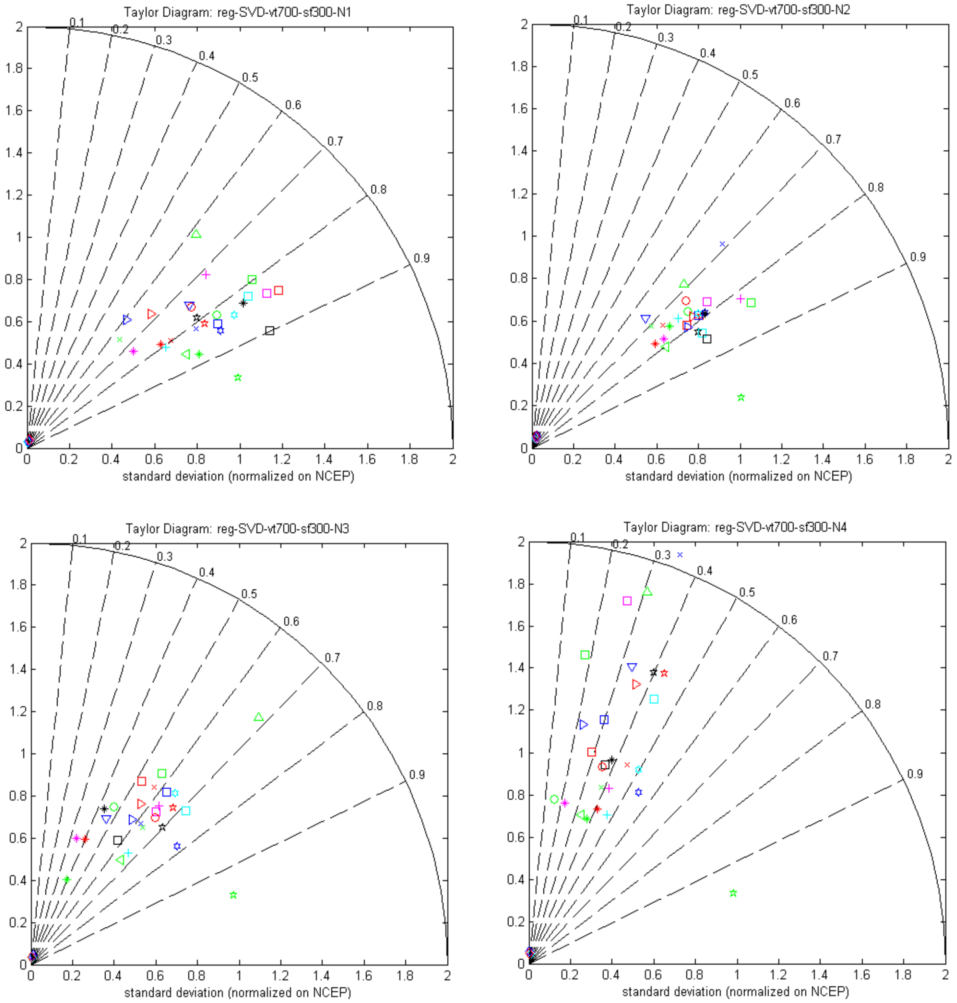

Figure 3.16: Same as Fig. 3.12, but for vt700.

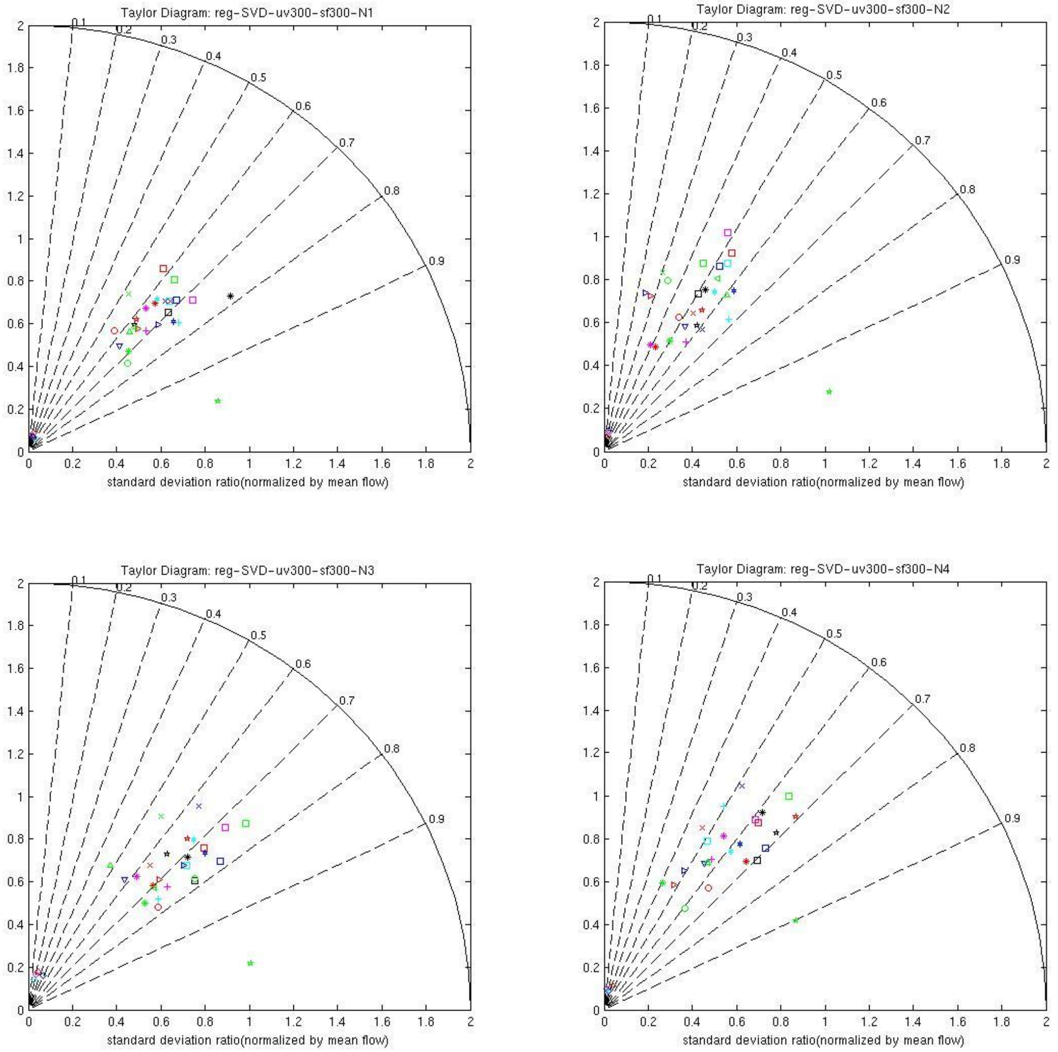

Figure 3.17: Same as Fig. 3.12 except that the amplitude of the momentum flux is normalized by that of the mean flow (Fig. 3.11).

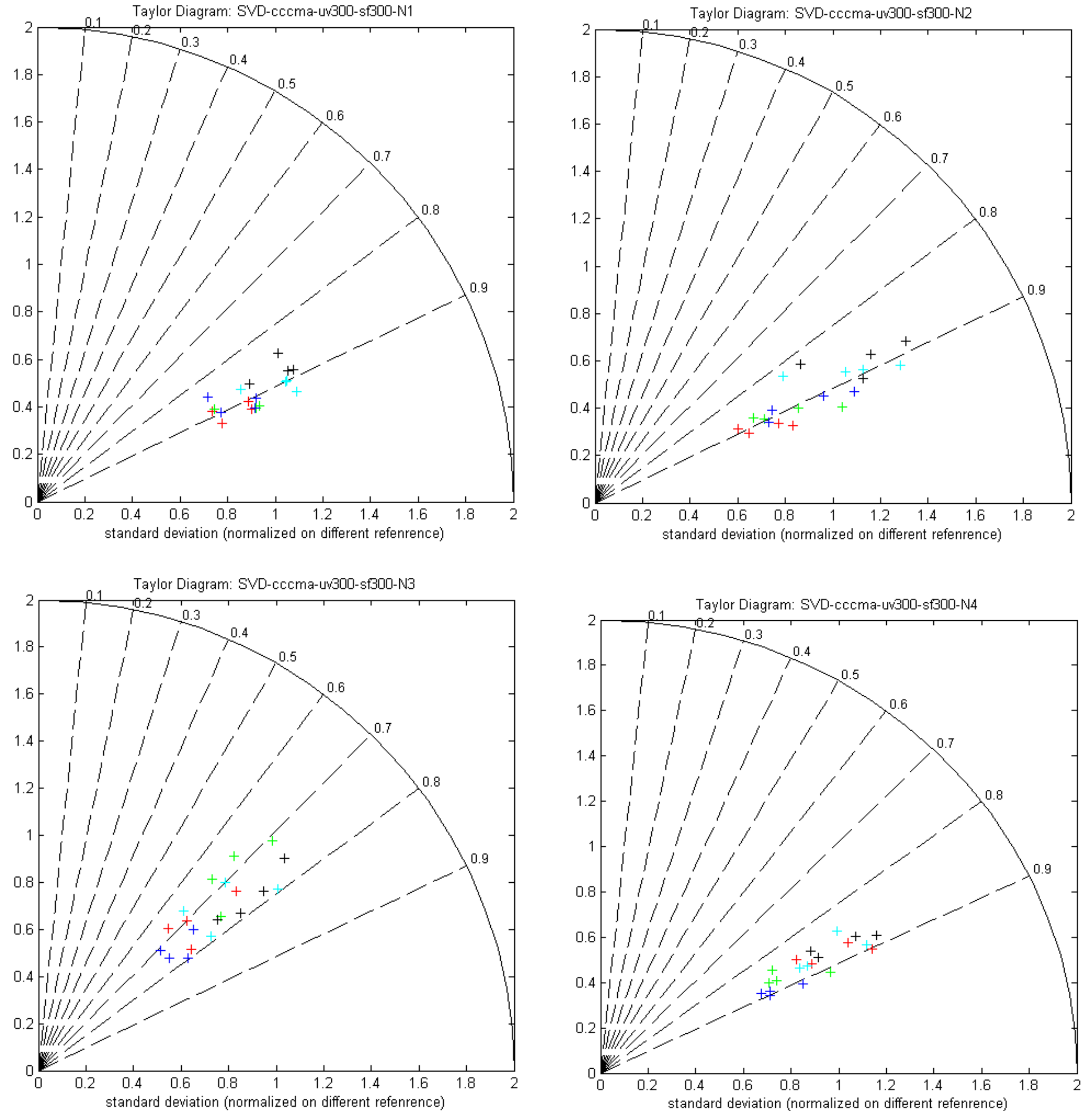

Figure 3.18: Pattern statistics describing the comparison the first 4 leading patterns of 300-hPa momentum flux field in the SVD analysis with 300mb streamfunction between 5 different runs of CCCMA_CGCM3.1_t47 model. Each run is treated as reference to be compared with the other four runs, thus giving 20 points.

Chapter 4 Diabatic damping of zonal index variations

4.1 Introduction

Numerous previous studies have shown that the dominant mode of interannual variability of the zonal wind in the Southern Hemisphere is an approximately equivalent barotropic dipole with maximum anomalies at 40^{o}S and 60^{o}S having opposite signs, representing north-south fluctuations in the position of the zonal-mean midlatitude jet about its time mean position at 50^{o}S (Kidson 1988; Karoly 1990; Hartmann and Lo 1998). This leading mode of the midlatitude zonal flow variability observed in the Southern Hemisphere is also readily simulated in numerical models (Robinson 1994; Yu and Hartmann 1993; Robinson 1996; Limpasuvan and Hartmann 1999).

The transient eddy momentum fluxes have a positive feedback on zonal-mean wind and this feedback between the zonal flow and eddy forcing acts to increase the persistence and low-frequency variance of the zonal index, which was suggested and confirmed by many observational studies (Shiotani 1990; Karoly 1990; Hartmann 1995; Kidson and Sinclair 1995; Feldstein and Lee 1998; Hartmann and Lo 1998). Furthermore, the importance of eddy momentum-zonal flow feedbacks has been studied by various modeling studies as well. Yu and Hartmann (1993) suggested that the long-term zonal wind variations result from a strong eddy momentum flux- zonal flow feedback by diagnosing output from a multilevel primitive equation model. Robinson (1994), using a two-level model, found that eddy momentum fluxes act as a positive feedback on very low frequency (periods longer than 30 days) imposed variability in the zonal index. Lorenz and Hartmann (2001) diagnosed the NCEP reanalysis data and confirmed such a positive eddy momentum flux-zonal flow feedback on low frequency variability, its strength and effects on zonal wind were estimated by a simple linear model as well.

Therefore, zonal index mode was maintained by this positive eddy-zonal wind feedback for a long timescale, and it is longer in GCMs than in observations or in the reanalysis data. Hartmann and Lo (1998) found that the timescales of the variations related to zonal index mode in the Southern Hemisphere is about 10 days for the unfiltered data for all seasons, by using ECMWF data. Feldstein (2000a) used the NCEP reanalysis to estimate the e-folding time associated with the intraseasonal zonal index time series around 18 days and 14days for the Northern Hemisphere winter and Southern Hemisphere summer, respectively. And Lorenz and Hartmann (2001) suggested that the observed e-folding time scale of the zonal index in the Southern Hemisphere is around 13 days. While for modeling work, Yu and Hartmann (1993) suggested that the zonal index in the Southern Hemisphere varied on timescales of hundreds of days in a multilevel primitive equation model, and these long-term variations were maintained by eddy forcing. In the particular cases of Polvani and Kushner (2002) and Kushner and Polvani (2004), the decorrelation timescale of their dry model's leading annular mode is extremely long (200-500 days) as compared to the timescale observed in the atmosphere. Gerber and Vallis (2007), and Gerber et al. (2008) also showed that the annular mode timescale was several times larger than those observed in dry models driven with the Held-Suarez forcings. These timescales of zonal index calculated from various models are much longer than those found in reanalysis or observations. In our model simulations (to be discussed below), we also found that the persistence of zonal index is quite long, and is much longer than those found in GCM runs. What is the reason for this substantial time scale gap?

One possible effect is the lack of moist process in our dry model experiments. As we mentioned in the paragraphs above, many studies have shown that transient eddy momentum flux provides a positive feedback on zonal index low frequency variations. However, as far as we know, no study has investigated the role that diabatic heating related with eddies play on mid-latitude jet variability. In this section, we will address this problem by diagnostic studies based on observation and reanalysis data, as well as conducting experiments using a dry idealized model.

In the current study, we will first provide a brief discussion of the data, then a short description of the idealized model we used, and some analysis about timescale comparison and regression studies (section 4.2). In section 4.3 we design three different experiments to mimic the diabatic heating associated with eddies in the model, then compare the timescale of zonal index in these experiments to the dry model runs. We will then discuss the dynamics involved in section 4.4. The conclusion will be presented in section 4.5.

4.2 Data and analysis

4.2.1 Data

For this study, we used the NCEP/NCAR and ERA40 reanalysis four-time-daily wind and temperature data on constant pressure levels. We used data for Southern Hemisphere summer (December-February; DJF) from December 1979 to February 2002 for ERA40, and to February 2009 for NCEP reanalysis on a $2.5^{o} \times 2.5^{o}$ latitude-longitude grid and 17 vertical levels (1000, 925, 850, 700, 600, 500, 400, 300, 250, 200, 150, 100, 70, 50, 30, 20, and 10 hPa). We also used NCEP and ERA40 precipitation rate to estimate the latent heating.

With respect to precipitation data, the GPCP daily (Dec 1996 – Feb 2009) and monthly (Dec 1979 – Feb 2001) precipitation was used as observation.

The wind, temperature and precipitation of a 100-year seasonal run of CAM3.1, as well as model results from 28 individual runs of 18 IPCC AR4 models (1961-2000) were also examined in this study as GCMs to be compared.

4.2.2 Idealized dry model description

In addition to analyzing all the data sources described above, we used an idealized dry model (Chang 2006) to conduct some idealized experiments. This model has been introduced in Chapter 2, but we will briefly describe it here. This model is based on the dynamical core of the Geophysical Fluid Dynamics Laboratory (GFDL) global spectral model (Held and Suarez 1994). Realistic orography, smoothed to model resolution (T42L20), is imposed. A land-sea mask is used, with stronger surface friction over land. The only forcing imposed to drive the model is Newtonian damping to a radiative equilibrium potential temperature profile (θ_E). In order to enhance the amplitude of eddies to be close to the realistic atmosphere, the target climate is imposed with the observed temperature profile (here we used NCEP reanalysis), while with reduced static stability (to mimic the impact of moist effect in a dry model) (4.3) and iteratively tuned heating forcing Q (which is fixed for each model run) (4.4) until a model climate close to θ_C is achieved..

$$\frac{D\theta}{Dt} = -\frac{\theta - \theta_E}{\tau} - \kappa\nabla^8\theta \tag{4.1}$$

$$\theta_E = \theta_C + \tau Q \tag{4.2}$$

$$\theta_C = \theta_{obs}(x, y, p) - Az(p) \tag{4.3}$$

$$Q_N = Q_{N-1} - \frac{2}{3}\frac{\bar{\theta}_{N-1} - \theta_C}{\tau}, N = 1,2,3, \ldots, \tag{4.4}$$

More details concerning the model formulation can be found in Chapter 2 and in Chang (2006). In this study, the control run is made with *A=0.65K/km* in (4.3).

4.2.3 Timescale comparison

To address the problems of very long timescale of low-frequency variation occurring in our idealized model simulations, we performed the timescale analysis of related zonal index mode in the Southern Hemisphere based on reanalysis data, observations, GCMs and idealized dry model experiment results. Gerber et al (2008), presented a simple procedure to compute the e-folding time scale of the annular mode autocorrelation function which could concisely quantify the strength of the low-frequency variability in a model experiment and be computed easily in practice. In this procedure, an empirical estimate (τ_N) of the "true" autocorrelation time scale for N days is computed by fitting the autocorrelation function $r_N(t)$ to a simple exponential. In particular, τ_N is chosen so as to minimize the RMS distance between $r_N(t)$ and $e^{-\frac{t}{\tau_N}}$ for all t such that $r_N(t) > e^{-1}$. Using this methodology, we calculated the autocorrelation timescale of the zonal index mode (also known as jet shift mode), as well as that of the precipitation pattern related to the Southern Hemisphere jet shift, and eddy momentum fluxes variability as well.

In this study, the reanalysis data used ranges from December 1979 to February 2002 (DJF), consisting of 2076 days. The GPCP daily precipitation only has daily data from 1996 to 2009, for the Northern Hemisphere winter (DJF) gives a total of 1173 days. Given that these data sets do not cover a long time range, the long-timescale (> 15 days) correlation may not be reliable. In order to reduce such uncertainty, we used much longer time-period data from our idealized dry model experiments (about 8500~18000 days), CAM runs (9000 days) and IPCC AR4 multi-model runs (1961-2000 DJF consisting of around 3600 days). The results (to be discussed below) showed that the timescale analysis is quite consistent between the different reanalysis data, and has reasonable agreement among different idealized dry model simulations. However for IPCC GCMs, even for different runs of the same model, the timescale of zonal index varies quite a lot. This is probably due to few degrees of freedom in data in addition to the model internal variability.

4.2.4 Regression analysis

Guo (2010) found that the zonal mean precipitation is significantly correlated with the zonal index (jet shift) mode. We also find similar precipitation patterns in reanalysis data (both NCEP/NCAR and ERA40), satellite observations (GPCP), and GCM simulations (CAM 100-year run and IPCC AR4 multi-model runs) as well.

Fig. 4.1 shows the regression of daily zonal wind at 300 hPa and eddy momentum flux against the principal component (PC) of 300-hPa zonal wind first EOF mode in the Southern Hemisphere based on several data sources including NCEP and ERA40 reanalysis, CAM 100-year run results and the control run of our idealized model as well. From this figure, it is very clear that the zonal wind anomalies display a poleward shift pattern (recall that the climatological position of the jet is around 50°S), and the eddy momentum flux anomaly also acts consistently in terms of convergence at the poleward side of the jet, and divergence at the equatorward side of the jet.

To examine whether there exists a robust relationship between the precipitation and jet variability, we regress the PC of the first ERA40 EOF mode of the Southern Hemispheric zonal mean zonal wind at 300-hPa (zonal index) on the daily precipitation anomalies of the GPCP satellite observations (monthly mean), ERA40 and NCEP reanalysis. This precipitation pattern comparison is shown in Fig. 4.2(a). The amplitude based on the two reanalysis datasets is quite similar with each other, while the reanalyses have a much larger magnitude than the satellite observations (GPCP). However the pattern is very consistent among these data sources: enhanced precipitation centered near 60^{o}S and 25^{o}S, and reduced precipitation centered near 45^{o}S. This agreement among three datasets indicates that there exists a robust relationship between the jet shift and precipitation anomalies in observations and reanalysis datasets. Also similar patterns have been found in most of IPCC AR4 models (not shown here).

The time series of eddy momentum flux, which is calculated by projecting the pattern shown in Fig. 4.1(b) onto the original 6-hourly eddy momentum flux fields for both NCEP and ERA40 reanalysis, has been regressed on the precipitation anomalies to get the regression of precipitation associated with eddy momentum flux shown in Fig. 4.2(b). The heating distribution due to this kind of precipitation regression is very similar to what shown in Fig. 4.2(a). In these two figures, the precipitation increases at the poleward side of mid-latitude jet and decreases at the equatorward side, indicating more latent heat released at the north of jet and less at the other side. Thus the effect of latent heat due to precipitation pattern shown in Fig. 4.2 is the same as the effect of eddy heat flux: transporting warm air to the cold side and cold air to the warm side, making the temperature gradient weaker. The climatology (DJF) of daily eddy moisture transport ($v'q'$) and heat flux ($v'T'$) in NCEP reanalysis from 1979 to 2007 is shown in Fig. 4.3, they maximize at almost the same locations in both hemispheres. Their correlation at the latitude where the maximum locates in the SH is about 0.52, and about 0.33 in the NH (both of these correlations are significant at the 95% level based on a two-tailed student's t-test). Therefore, the latent heat of precipitation related with eddy anomalies opposes the eddy momentum forcing which drives the jet poleward. However Fig. 4.2 shows that similar precipitation anomalies are related to both the jet shift and the eddy momentum flux anomalies. The question is whether the precipitation pattern is more directly related to the midlatitude jet shift or the eddy momentum flux anomalies.

To explore this, we calculate three time series by projecting the regression of u300, uv300 and precipitation anomalies, all based on the PC1 of SH u300 (shown in Fig. 4.1(a), Fig. 4.1(b)), and Fig. 4.2(a) respectively), onto their original fields taken from the NCEP reanalysis for the winters of 1979-2001. The autocorrelation of these 3 time series then is computed to represent the timescale of the different anomalies. The same calculation is done for GPCP observations for 1996-2008. The autocorrelation of 300 hPa zonal wind, eddy momentum flux and precipitation based on the Southern Hemispheric zonal index are plotted for both NCEP reanalysis (Fig. 4.4(a)) and GPCP observations (Fig. 4.4(b)). It is obvious that the timescale of precipitation (less than 5 days) is much more closely tied with the eddy momentum flux (less than 5 days) than the zonal wind (about 13-16 days), in both reanalysis data and the GPCP observations. This indicates that the precipitation anomalies related to the Southern Hemispheric zonal index is more closely related to the eddy anomalies instead of the zonal mean flow. Therefore in our discussions below, we will focus more on the relationship between the precipitation pattern and 300 hPa eddy momentum flux anomalies.

4.3 Experiments with extra diabatic heating

Previous research suggested that the timescale of zonal index variations in GCM simulations is somewhat longer than that in reanalysis data, and even longer timescales are found in our idealized dry model simulations. In Fig. 4.5, autocorrelation of the PC1 time series of the Southern Hemispheric zonal index for NCEP reanalysis, CAM model climate experiment, and our idealized dry model control experiment have been compared. The NCEP one can be considered the one close to the real atmosphere, the GCM simulation shows a longer timescale (about 30 days) and our model's control run (without any extra forcing) has an even longer timescale (about 50 days). Although reasons for the timescale gap between reanalysis data and GCMs are still not well known, we can hypothesize that the difference between the GCM and our model control run may be partly due to the lack of moist effect in dry model, and validate this in our modeling studies.

Previous studies have shown that significant positive feedback via changes in the eddy-momentum flux acts to prolong the e-folding timescale of the zonal index, while eddy sensible heat flux acts to damp this mode (Yang and Chang 2007). In this study, we will explore the impacts of diabatic heating associated with the eddies on the timescale of the zonal index. To do that, we will add extra diabatic heating forcing onto our dry model experiments to mimic the effect of moisture. In section 4.2.4, we found a robust relationship between the precipitation and eddies anomalies associated with the zonal index in reanalysis data, observations, as well as in GCM simulations. The extra heating derived from such a precipitation distribution will be imposed in our idealized dry model to study the impact of diabatic heating.

4.3.1 Constant forcing

The first set of experiments we designed in this study is to impose a constant extra forcing at each time step in our idealized model. This constant forcing is a diabatic forcing due to latent heat release of the precipitation distribution we found in previous section (Fig. 4.2(b)). We use the NCEP one to represent a forcing close to the real atmosphere, shown in Fig. 4.6. The extra diabatic forcing is imposed in the Southern Hemisphere, warming in the region of increased precipitation and cooling in the region of decreased rain due to eddy anomalies associated with the zonal index. In the vertical direction, the extra heating is equally distributed in the layer from 850 hPa to 350 hPa, in which the large scale condensation processes mainly occur. The vertically integrated heating corresponds to the precipitation rate shown in Fig. 4.2b.

After imposing the constant extra latent heat due to precipitation associated with the SH zonal index related eddy momentum flux at 300 hPa similar to the real atmosphere, which is warming at poleward side of the mid-latitude jet, cooling at equatorward side and a little warming at subtropics as well, the mid-latitude jet moves equatorward. As shown in Fig. 4.7(a), the green line is the zonal wind difference at 300 hPa between the constant forcing experiment and the control run, and the black line is the zonal wind regression of control run against the NCEP SH zonal index. The zonal wind difference for all levels is shown in Fig. 4.7(b), anomalies peak around layer from 200 hPa to 300 hPa, in which eddy momentum fluxes approach the maximum. Throughout the model atmosphere, from surface to upper level, the zonal wind accelerates at the equator side of the jet and decelerates at the polar side of the jet, making mid-latitude jet shift equatorward.

Given that the latent heat of precipitation we imposed in this study is associated with eddy momentum flux anomalies due to poleward shift of the jet, and after imposing the extra heating the jet moves equatorward, this diabatic forcing clearly acts to oppose the effects of eddy momentum forcing. As we mentioned before, the eddy momentum flux has a positive feedback on mid-latitude jet variations, therefore in this set of experiments we confirmed that the diabatic heating acts to damp the jet shift mode driven by eddy momentum flux, forcing the mid-latitude jet to shift to the opposite direction. Since this heating is related to eddy displacement related to the zonal index, this corresponds to a negative feedback on jet shift mode.

4.3.2 Time varying heating

The constant forcing discussed in the preceding subsection is fixed and time independent, at this point, the first set of experiments suggested that the diabatic forcing has a negative feedback on mid-latitude jet variations, against the effects of eddy momentum forcing. However in the real atmosphere, the diabatic forcing cannot be constant, it must fluctuate in time following the precipitation anomalies related to the eddy anomalies. Therefore in our second set of experiments, the extra heating imposed is time dependent based on the idealized dry model zonal mean momentum flux anomaly at each previous time step.

In this set of experiments, at each time step, heating is imposed based on the pattern shown in Fig. 4.6, but the amplitude of the heating is not constant, but varies depending on the momentum flux anomaly at the previous time step. Specifically, the regressed pattern of zonal mean 300 hPa momentum flux related to the zonal index variation based on the control experiment is used as a reference. This pattern (similar to the pattern shown in Fig. 4.1b) is projected onto the model's 300 hPa zonal mean momentum flux anomaly at the previous time step to obtain an amplitude (that can be either positive or negative). This amplitude is then used to set the amplitude of the diabatic heating anomaly at the current time step. So the derived latent heating associated with such a varying precipitation pattern imposed in the model is varying with time. In this way, the precipitation following the eddy anomalies similar to what happens in the real atmosphere are simulated in the model, instead of a fixed distribution. A set of 6 experiments have been conducted by varying the amplitude of heating imposed (from 0.25 to 4 times the heating shown in Fig. 4.6) to examine the sensitivity of the results to the heating amplitude.

At the end of model run, the results show that the leading mode of zonal wind is not the jet shift mode anymore, which suggest that the north-south jet shifting is suppressed by adding an extra diabatic heating related with eddies, the zonal index was damped as a negative effect of diabatic forcing, exactly as what we expect.

Since the zonal index is no longer the 1st leading mode in model results after imposing extra latent heat, here we project the 1st EOF pattern of ERA40 u300 (which, as discussed above, is the zonal index mode) onto the model simulated zonal mean zonal wind at 300-hPa to get the time series from which the autocorrelation of SH zonal index for model runs is calculated. The model's autocorrelation of the zonal index after imposing latent heat by different magnitudes is plotted in Fig. 4.8. In Fig. 4.8 the black line is the autocorrelation of the control run without extra heating, the other colored lines are results for different magnitudes of diabatic heating imposed in model simulations. Fig. 4.8 shows that the timescale for the extra-heating run is significantly shorter than that of the control run, and it generally gets shorter when larger amplitude of extra heating is applied. While the change in time scale shown in Fig. 4.8 does not seem to be continuous with respect to the heating amplitude, this may be due to the large uncertainty involved in estimating the zonal index time scale due to its relatively long decorrelation time (E. Gerber 2011, personal communications).

4.3.3 Condensational heating due to upward motion

Other than the previous experiments of imposing diabatic heating derived from precipitation associated with eddies, another way to mimic the diabatic heating in a dry model is to parameterize the condensational heating based on model upward motion (e.g. Becker and Schmitz 2001). In this study, the self-induced condensational heating in the extratropics is scaled with the pressure velocity ω and is only active in region of rising motion as indicated by the Heaviside step function $H(-\omega)$ in (4.5), imposed in our dry model. The strength of the heating is derived based on regression between condensational heating and $-\omega$ from a GCM run made with the GFDL R30 spectral model, the spatial structure of this function C(x,y,p) is shown in the Appendix.

$$\frac{D\theta}{Dt} = -\frac{\theta - \theta_E}{\tau} + C(x, y, p)|\omega|H(-\omega) \qquad (4.5)$$

Since in (4.5), the impact of diabatic heating in enhancing baroclinic waves has already been included in the newly added term, in this experiment, there is no need to reduce the static stability of the model atmosphere, and the parameter A in equation (4.3) is set to zero. θ_E is again iterated until the model climate becomes close to the imposed θ_C (with A = 0).

In Fig. 4.9, the autocorrelation for two different runs has been compared in the same way as in previous sections. The green line is the autocorrelation of zonal index variation of a control run without reduction of static stability (A=0 in (4.3)), while the black line is the run forced to same basic state but with parameterized "condensational heating" given by equation (4.5). It is very clear that the timescale of SH zonal index is substantially reduced by adding the condensational heating in the upward motion regions, compared with that of control run without any reduction of static stability. For the model control run, the timescale curve is quite flat without a clear e-folding time, a very low-frequency variation dominates the jet shift. However after adding the condensational heating in rising motion regions, the e-folding time becomes much shorter and is about 17 days. This result suggests that the jet south-north shift mode is significantly damped with parameterized condensational heating in regions of rising motion. It is of interest to note that the second EOF mode (jet strengthening or broadening) and the third EOF mode (the subtropical jet), their timescales are also substantially reduced by adding extra diabatic heating in regions with rising motion (not shown).

In section 4.3.2, we imposed extra latent heating based on eddies associated with the zonal index in our dry model, and find that this forcing works against the effect of eddy momentum forcing which has a positive feedback on jet variations. Therefore, the last experiments indicated that the time varying extra latent heating we imposed related to eddies could damp the zonal index mode, reduce the timescale dramatically. This is the direct impact of diabatic heating on timescale of jet variations. Apart from this direct effect, the experiments discussed in the following paragraph suggest another mechanism behind the relationship of diabatic heating and the zonal index timescale.

In Fig. 4.10, results from 5 different experiments using different values of A (see equation 4.3) ranging from 0 to 2 K/km are shown. In these experiments, no diabatic feedback to the jet variation is imposed. The results show that as the static stability is reduced, the timescale is shortened. The more the static stability is reduced, the more the time scale is shortened. Why is that the case? Our hypothesis is that even though in these experiments, no diabatic feedback is present, but as the static stability decreases, baroclinicity increases, resulting in enhanced eddies. The enhanced eddies then will make the system more chaotic, in this way the zonal index timescale is reduced. When we add the condensational heating in the upward motion regions, since rising motion generally occurs over the warm sector of cyclones, the warm sector of eddies tends to get warmer, resulting in increased eddy energy. Thus the system becomes more chaotic, and the time scale is further reduced in the same way as the zonal index time scale is reduced in the reduced static stability experiments. This effect on the zonal index time scale can be regarded as an indirect effect of diabatic heating. This potentially explains why the parameterized heating experiment discussed in this subsection is more effective in reducing the zonal index timescale than the experiments discussed in the previous subsection (4.3.2), since in the current case, both direct and indirect effects are present, while in the latter case only the direct effect is present while the indirect effect is not.

4.4 Discussions

In this section we would like to briefly summarize the differences in the feedback related to eddy momentum flux, heat flux, and diabatic heating. When the mid-latitude jet shifts poleward, this results in the poleward shift of the baroclinic zone. The wave source shifts with the jet. More waves then propagate equatorward from the wave source at higher latitudes, thus giving rise to more momentum fluxes converging into the new jet position to reinforce the wind anomalies. This is the positive feedback of the eddy momentum flux on zonal wind anomalies. While for the eddy heat flux which always transports heat poleward around the wave source, it mixes the air around cyclones by warming at the north and cooling at the south to weaken the temperature gradient. In this way, it weakens the jet and works against the effect of eddy momentum forcing. Therefore, the heat flux has a negative feedback which is the opposite to the momentum forcing on the zonal wind anomalies. With respect to the effect of diabatic heating investigated in this study, we find the latent heat of precipitation which is related to eddy anomalies due to jet shift has the similar effect as the eddy heat flux. Comparing Fig. 4.1(a) with Fig. 4.2(a), the positive precipitation anomalies due to jet shift is a little poleward of the mid-latitude jet anomalies in the Southern Hemisphere. Thus, there is warming at the poleward side of the positive zonal wind anomalies and cooling at the equatorward side, forcing a weaker temperature gradient to damp this wind anomaly. In fact, there is a high correlation between the heat flux and moisture transport at locations of jet and storm track shown in reanalysis (0.52 in the SH in NCEP mentioned before), which also suggests that eddy moisture feedback should work in a similar manner as feedback due to eddy heat flux, which is to damp the jet shift.

4.5 Conclusion

In this chapter, the role that diabatic heating plays in zonal index variations is investigated using diagnostic and modeling studies.

First, by diagnosing satellite precipitation observations, the reanalysis data, and GCM data, we have found that the precipitation distribution related with the zonal index (basically north-south shift of the jet) in the Southern Hemisphere has a very similar pattern among all the datasets. The precipitation due to poleward shifted (equatorward shifted) mid-latitude jet increases (decreases) at the poleward side of the jet, and decreases (increases) at the equatorward side. Nevertheless, the amplitude of the precipitation anomalies derived from satellite observations is weaker than that based on the two reanalysis data sets.

Since precipitation in the mid-latitudes are due to baroclinic waves, we expect that the precipitation anomalies should be more directly related to anomalies in the eddies instead of the midlatitude jets. So the regression of precipitation based on eddy momentum flux at 300 hPa has been calculated. The results show a similar pattern of precipitation anomaly as that derived based on the jet shift. When we compared the timescales of variations in the midlatitude jet, eddy momentum flux at 300 hPa and precipitation regressed based on the zonal index, we found that the precipitation timescale is closer to the eddy timescale than to the jet timescale. Therefore, we consider the precipitation anomalies to be directly related to anomalies in eddy momentum fluxes.

Meanwhile, we find that the zonal index variability in our dry model experiments displays a very long timescale, which is much longer than those found in GCM runs, which are already longer that that found in the reanalysis data. Although there are still some debates about this timescale difference between reanalysis data and GCM simulations, we hypothesize that the most important reason for this difference between GCMs and our model results could be the lack of moist process in the dry model. This hypothesis is tested by imposing extra diabatic forcing in our dry model in three different ways to mimic the effect of diabatic heating related to the eddy anomalies.

First, time-independent constant diabatic heating is imposed in our idealized dry model. This extra heating is based on the precipitation anomaly regressed from the momentum flux anomaly associated with poleward shift of the jet. When this heating is imposed, the midlatitude jets move equatorward (poleward) when the precipitation is related to poleward (equatorward) shifted eddies. The results suggest that the diabatic forcing has a negative feedback on mid-latitude jet variations, working against the effects of eddy momentum forcing.

Next, a time varying diabatic forcing is added to the model, with the amplitude and sign of the heating imposed based on the modeled eddy momentum flux anomalies at the previous time step. In this experiment, the leading mode of 300 hPa zonal wind is not the jet shift mode anymore, suggesting that this north-south jet shift mode is suppressed by adding the extra latent heat of precipitation related with eddies. Given this point, we can say that the zonal index was damped by a negative feedback of the diabatic forcing. Also the very long timescale in our dry model has been substantially improved in this set of experiments. The timescale of jet shift mode in these experiments with extra-heating is much shorter than that of control run, and it gets shorter when the magnitude of the extra heating is enhanced.

The third way to mimic the effect of diabatic heating is to parametrize diabatic heating as a function of   in regions where there is upward motion. In this experiment, the jet south-north shift mode was again significantly damped. The timescale of SH zonal index becomes much closer to that observed, and is significantly reduced when compared with that of a control run without any reduction in static stability.

Adding the latent heat of precipitation related to eddies could damp the zonal index mode against the eddy momentum forcing to reduce the timescale substantially. This is the direct impact of diabatic heating on zonal index variations. In the experiments with condensational heating imposed in upward motion regions, the warm regions get warmer, which tends to make the eddies stronger. Under such a circumstance, the system will become more chaotic, causing the timescale to be further reduced. In this way, we conclude that diabatic heating can affect the zonal index timescales in two ways.

Appendix 4A: The structure of C(x,y,p) in Equation 4.5

In this appendix, the prescribed spatial distribution of C(x,y,p) shown in Equation (4.5) is described. The strength of the heating imposed in the dry model is derived based on regression between condensational heating and $-\omega$ from a GCM run made with the GFDL R30 spectral model. The structure is qualitatively similar to the function imposed by Becker and Schmitz (2001). The horizontal distribution of the vertical average of C is shown in Fig. 4.11a, while the vertical distribution of the zonal mean of C is shown in Fig. 4.11b. In fact, the values in Fig. 4.11 are $\rho \times g \times C$. It is clear that the heating covers regions from subtropical jet to high latitudes and mainly distributes in the troposphere in both hemispheres, maximizing at the position of the mid-latitude jet stream and subtropical jet around 750 hPa in the Southern Hemisphere, and peaking around 35^{o}N at the same level in the Northern Hemisphere.

To test whether our results are sensitive to the detailed structure of C, we have performed sensitivity studies by broadening the heating function C by 2 grid points (~5.6 degrees latitude) on both the subtropical and poleward sides in both hemispheres and obtained very similar results in terms of reduction in the zonal index timescale. Therefore we conclude that the effects of diabatic feedback in damping the jet shift mode are not very sensitive to the exact form of C imposed.

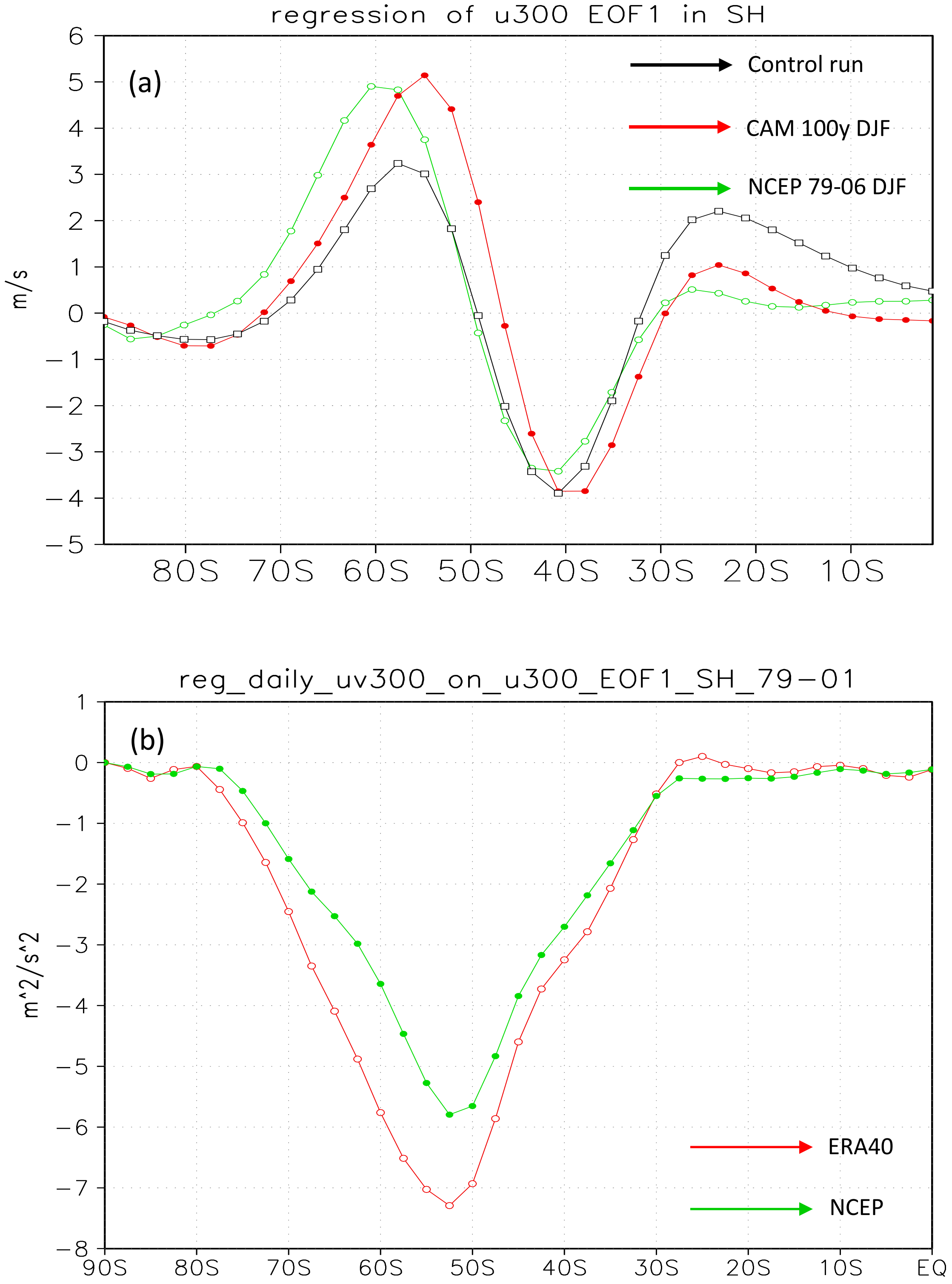

Figure 4.1: Regression based on the PC of EOF1 mode of SH daily u at 300 hPa of: (a) zonal mean daily zonal wind at 300 hPa for control runs of our idealized dry model; CAM 100-year run .DJF; NCEP/NCAR 1979-2006 DJF. Unit: m/s. (b) zonal mean daily momentum flux at 300 hPa on for two data sources: NCEP/NCAR 1979-2001 DJF; ERA40 1979-2001 DJF. Unit: m^2/s^2.

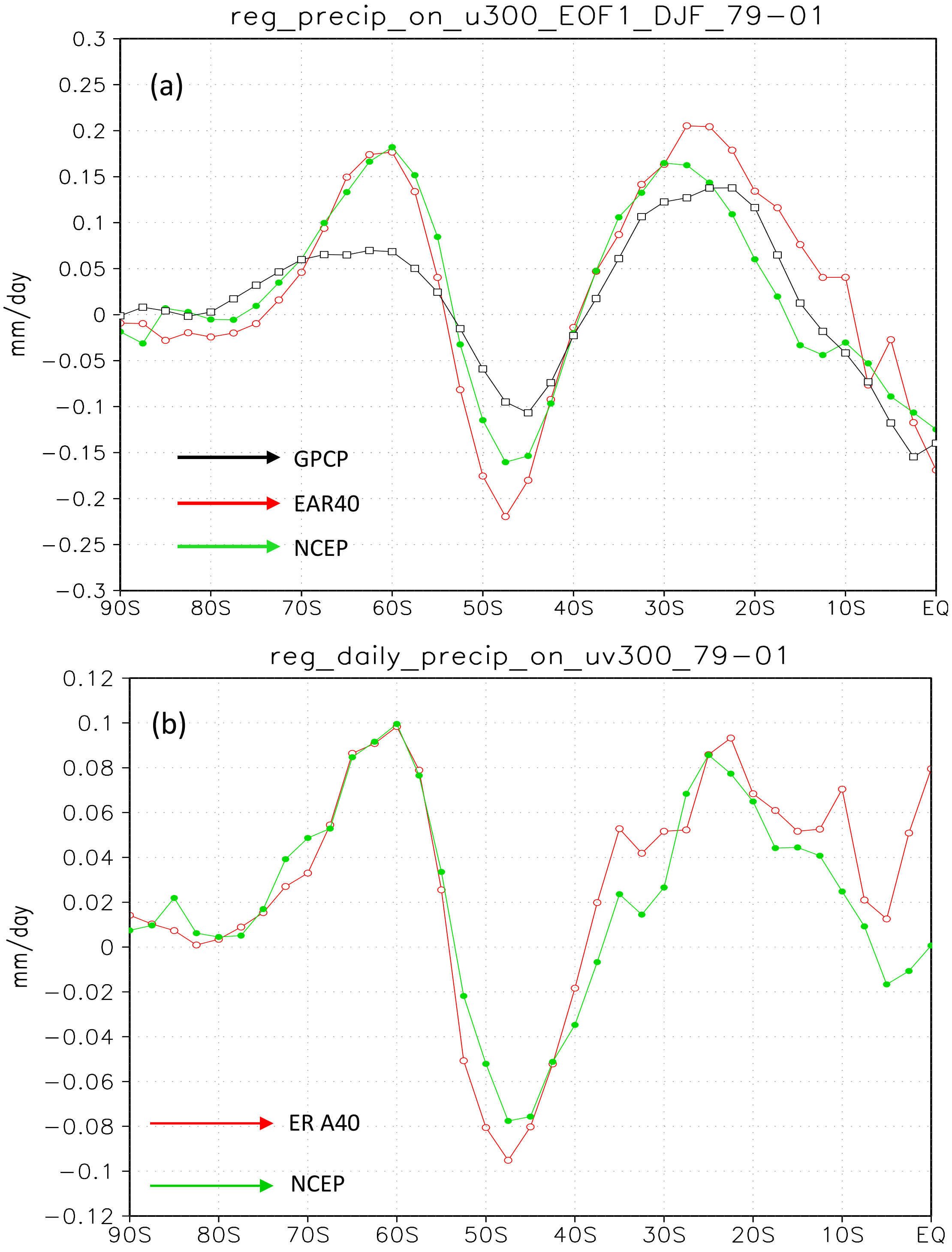

Figure 4.2: Both panels show regression of precipitation from 1979 to 2001 DJF, for: (a) GPCP satellite observations; ECMWF/ERA40; and NCEP/NCAR; based on PC of ERA40 EOF1 mode of u300. (b) NCEP/NCAR; and ECMWF/ERA40; based on time series computed using eddy momentum flux pattern of Fig. 1(b). Unit: mm/day.

a) vt700_daily_mean_79−07

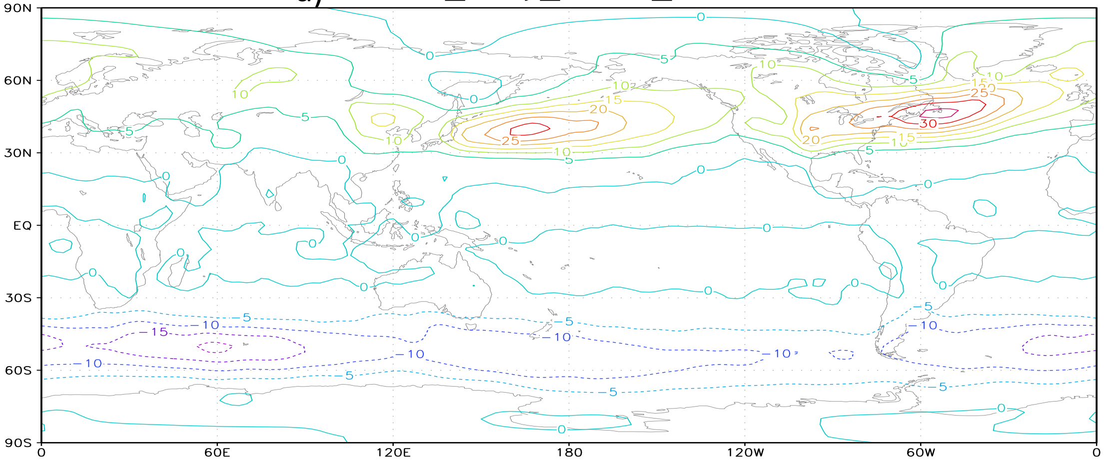

b) vq700_daily_mean_79−07

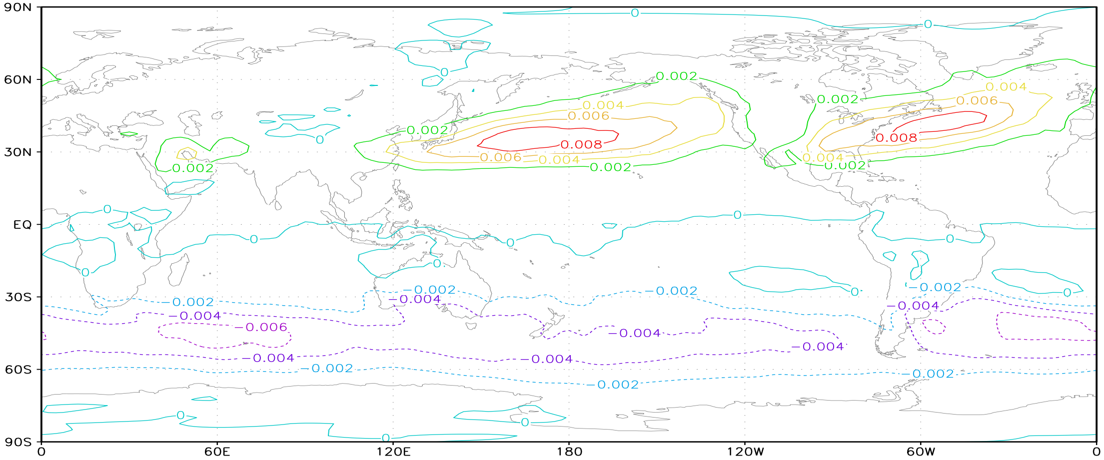

Figure 4.3: The mean of daily (a) eddy heat flux (v’T’). Unit: m·K/s; and (b) eddy moisture transport (v’q’). Unit: m·Kg/s·Kg at 700 hPa in the NCEP reanalysis from 1979 to 2007.

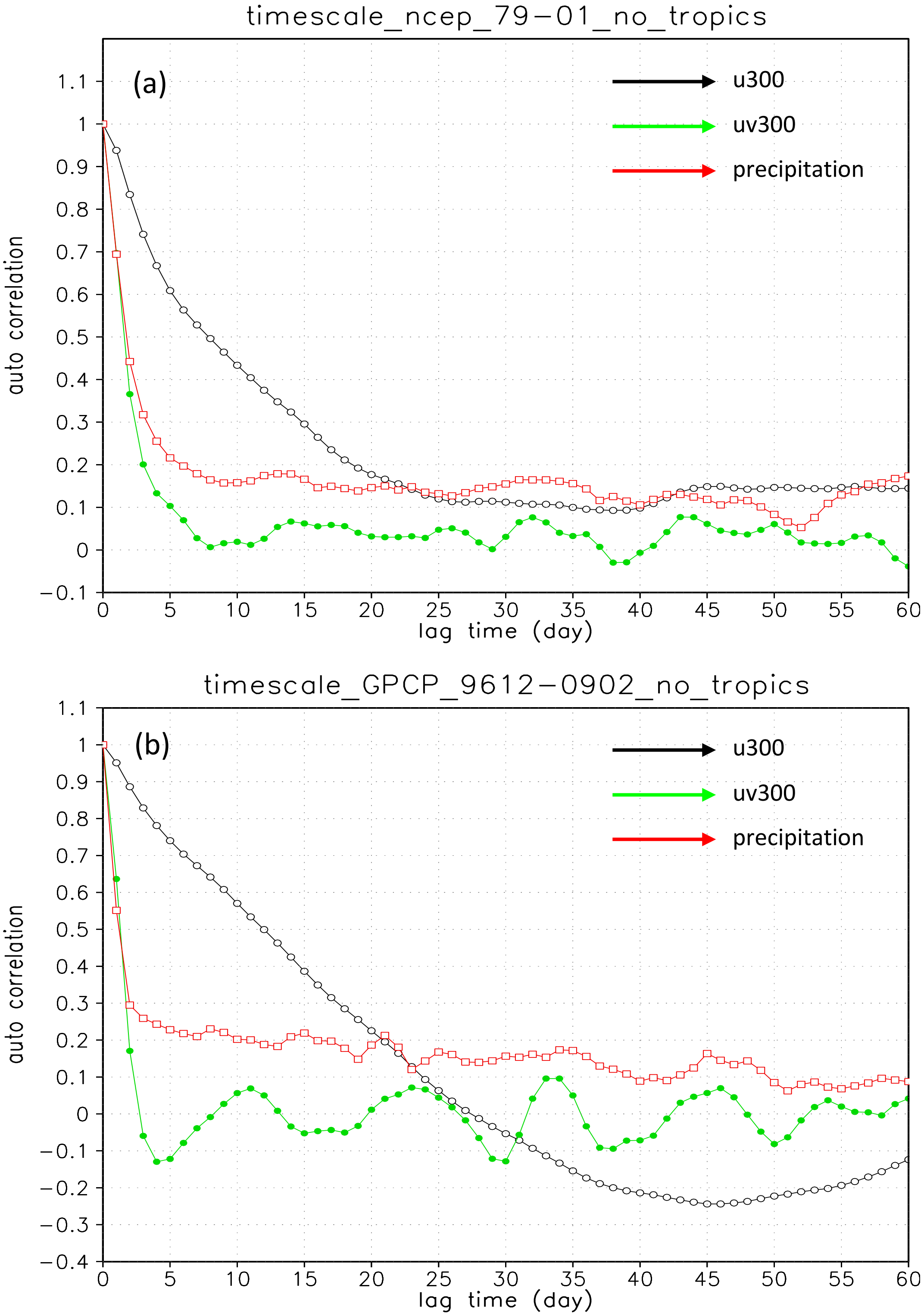

Figure 4.4: Lagged autocorrelation for NCEP 300 hPa zonal wind (black), NCEP eddy momentum flux (green) and precipitation anomalies (red) for (a) NCEP 79-01 DJF and (b) GPCP 96-08 DJF.

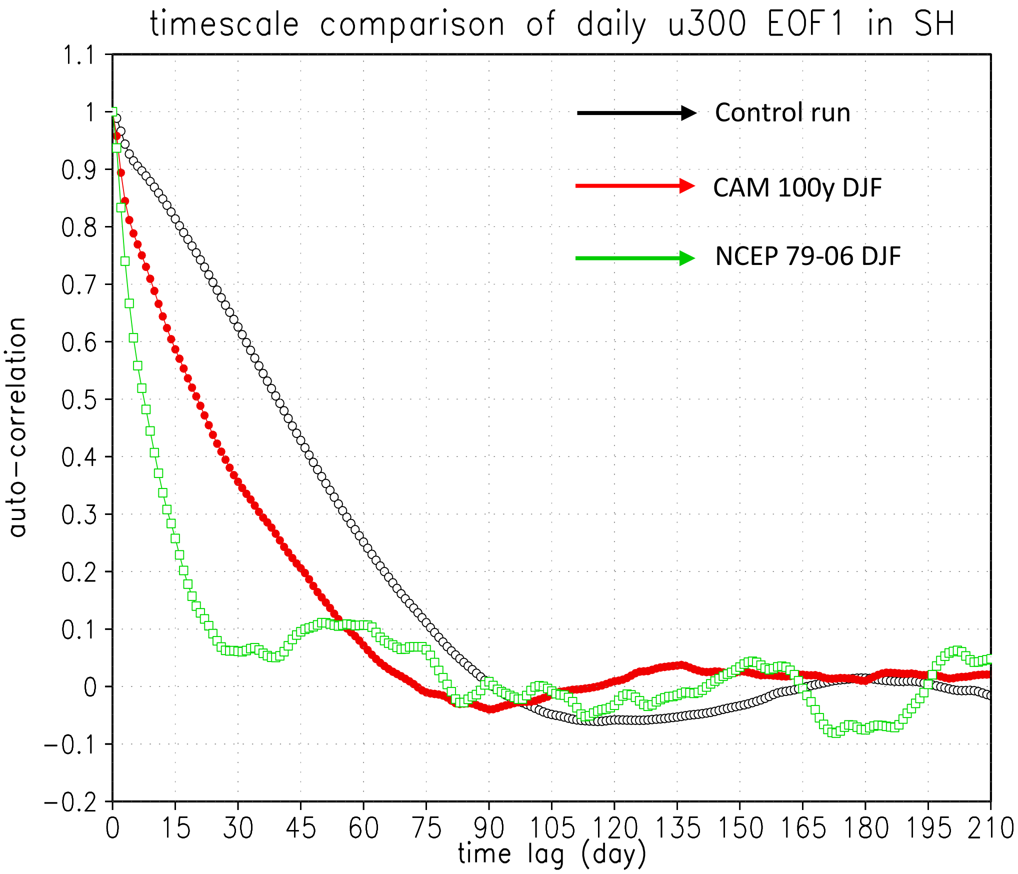

Figure 4.5: Auto-correlation of PC1 for three data sources: NCEP/NCAR 1979-2006 DJF; CAM 100-year runs DJF; control run of our idealized dry model.

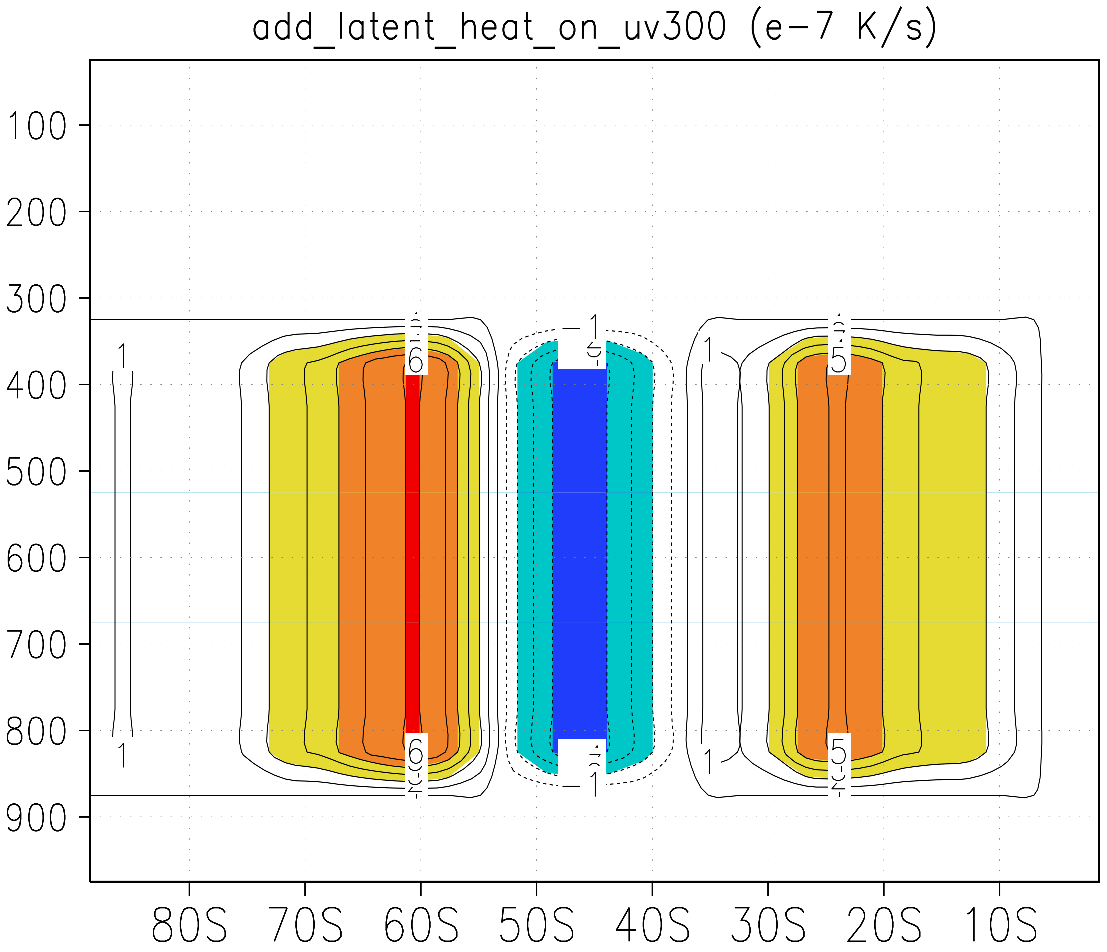

Figure 4.6: The extra heating profile imposed in our idealized dry model experiment at each time step, heating rate computed based on the NCEP precipitation distribution shown in Fig. 4.2b. Unit: 10^{-7} K/s.

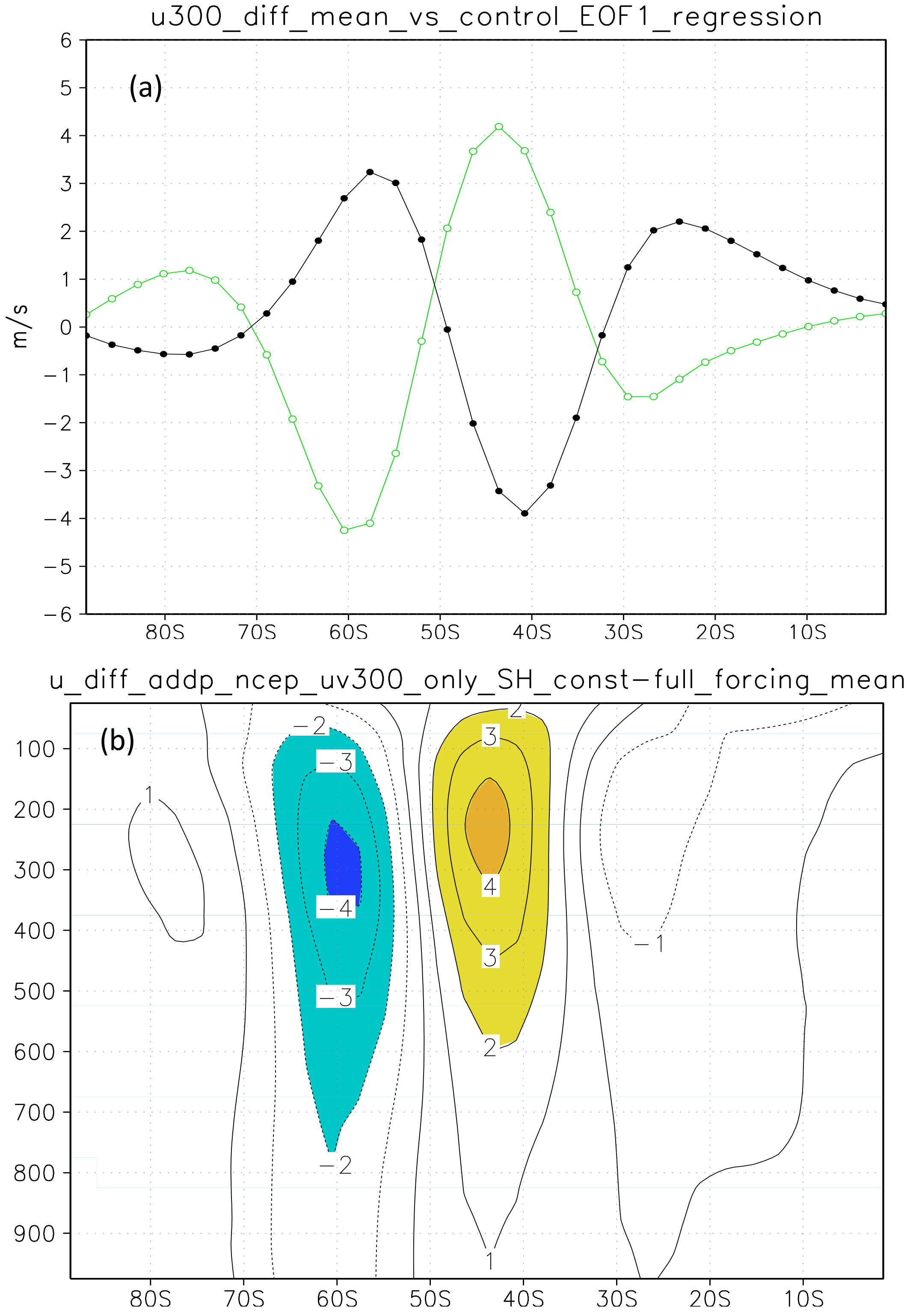

Figure 4.7: (a) Zonal wind difference at 300mb after imposing constant diabatic forcing (green) against u300 EOF1 regression (black) of control run. (b) Zonal wind difference at all levels after imposing constant diabatic forcing. Unit: m/s.

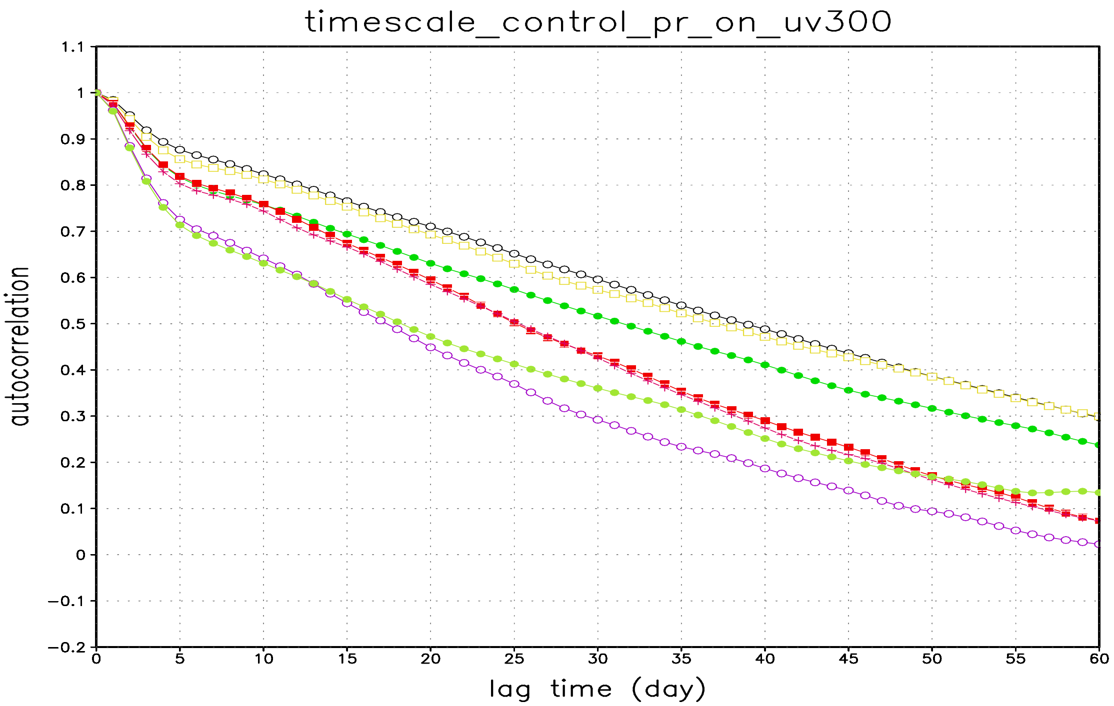

Figure 4.8: Auto correlation of SH zonal index for different runs with different magnitude of extra heating imposed in model.

Black: control (no diabatic heating)

Green: 0.25×heating

Yellow: 0.5×heating

Red: 1×heating (Fig. 4.6)

Dark red: 2×heating

Purple: 3×heating

Light green: 4×heating

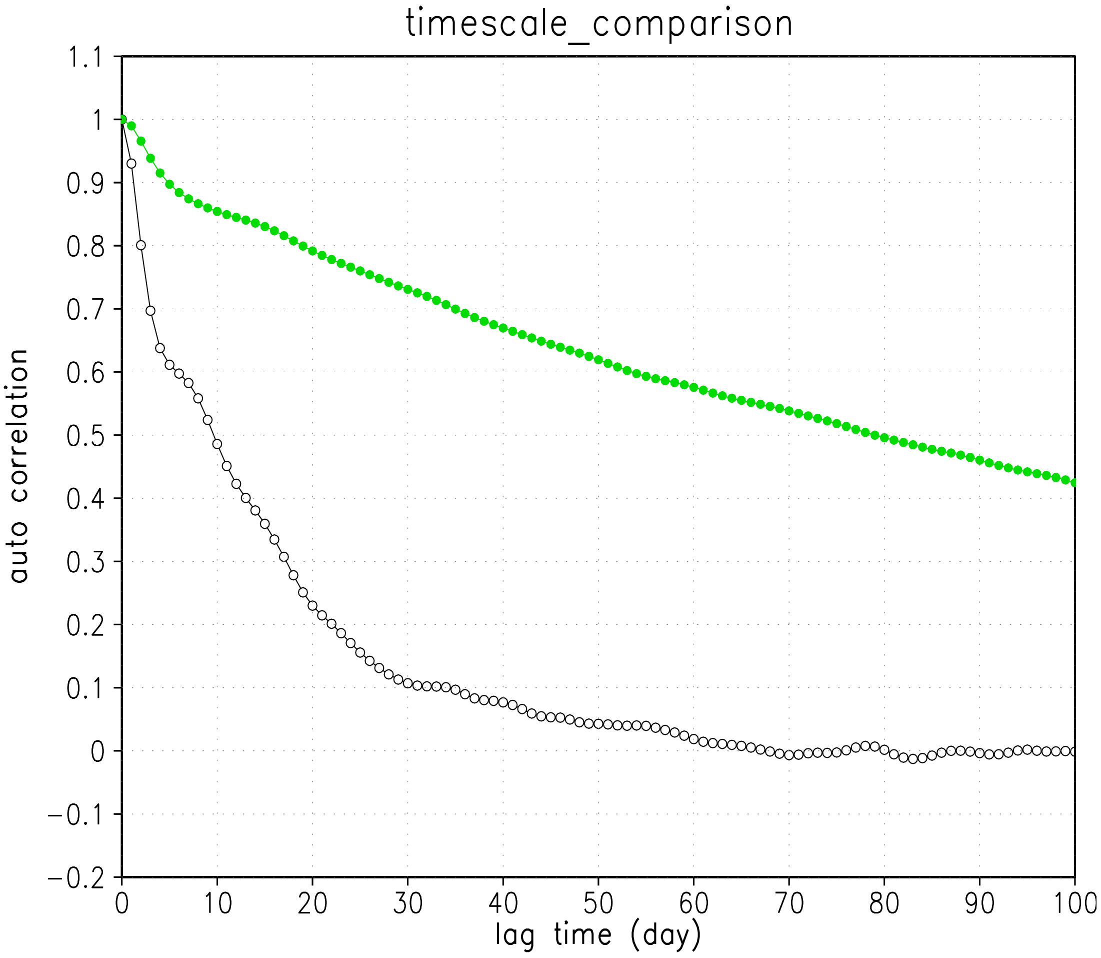

Figure 4.9: Autocorrelation of zonal index variation for:

Green: Control run without reduction of static stability (*A* = 0 in (4.3))

Black: Run forced to same basic state but with parameterized “condensational heating”

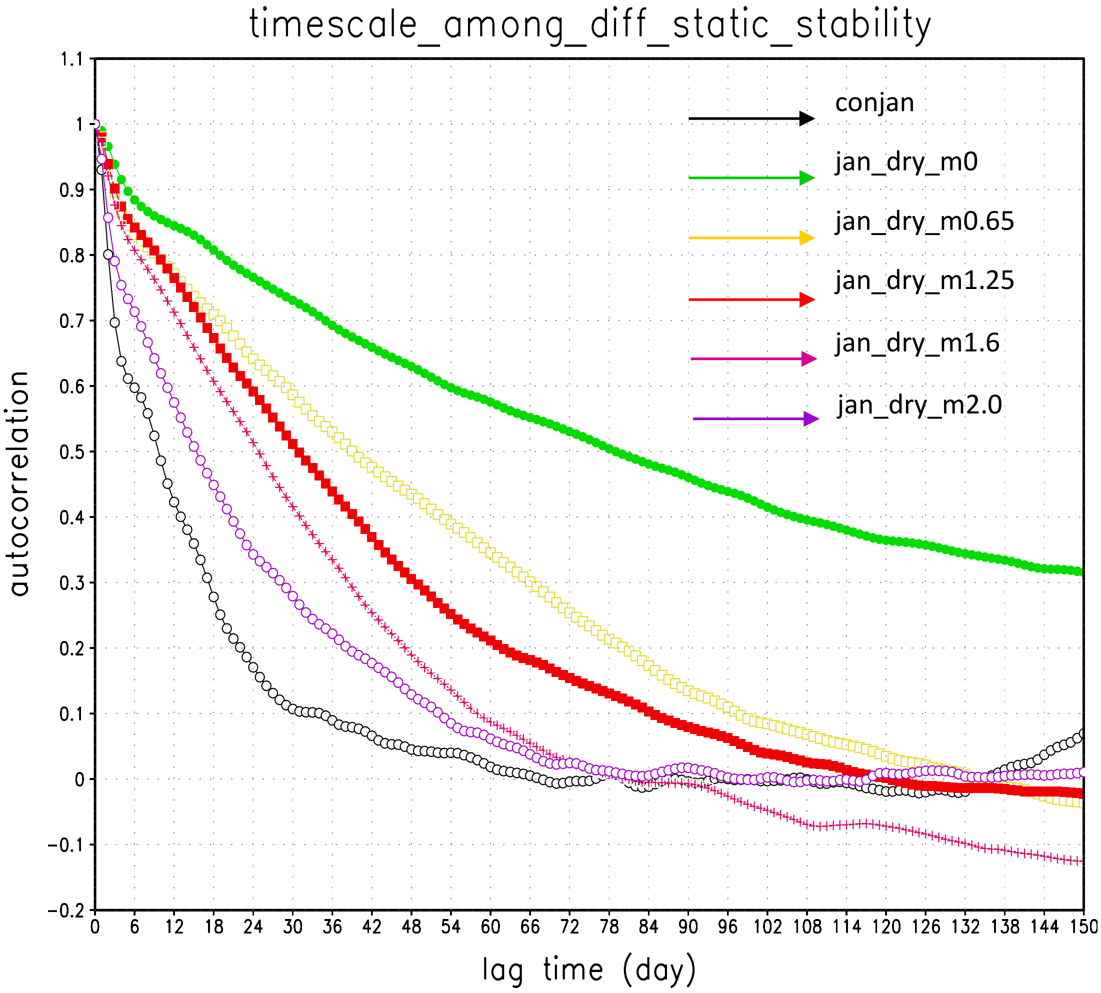

Figure 4.10: Autocorrelation of zonal index variation for:

Green: Control run without reduction of static stability ($A = 0$ in (4.3))

Black: Run forced to same basic state but with parameterized “condensational heating”

Other colors: Control run with different reduction of static stability (A=0.65, 1.25, 1.6, 2.0 respectively)

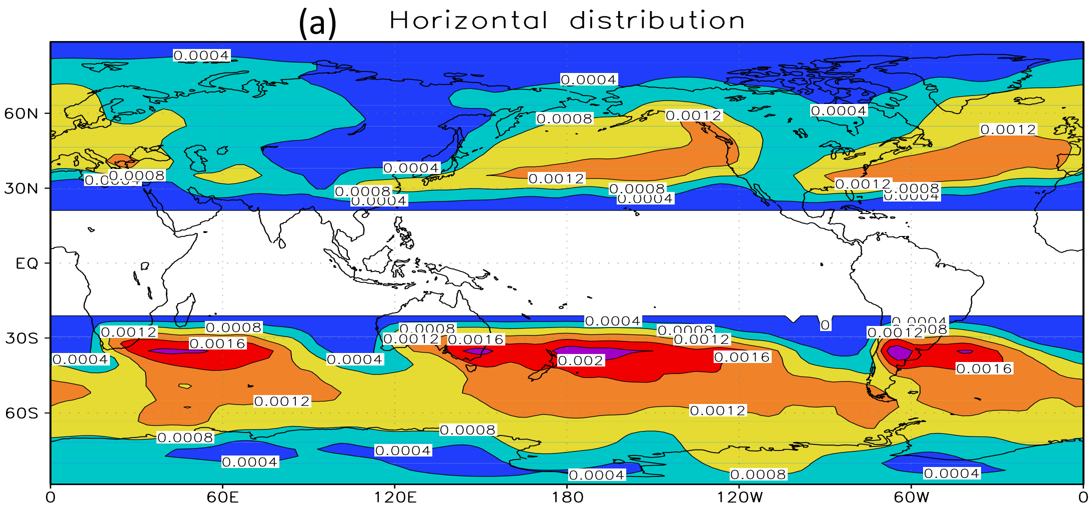
(a) Horizontal distribution

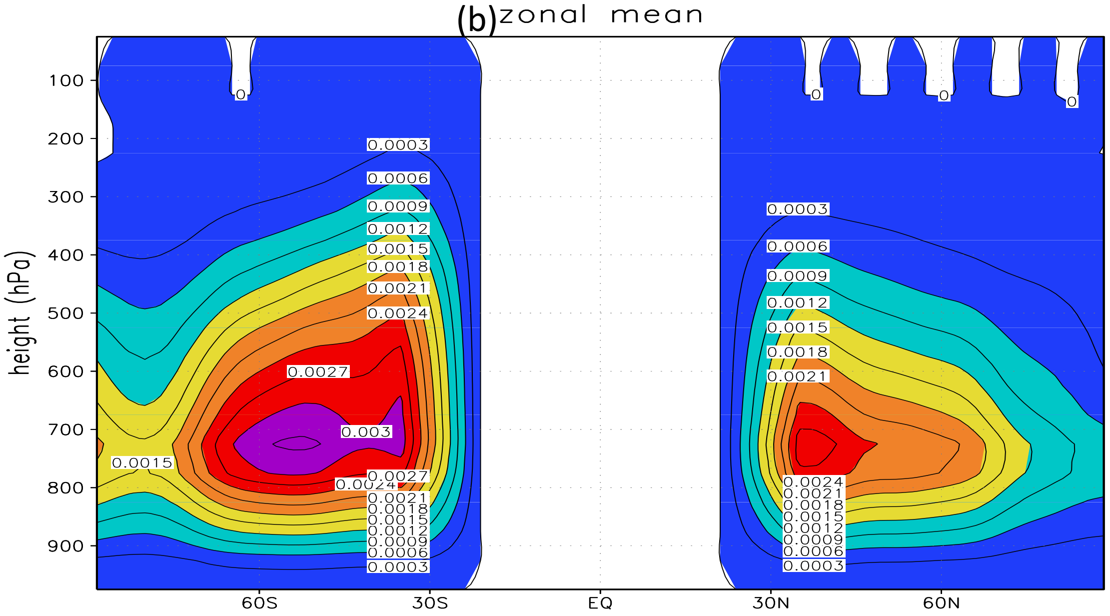
(b)zonal mean

Figure 4.11: The spatial distribution of the structure of ρ·g·C(x,y,p) in which C is in Equation 4.5: (a) Horizontal distribution (vertical average); (b) The latitude-height cross section (zonal mean). Unit: K/m.

Chapter 5 Understanding GCM predicted storm track changes under global warming

As we introduced in previous chapters, the mid-latitude storm tracks, defined as the temporal and spatial variability of the meridional wind, heat fluxes and momentum fluxes and so on, have rather remarkable impacts on the mid-latitude areas in terms of both synoptic and climate aspects. The storm tracks are usually tied closely with the eddy-driven jets, as well as the general circulation since they effect and constrain each other by exchange of energy and momentum. Therefore, once one of them has changed under global warming, say the most direct one the general circulation which was driven by thermal cause, how will the others change? Under what mechanism?

Following up on some hypotheses raised recently, in this chapter we will examine the influence of static stability, temperature gradient and tropopause height change by using an idealized storm track model with realistic climate and forcings in this study.

5.1 Introduction (Motivation)

In recent years, how the extratropical climate and Hadley cell respond to global warming has gained increasing attention. Under global warming, Yin (2005) found a poleward shift of mid-latitude storm tracks in multi-model outputs of IPCC AR4 experiments. Meanwhile, a poleward shift in eddy-driven jets has been discovered in a GCM experiment by Kushner et al. (2001), which is also found in reanalysis data (Fyfe 2003, Chen and Held 2007). Fu et al. (2006) discovered a poleward expansion of the HC over the past 27 years in satellite observations, while Lu et al (2008) found a poleward extension of the poleward edge of the HC responding to the greenhouse gases warming in IPCC AR4 project.

What is the real mechanism behind such a poleward shift of mid-latitude jets or storm tracks and poleward extension of Hadley circulation? There is no consensus explanation so far, but several hypotheses have been raised. In this chapter we will describe several hypotheses and examine them quantitatively.

First, let us examine the projected temperature change which is likely to be mostly due to the direct consequence of increased greenhouse gases including carbon dioxide and water vapor. In Fig. 5.1, zonal mean temperature change simulated in greenhouse gas emission scenarios (A1B and A2) by IPCC AR4 models without ozone recovery (see discussions below) between the last 20-year of the 20th and 21st century is plotted as the anomalies due to global warming. A big warming center is located over the tropics just underneath the tropopause, with maximum in the upper troposphere because the moist adiabatic structure (decreased moist adiabatic lapse rate by latent heat releasing as moist parcels ascend) results in upper tropospheric amplification of global warming within the tropics. All the troposphere is warmed up by the greenhouse effect, with greatest warming over the polar region near the surface in the Northern Hemisphere. This is because high latitudes warm more than the lower latitudes due to the positive feedback of sea ice and snow cover under global warming. In contrast, this feedback is very weak in the circumpolar ocean regions of the Southern Hemisphere because of the vertical mixing of heat over a deep water column (Manabe et al. 1991, 1992; Manabe 1998). Meanwhile, given the increased longwave emission by increased CO_2 the stratosphere is projected to cool down.

One hypothesis for the poleward shift of the jet or extension of the poleward edge of the Hadley cell is that it is a response to the increased static stability under global warming. Lu et al. (2008) argued that with the static stability projected to increase over subtropics due to global warming (see Fig. 1a), baroclinic instability will be suppressed at the equatorward side of the midlatitude jet, leading to the jet to shift poleward, or the Hadley circulation to expand poleward. Held (2000) suggested that the meridional extent of the Hadley cell could depend on the gross static stability, which is inversely proportional to the critical criterion for baroclinic instability, providing an alternative view different from the classic inviscid theory for axisymmetric circulations (Held and Hou, 1980) which suggested that the HC meridional scales had no explicit dependence on the static stability. Frierson et al. (2006), based on experiments using simplified dry and moist general circulation models, argued that the meridional extent of the Hadley cell was sensitive to tropospheric static stability., In their experiments, they found a much stronger and poleward extended Hadley cell in the dry case, while in the moist case the Hadley cell was weaker and the Ferrel cell was also much weaker and displaced poleward. They argued that with increasing moisture the meridional temperature gradient decreased and the static stability increased, both effects lead to a flattening of the dry isentropic slope which was related to the reduction in eddy kinetic energy (EKE). And they explained the poleward shift in their model in terms of the preferential stabilization of baroclinic eddies at low latitudes. Meanwhile Lu et al. (2008) found a weakening and increased poleward extent of the HC together with increased static stability under global warming in the

IPCC AR4 greenhouse gases (GHG) emission scenarios data. Based on the same dataset Yin (2005) found enhanced EKE at the poleward side of the jet. The different extent of the Hadley circulation and the opposite change of the EKE in the different dataset and model studies are of particular interest.

Geng and Sugi (2003) suggested that the baroclinicity will be decreased in both hemispheres due to global warming, and argued that the reasons for the decreased baroclinicity were different for each hemisphere. In the Northern Hemisphere mid-latitudes, the decrease of baroclinicity was mainly caused by the decrease of meridional temperature gradient, while in the Southern Hemisphere, such a decrease was caused by the static stability increase due to the enhanced greenhouse gases. Yin (2005) also pointed out that the effect of the meridional temperature gradient on baroclinicity was clearly larger than the static stability on the maximum Eady growth rate, it was primarily responsible for the poleward shift of baroclinicity in the Northern Hemisphere except in boreal summer. Therefore the distinction between two hemispheres, even in different seasons, is worth further studies. Since dynamical processes are more complex in the Northern Hemisphere, in this chapter we will first focus on the Southern Hemisphere which could give us a basic and relatively simpler view of the dynamics involved.

Another hypothesis relates to the rise of the tropopause height. Held and Hou (1980) developed a theory in which the poleward flow in the Hadley cell was nearly angular momentum conserving as the fluid is sufficiently inviscid. This theory predicted that the width of the Hadley cell should be proportional to the square root of the tropopause height. On the other hand, William (2006), based on idealized numerical experiments, suggested that change of eddy scales due to changes in tropopause height, was responsible for changes in the HC extent and jet shift, and the tropopause change also played a role in determining the jet characteristic, single jet or double-jet, and even multi-jet. In a simple dry GCM, he uniformly increased the stratospheric temperature to lower the tropopause height and found smaller eddies and equatorward shift of single jet due to lowering of tropopause height. These studies exhibited a particularly tight relationship between the tropopause height and the HC extent or jet latitude.

Haigh et al (2005) conducted a series of experiments by increasing temperature in the lower stratosphere (just above the tropopause) either uniformly, as a function of latitude, or only at polar latitudes, respectively, using a simple GCM, in an attempt to find out how the troposphere responses dynamically to changes in heating in the lower stratosphere. They found an equatorward shift of tropospheric midlatitude jet in the cases of latitudinally uniform or high-latitude heating in the stratosphere, poleward shift responding to low-latitude heating at stratosphere, and weakened jets in all the cases. In these experiments, not much attention was paid to the role of the tropopause on jet position – the authors, only claimed that the lowering tropopause associated with imposed stratospheric warming tends to weaken the jet and storm tracks, whereas the shift of jets depends on the latitudinal distribution of stratospheric heating, it is primarily determined by the changes in the poleward eddy momentum flux due to the temperature changes in the lower stratosphere. These results suggested that the meridional temperature gradient seems to be a correct way to think about the zonal wind response. However, Lorenz and DeWeaver (2007) suggested that jet shift due to global warming was predominantly driven by a rise in the height of the tropopause, especially in the midlatitude regions. They imposed a 400m rise in the tropopause height in their simiple GCM run, and showed that the lapse rate change as a result of this tropopause rise is similar to that found in IPCC model results for global warming. As the tropopause height increase resulted in poleward shift of the mid-latitude jets in their idealized experiments that is comparable to that found in global warming experiments, the authors concluded that other factors such as increased moisture content and the change in the low-level pole-to-equator temperature gradient, likely only played a secondary role. They also tried to separate the effects of tropopause height rise and meridional temperature gradient changes near the tropopause by putting the heat source above or below the tropopause, also varying with latitude. In this way, they claimed that the tropopause height determined the zonal wind response, especially in the mid-latitudes.

A third hypothesis suggests that poleward shift of the jet may be related to change in eddy phase speed. While the troposphere is warming, the stratosphere is getting cooler due to increased CO_2 since the dominant balance in the stratosphere is between warming due to shortwave absorption by ozone and cooling due to longwave emission by CO_2 (e.g., Held 1993), and with the simultaneous warming in the upper troposphere, the jet in the lower stratosphere will be enhanced because of the increased meridional temperature gradient near the tropopause. Chen and Held (2007) found that the increased zonal winds near the tropopause or in the lower stratosphere increased the eastward phase speeds of midlatitude eddies, leading to a poleward shift of the eddy momentum flux convergence and the associated surface and tropospheric winds.

On the other hand, ozone recovery could also play an important role in changing the stratospheric temperature profile, by offsetting or even overwhelming the stratospheric cooling. Based on results obtained from chemical-climate models with a fully interactive stratospheric chemistry, Son and his colleague (Son et al., 2008) discovered that the effect of the ozone recovery, which will warm the polar stratosphere due to solar UV radiation absorbed by ozone, might overwhelm the effect of the stratospheric cooling due to the increasing greenhouse gases. Therefore, we have separated the IPCC AR4 multiple-model runs into two groups which will be introduced below when we describe the data used. In order to simplify the problem, we will focus on the simulations without ozone recovery in this work. In addition, most IPCC AR4 models as well as our idealized model have rather coarse vertical resolution and do not resolve the stratospheric circulation. The influence of the changes in the stratosphere on the midlatitude jet or storm tracks under global warming will be an interesting topic to pursue in the future.

More recently, Lim and Simmonds (2008) focus only on the Southern Hemisphere storm track response to tropical tropospheric heating in idealized experiments of a GCM. Simpson et al. (2009) focus on the thermal effects of the solar cycle in the tropical stratosphere by using a simple GCM. Butler et al. (2010) examine the steady-state extratropical atmospheric response to three pieces thermal forcing of anthropogenic climate change individually in a simple GCM. In their experiments, several idealized thermal forcings in terms of different location or depth are imposed in this dry core model to mimic three aspects of anthropogenic climate change: warming in the tropical troposphere, cooling in the polar stratosphere, and warming at the polar surface. They suggest that the first two forcings drive the storm track shift poleward while the third one drives an equatorward shift.

Results presented in the preceding paragraphs are mostly based on model experiments that apply thermal forcing in a very idealized context, usually with the model climate forced to a zonally symmetric idealized temperature profile that is constructed analytically to bear some resemblance to the earth's atmosphere. However, several recent studies suggested that the response of a model atmosphere to thermal forcing may be very sensitive to the timescale of the model climate system (Bell 1980; Ring and Plumb 2007, 2008; Gerber et al. 2008; Chan and Plumb 2009). Leith (1975) first suggested that the climate response to changes in external forcing of the climate system could be estimated via the fluctuation-dissipation theorem (FDT). Afterwards, plenty of relevant studies as above have been done. In general, we can write the fluctuation-dissipation theorem applied in climate system as follows:

$$\frac{dX}{dt} = -\frac{X}{\tau} + C + \xi(t) \tag{5.1}$$

where X stands for the climate response which is the response of jet shift mode in this study, and τ is the timescale of this mode. The last two terms on the right side of the equation are the total forcing including the constant external thermal forcing and the random eddy forcing. When it is time averaged at equilibrium, the time derivative of the climate response and the random eddy forcing vanish, thus equation (5.1) becomes:

$$X = \tau C \tag{5.2}$$

Based on (5.2,) the climate response of this mode is seen to be proportional to the timescale of this mode. As we found in Chapter 4, the timescale of the zonal index variability is much longer in a dry model run due to lack of the moist feedback which acts to damp the zonal index mode. Therefore, with the same constant external forcing, the jet response can be much stronger due to its proportional relationship with the longer timescale in dry model runs than the simulations with diabatic feedback. This is also the difference we expect between the dry model runs and experiments of imposing extra diabatic heating which we will discuss later.

In our study, we will make use of a model with a mean climate similar to that found in reanalysis data (see Chang 2006). We will make use of the global warming forcing calculated from the IPCC AR4 prediction shown in Fig. 5.1 in our modeling work. The global warming forcing will be separated into several pieces such as the static stability forcing, the temperature gradient forcing and the tropopause height rise and so on, and the importance of each one to the jet response will be examined. As discussed in Ch. 4, the jet shift mode in the control dry model experiment has a very long auto-correlation time scale, and by incorporating the diabatic feedback discussed there, the timescale was found to be substantially decreased. Hence experiments incorporating extra diabatic heating such as the latent heat of precipitation related to eddies and the parameterized condensational heating will be imposed in the dry model to examine if the response is different from that found in the dry model runs. For both dry model runs and experiments with additional diabatic feedback, the constant thermal forcing (i.e. the target temperature profile) imposed in the model is the same, while the jet responses are expected to be different. This is because while the baroclinic component will obviously be constrained by the thermal wind balance and exhibit similar changes, the barotropic component is not constrained by the imposed heating, and much of the wind response is likely from this aspect. Therefore, we will focus mainly on what drives the change in the barotropic component of the jet.

5.2 Data and method

In this study, numerical experiments are conducted based on the idealized storm track model introduced in section 2.4. However in order to investigate the global warming scenarios, the target temperature profile (θ_C in equation (2.1) and (2,2)) is changed from the climatological temperature distribution derived from reanalysis data to one with anomalies of IPCC AR4 models ensemble mean (see Fig. 1) added on.

The datasets used in this work include the NCEP/NCAR reanalysis and ECMWF ERA-40 reanalysis just the same as described in previous chapters, and the last 20 years of the 20th century simulations as well as last 20 years of the 21st century CO_2 emission scenarios runs of IPCC AR4 models. In order to increase the sample size for the scaling/sensitivity analysis, the 21st century products we used here include the A2 scenario, a high-emission scenario (CO_2 concentration reaches 800 ppm at the end of the 21st century), and a scenario with less aggressive global house gas forcing A1B, with CO_2 stabilized at 720 ppm. Both daily data and monthly mean data have been examined. All the model data that we examine are listed in Table 5.1.

As we mentioned before, we separated the IPCC AR4 multi-model runs into two groups, the ones without ozone recovery including BCCR_BCM2_0 (British), CCCMA_CGCM3_1_t47, CCCMA_CGCM3_1_t63, GISS_AOM, GISS_E_R, IAP_FGOALS1_0_G, INMCM3.0, IPSL_CM4, MRI_CGCM2.3.2A, while the others are with ozone recovery, including CNRM_CM3, CSIRO_MK, GFDL_CM2.0, GFDL_CM2.1, MIROC3_2_MEDRES, MPI_ECHAM5, NCAR_CCSM, NCAR_PCM, UKMO_HADCM3, UKMO_HADGEM1. We'll focus on the case without ozone recovery.

The temperature anomalies of global warming projected by the IPCC AR4 future runs used in this study (and shown in Fig. 5.1a) are the differences between the mean temperature of the last 20-year in the 21st century and the last 20-year mean of the 20th century climate runs for each model without ozone recovery. This 3-D temperature anomaly is then added onto the NCEP climatology to get the target temperature profile. We will treat this as the "target temperature profile of the global warming runs" and impose it into storm track model to run the following experiments.

One may argue that the temperature anomalies projected by the IPCC runs may not be due to heating alone, but may also reflect the impact of the circulation response to the actual heating. However, results shown below show that the temperature response to the heating strongly resembles the applied heating, suggesting that much of the temperature response is likely due to the direct effect of diabatic heating. Moreover, previous studies (e.g. Butler et al. 2010) have suggested that the jet shift response is not very sensitive to small details in the applied heating distributions, thus we believe that using the temperature anomalies projected by IPCC models as the forcing is sufficient for our purpose.

5.3 Experiments

In our global warming experiments, the most substantial difference from previous studies is that in this study, more realistic climate and forcings (based on NCEP/NCAR reanalysis climatology and IPCC models projected temperature change), rather than idealized ones used in previous studies, have been applied. Because the jet response is more robust in the Southern Hemisphere, and because of the zonal symmetry in the Southern Hemisphere, which leads to simpler dynamical processes, in this study we will mainly examine the Southern Hemispheric anomalies.

Based on the hypotheses discussed in section 5.1, we have designed several experiments to examine the influence of the static stability, temperature gradient and tropopause height anomalies associated with global warming on the mid-latitude jets shift. In the previous chapter, we have discovered that the extra diabatic heating imposed in the dry model could substantially reduce the timescale of zonal index variations. Thus in this chapter, we will add the same diabatic forcing as the ones used in chapter 4 in these global warming experiments to check if it would also shorten the timescale of jet shifting mode just as what it did in control experiments, and modify the response to the thermal forcing.

The climate run (also called control run in previous chapter) is the one with the NCEP/NCAR reanalysis climatology as the target temperature profile, and without any extra forcing except the diabatic Q, just as the same as the control run in previous chapters. Based on this climate run, different forcings have been added such as the static stability change globally or locally, only the temperature gradient change, all the temperature anomalies due to global warming, and the tropopause rise and so on.

As we mentioned in section 5.2, the temperature anomalies due to global warming scenarios (here we used A1B, A2) in IPCC AR4 simulations have been calculated as the difference between the last 20-year mean of the 20th and 21st century. This temperature anomaly due to global warming scenarios is shown in Fig. 5.1(a). As we introduce in the first part, there is a big warming center with a maximum of 5 degrees over the tropics just under the tropopause and cooling all through the stratosphere. Meanwhile over the north pole near the surface, there exists a very strong warming center with maximum warming of over 8 degrees. Therefore several important factors of the atmosphere would have been impacted by such a thermal forcing due to global warming. The static stability, the temperature gradient, and the tropopause height anomalies are the main three aspects we will investigate.

The zonal mean zonal wind anomalies as the difference between 21st and 20th century simulated in IPCC AR4 models are plotted in Fig. 5.1(b). There is a dipole over the Southern Hemispheric mid-latitude jet, the zonal wind increased at the poleward side of the jet, and decreased at the equatorward side, resulting in a poleward shift of the mid-latitude jet. The anomalies mainly peak in the upper troposphere and lower stratosphere, and their structure is quite barotropic in the troposphere. In the Northern Hemisphere, the enhanced zonal wind anomalies are mainly over the subtropics near the tropopause, while there is no an apparent dipole structure as exhibited in the Southern Hemisphere. It seemed that the mid-latitude jet in the NH didn't change much in the IPCC AR4 global warming projections by these models. As some studies suggested (Geng and Sugi 2003; Yin 2005; Deser et al. 2010), the decreased temperature gradient near the surface could offset some effects caused by upper level enhanced temperature gradient.

5.3.1 Experiments using the dry model

In this subsection, we will first discuss results from the control version of the dry model without extra diabatic heating feedback imposed.

i. Total forcing versus static stability change at each level

When we impose the entire temperature anomalies as shown in Fig. 5.1(a) in the dry model, it is called the "total forcing" experiment hereafter. The total thermal forcing certainly includes all the forcings on mid-latitude jets and storm tracks variations, such as the changes of static stability and temperature gradient, and the tropopause height rise. The zonal mean temperature response is shown in Fig. 5.2(a). We see that the response is quite similar to the imposed forcing (Fig. 5.1a), supporting our argument above that much of the temperature change represents a response to diabatic heating. In Fig. 5.2(b), the latitude-height distribution of the zonal mean zonal wind anomalies for the total forcing experiments is plotted. The response is much stronger than that simulated by the IPCC

AR4 GCMs, shown in Fig. 5.1(b), in terms of either poleward shift or the strengthening of the jet in both hemispheres. The main key is that in our dry model runs, there is no moist effect, while in GCMs there is. As discussed above, if there is no moist process in the model, there is no negative diabatic feedback, but the positive dynamical feedback associated with the eddy momentum fluxes is present. In that case, the zonal index (or jet shift) variations will have much longer time scale, and based on the discussions above, we expect the response related to the jet shift mode will be significantly enhanced. Nevertheless, this experiment demonstrate that when the total forcing is applied, the Southern Hemisphere jet responses by shifting poleward. In the discussions below, we will separate this forcing into different pieces and examine the response to each of the difference pieces of forcing.

To examine the impact of change in global static stability, we compute the global mean temperature change at each level, then add it onto the climatology to become the new target temperature profile that includes global mean static stability increase in the troposphere. This forcing is referred to the “global static stability forcing” in the dry model. When we subtract the global static stability forcing from the total forcing, the resultant forcing is called the “temperature gradient only forcing” in the following studies.

The same zonal wind response except driven by the global static stability forcing is plotted in Fig. 5.2(d) and the one driven by the temperature gradient only forcing, which was the rest when subtracting the global mean static stability forcing from the total forcing, is plotted in Fig. 5.2(c) as well. From these figures, we can see that it was very clear that there were almost no significant zonal wind anomalies responding to the global static stability forcing. While the zonal wind response in experiment of the total forcing and of the temperature gradient only forcing was almost the same, not only in terms of the latitude position or the height peaks, but also in terms of the maximum of anomalies.

Comparing Fig. 5.2(b) to Fig. 5.2(c), they are almost identical. The zonal mean zonal wind exhibited positive anomalies at the poleward side of mid-latitude jets and negative anomalies at the equatorward side in the Southern and Northern hemispheres for both experiments of imposing different forcings. Both wind anomalies were quite barotropic distributed through height from surface to the tropopause. These results are consistent with the results of previous work which suggest that the mid-latitude jet will shift toward polar region under heating mimicking global warming. However in our studies, although so far we cannot completely separate the temperature gradient change from the static stability change, given that the total forcing is the sum of the other forcings, the similarity of Fig. 5.2(b) and (c), as well as the near zero zonal wind response in Fig. 5.2(d) indicated that the static stability, at least the globally uniformly changed static stability, was not that crucial to the mid-latitude jet poleward shift under global warming, while the impact of change in temperature gradient is much more important.

ii. Meridional temperature gradient only

a. Upper level vs. lower level

The results from the previous subsection show that the horizontal temperature gradient was very important to poleward shifting of the jets under global warming. Therefore, in this part we are going to explore the temperature gradient only forcing in more details. In IPCC AR4 multi-model's global warming scenario simulations, we found that near the tropopause, a very significant enhanced temperature gradient structure had been established for both hemispheres when the greenhouse gases increased, this strong anomaly extended from the upper troposphere to lower stratosphere. In the Northern Hemisphere near the surface, the temperature gradient was substantially reduced due to the warming in the northern pole. These are all shown in Fig. 5.1(a). So did the surface temperature gradient change due to global warming play a big role in making mid-latitude jet poleward shift?

Geng and Sugi (2003) found the change in extratropical cyclone activity to enhanced greenhouse gases was closely linked to the changes in the baroclinicity in the lower troposphere in an AGCM. Held and O'Brien (1992) suggested that the baroclinic eddy growth was more sensitive to the lower- than the upper-level baroclinicity, thus Lu et al. (2008) did the calculation of baroclinicity between 500 hPa and 850 hPa to try to explain the poleward extent of the Hadley cell. Therefore, the change in which level is more important to anomalies of zonal wind or eddy activity due to climate change? In the following experiments, we try to explore the impact of the thermal forcing on the jet shift in upper and lower level. However in our study, we mainly focus on what drives the change in the barotropic component of the jet which is not constrained by imposing heating. So the results may be different.

In this set of experiments, we separated the temperature gradient only forcing into two parts, one is the upper level forcing which was above 500 hPa, and the other one is what is left below 500 hPa. First of all, the temperature gradient above 500 hPa only forcing was shown in Fig. 5.3(a). There was a warming center just over 3K over the tropics, and with two cooling centers maximizing around -3K in both polar regions, both anomalies centering close to the tropopause. Based on this partial global warming forcing, the zonal wind response (Fig. 5.3(b)) was very close to that in temperature gradient only forcing experiments (Fig. 5.2(c)). The distribution of wind anomalies were almost the same, positive at polar side of mid-latitude jets and negative at equator side, indicating poleward shift of jets. While the maximum of wind changes for above forcing was a little bit smaller than that for temperature only forcing, by order of 1~2 m/s which was much smaller than the maximum value especially in the Southern Hemisphere.

Meanwhile, the forcing below 500 hPa was plotted in Fig. 5.4(a). There was a warming center of about 5K over the north pole near the surface, and a slight cooling at the Southern Hemisphere high latitudes near the surface. How would this forcing below 500 hPa drive the mid-latitude jets? From Fig. 5.4(b), we found that the Northern Hemispheric jet moved equatorward with this decreased temperature gradient at the surface, but the anomalies were very weak compared with the jet shift driven by forcing above 500 hPa. This equatorward shift of jet could partially offset the poleward shift in the NH, making the shift weaker than in the SH. In the Southern Hemisphere, the anomalies were quite negligible compared to what shown in Fig. 5.3(b). Because in this study we are focusing on the variations in the Southern Hemisphere first, in the discussions below we will focus on the forcing above 500 hPa which does not take into account the surface warming near the north pole.

b. Localized static stability change without changing temperature gradient

So far we have found that the horizontal temperature gradient anomalies near the tropopause due to global warming contributed much more on mid-latitude jet poleward shift, than the global static stability change or temperature gradient decreased near the surface. However in the first hypothesis we mentioned in introduction, the static stability over subtropics may have some impact on jet shift. In this set of experiments, we tried to examine if localized static stability change played a role in driving the mid-latitude jet poleward.

(1). Static stability change over polar regions

Actually it is impossible to completely separate the effect of the static stability or the horizontal temperature gradient. In this study, we tried to examine the effect of each one individually. We have already known that the global static stability change had a very weak impact on jet shift, so here localized change in static stability would be our focus. Based on the temperature gradient only above 500 hPa forcing (Fig. 5.3(a)), the warming over tropics has been removed by subtracting the maximum value in the center at all latitudes. Therefore, with the horizontal temperature gradient unchanged, the thermal forcing turns out to be almost no change over tropics and two very strong cooling centers over polar regions, hereafter is called “SS1 forcing”, shown in Fig. 5.5(a). Under this forcing, the static stability is substantially reduced over polar regions near the tropopause in both hemispheres, while over tropics there is only very weak.

Comparing the forcing in Fig 5.5(a) to the temperature gradient only forcing in Fig. 5.3(a) related to the climatology, the change in temperature gradient is the same while the change in static stability isn't. The zonal mean zonal wind response latitude-height cross section with the SS1 forcing is plotted in Fig. 5.5(b). In both hemispheres, the wind increases poleward of mid-latitude jets and decreases toward equatorward flank of the jets, clearly signifying a poleward shift of jets. Meanwhile, the increase in the high latitude is much stronger than the decrease in the equatorward flank of jets, suggesting a strengthening of the mid-latitude jets, especially in the Northern Hemisphere. As we go back to check the wind anomalies in Fig. 5.3(b) being with temperature gradient only above 500 hPa forcing, these two wind responses are very similar in the Southern Hemisphere in terms of the relative strength of poleward shift jets and jet intensity. However in the Northern Hemisphere, the poleward shift of jet is only robust near the surface in Fig. 5.3(b) under temperature gradient only forcing, and the jet strengthening is stronger when the static stability decreased more over polar regions, as shown in Fig. 5.5(b). Overall, wind anomalies in Fig. 5.3(b) and in Fig. 5.5(b) are quite similar despite some slight differences in the NH.

(2). Static stability change over tropics

Different from part (1) but using the same idea, we removed the two cooling centers over polar regions in both hemispheres without changing the horizontal temperature gradient, to further explore the impact of the localized static stability or the temperature gradient on poleward shift of mid-latitude jets under global warming. We call it "SS2 forcing", as shown in Fig. 5.6(a). The SS2 forcing highlights the increased static stability over the tropics with very little changes over high latitudes near the tropopause, which has the same horizontal temperature gradient but different static stability as the SS1 forcing shown in Fig. 5.5(a). Driven by SS2 forcing, the zonal wind response in dry model is shown in Fig. 5.6(b), demonstrating poleward shift of mid-latitude jets in both SH and NH given the positive anomalies in the poleward flank of jets and negative responses toward equatorward.

In Fig. 5.6(b), the wind response shows a stronger magnitude and a comparable difference between the positive and negative maximum in the SH, implying a little bit of stronger jet poleward shift but the relatively same jet strengthening compared with anomalies forced by the SS1 forcing shown in Fig. 5.5(b). They also are quite similar to the wind anomalies driven by temperature gradient only forcing shown in Fig. 5.3(b) in the SH. While in the NH compared to Fig. 5.5(b), the vertical and latitude distribution of the jet response in Fig. 5. 6(b) is more similar to that driven by temperature gradient only forcing in Fig. 5.3(b). The mid-latitude jet exhibits a robust poleward shift only near the surface and a weak strengthening just as what shown in Fig. 5.3(b), but quite differs from what shown in Fig. 5.5(b). This might be a hint that the localized static stability change around the tropopause could be a factor with respect to jet variations in the Northern Hemispheric. However, the results discussed in this section suggest that local static stability change is not an important factor driving the jet shift in the Southern Hemisphere.

iii. Tropopause height rise at all latitudes

Apart from the horizontal temperature gradient anomalies near the tropopause, the global warming could have raised the tropopause height because of the warming in the upper troposphere just beneath the tropopause and the cooling in the whole stratosphere above the tropopause. It is of great interest for us to explore if the rise of tropopause height does play an important role in making mid-latitude jet shift poleward. Lorenz and DeWeaver (2007) found that the change in upper tropospheric lapse rate between the 20th and 21st century in IPCC AR4 simulations is consistent with a 400 m rise in the tropopause, especially in the midlatitudes. They suggested that the rise of tropopause height is the primary factor driving the jet poleward, with other factors such as the change in the low-level pole-to-equator temperature gradient and increased moisture content playing a secondary role. Here we will use our model setup to explore this mechanism.

In the experiments of Lorenz and DeWeaver, raising the tropopause is very easy since in their idealized Held-Suarez forcing, the radiative equilibrium temperature of the stratosphere is a constant temperature, and raising the tropopause can be achieved simply by lowering the radiative equilibrium temperature of the stratosphere. However, in our experiments, the temperature profile is forced to be similar to the earth's atmosphere, thus the temperature of the tropopause varies with location, and a procedure similar to that used by Lorenz and DeWeaver cannot be applied. To lift the tropopause, we use the following procedure. First, we interpolate the 17 pressure levels of NCEP climatology in 20th century onto 99 regular levels with 10mb interval. After the interpolation, we found several layers with thickness of around 60mb having very similar lapse rate at all latitudes below the tropopause. We choose one layer between 470 hPa to 410 hPa and replace the two levels above with the lapse rate of this layer (or the four levels above) at all latitudes, and shift all the layers above upward. In this way we expand the layer with similar lapse rate by 20 hPa (or 40 hPa respectively) to implement the rise of tropopause height at all latitudes.

The vertical temperature profiles over the tropics and south pole for the control run and raised tropopause cases are shown in Fig. 5.7. The latitude-height cross sections of temperature anomalies of raising the tropopause by 20 hPa and 40 hPa using our procedure have been plotted in Fig. 5.8(a) and (b) respectively. Note that in the climatological profile, the lapse rate over the tropics becomes larger above 400 hPa, hence our procedure gives rise to increase in the radiative equilibrium temperature in the tropical upper troposphere just below the tropopause (see Figs. 5.7 and 5.8), instead of just cooling above the tropopause related to lifting of the tropopause. Hence our forcing involve not only raising the tropopause, but also acts to enhance the temperature gradient between 300 and 100 hPa because of this additional tropical warming. As discussed above, previous studies have suggested that enhanced temperature gradient near the tropopause acts to shift the jet poleward, hence our experiments should be interpreted as setting the upper bound on how much raising the tropopause can shift the mid-latitude jet poleward. The anomalies shown in Figs. 5.7 and 5.8 are the forcing we add to the climatology to construct the target temperature profiles for experiments testing the impact of raising the tropopause height.

Driven by the forcing of raising the tropopause height in the dry model, the zonal mean zonal wind responses for tropopause rise by 20 hPa and 40 hPa are shown in Fig. 5.9(a) and (b), respectively. For 20 hPa case, the wind responses are weaker than the other global warming forcings compared to the total forcing, by around 3 m/s maximum of positive wind anomalies in the poleward flank of the mid-latitude jets, and slightly weaker negative peak toward the equatorward flank. When the tropopause height is lifted by 40 hPa, the zonal wind responses become quite strong. The maximum positive and negative wind change in both hemispheres for raising tropopause 40 hPa case are almost linearly 2 times that of raising tropopause 20 hPa case. Nevertheless, comparing the responses to raising tropopause height (Fig. 5.9) with that given by the full temperature forcing (Fig. 5.2b), it can be seen that the response to a 40 hPa rise of tropopasue height is still slightly weaker than that due to the full forcing, especially in the Southern Hemisphere.

5.3.2 Experiments with diabatic feedback

In Chapter 4, we found a rather long timescale for the zonal index variability in the dry model run which can be substantially reduced by imposing some extra diabatic feedback. And we also mentioned in the previous section that the jet response is quite strong in the dry model compared with those found in GCMs. Therefore, in this part, the missing diabatic feedback will be incorporated in the simulations so that the results presented in the last section based on dry model runs without diabatic feedback can be validated when the zonal index timescale is closer to that found in the real atmosphere. As discussed in Chapter 4, the diabatic feedback can be mimicked in two different ways:

i) By imposing time varying but spatially fixed latent heat of precipitation (Fig. 4.6 as a function of eddy momentum forcing at the previous time step (called FEEDBACK 1 below); and ii) By imposing interactive heating by parameterizing heating as a function of ω in mid-latitude regions with upward motion (see equation 4.5; this approach will be called FEEDBACK 2 below). The global warming forcings are still the same as those used in the dry model experiments discussed above. For each imposed diabatic feedback, the control run was rerun with forcing tuned so that the climatology approaches that of the NCEP climatology temperature profile. Note that for the interactive heating experiments, the climatological static stability is not reduced (see discussions in section 4.3.3. All the differences discussed below are between the global warming forcing runs and their respective control runs.

i. Total forcing versus global static stability change

The zonal wind anomalies for the global warming total forcing (Fig. 5.1a) for the experiments with diabatic feedback are shown in Fig. 5.10. For comparison, the anomalies for the dry simulation without diabatic feedback have been shown in Fig. 5.2b. For FEEDBACK 1 (Fig. 5.10a), the mid-latitude jet's poleward shift in the Southern Hemisphere is nearly as strong as it is in the dry model simulations. However in Fig. 5.10(b) we can see that for experiments with FEEDBACK 2, the mid-latitude jet in the SH still shifts poleward, though the magnitude of jet anomalies becomes weaker and is now only about half of that in the other experiments. With respect to wind responses in the Northern Hemisphere, the anomalies are quite similar in terms of not only positions but also amplitudes for both experiments, and a clear poleward shift is not seen. It is clear that for these three cases, comparing the jet anomalies found in the dry runs (Fig. 5.2b), in the experiments with FEEDBACK 1 (Fig. 5.10a) and with FEEDBACK 2 (Fig. 5.10b), the one with FEEDBACK 2 has the weakest response and resembles the GCM results (Fig. 5.1b) the most. Based on fluctuation-dissipation theorem mentioned before, this is what we should expect because the jet variability timescale in experiments with FEEDBACK 2 is found to be reduced significantly to approach that found in the GCM experiments (see Chapter 4).

In Fig. 5.11, results for the temperature gradient only forcing is plotted. The results are very similar to those for the total forcing experiments (Fig. 5.10). In Fig. 5.12, the wind anomalies in the experiments with global static stability forcing are shown. The anomalies are very weak, with maximum amplitude of about 1 m/s. These results are consistent with the dry model simulations with no feedback (Figs. 5.2c,d).

As discussed above, based on the fluctuation-dissipation theorem, we expect that the amplitude of zonal index-like climate response (i.e. jet latitude shift) to imposed forcing would be roughly proportional to the auto-decorrelation timescale of the zonal index variations. In Fig. 5.13, the autocorrelation of the jet shift mode in the control runs for dry model and experiments with the two diabatic feedbacks added are compared with each other. The black line represents the autocorrelation of the zonal index computed from the dry model, having the longest timescale of jet shift mode. The green line stands for the experiments with diabatic FEEDBACK 1 added, showing a somewhat shorter timescale compared with the black line. Finally, the red line is for the runs with FEEDBACK 2 added, indicating the shortest timescale which is much shorter than that indicated by the green line for FEEDBACK 1. This is consistent with the results discussed in Ch. 4.

Fig 5.14 shows the timescale comparisons for the experiments with different global warming forcings added. Fig. 5.14, (a), (b) and (c) shows the global total forcing, the temperature gradient only forcing and the global static stability forcing, respectively. It is apparent that in all cases, the timescale of the SH zonal index is slightly reduced by adding FEEDBACK 1, and is significantly reduced by imposing FEEDBACK 2. This result is consistent with those for the control experiments shown in Fig. 5.13. We have also computed the timescales for experiments with other forcings imposed and the results are similar. Hence, in all experiments, the dry model (no feedback) case has the longest zonal index time scale, while the experiments with FEEDBACK 1 have slightly shorter timescale, and the experiments with FEEDBACK 2 have significantly shorter timescales. This is consistent with the relative amplitude of the jet shift response found in these different experiments.

ii. Lifting tropopause height

When the tropopause height is lifted by 20 hPa, the zonal wind responses with the two diabatic feedbacks are shown in Fig. 5.15. These should be compared to the no feedback case shown in Fig. 5.9a. For FEEDBACK 1, the positive wind anomalies under forcing of raising the tropopause height (Fig. 5.15a) are at the poleward flank of the mid-latitude jets for both hemispheres, and the negative anomalies are toward the equatorward flank, suggesting a poleward shift of mid-latitude jets. And the positive maximum is slightly larger than the negative one, indicating a slight strengthening of jets. The wind response for FEEDBACK 2 shown in Fig. 5.15(b) is much weaker in the Southern Hemisphere than wind response of FEEDBACK 1. In Fig. 5.16, the responses to raising the tropopause height by 40 hPa are shown. The wind responses for raising the tropopause by 40 hPa are much stronger: almost twice as strong as those for raising the tropopause by 20 hPa. Again in the SH, jet response with FEEDBACK 1 added is much stronger than that in experiments with FEEDBACK 2. While in the NH, jet anomalies are more concentrated in upper level for FEEDBACK 2, indicating a more baroclinic structure compared with the experiments of adding FEEDBACK 1 in which the jet response is more barotropic.

Similar to the dry model case discussed above, when the responses to raising tropopause height (Figs. 5.15 and 5.16) are compared to those given by the full forcing (Fig. 5.11), it is again apparent that more than 40 hPa of tropopause height rise is needed to attain the same jet shift as that achieved by the full forcing (as well as the temperature gradient only forcing). As discussed above, based on the zonal index timescale found in these experiments, we expect that the results based on the FEEDBACK 2 experiments to be most realistic. Comparison between Figs. 5.15-5.16 with Fig. 5.1b suggests that over 40 hPa tropopause height rise is needed for the experiments with FEEDBACK 2 to produce the amount of jet shift found in IPCC AR4 experiments. As discussed above, Lorenz and DeWeaver (2007) showed that the IPCC AR4 experiments project a tropopause height rise of about 400 m, which is equivalent to about 15 hPa rise in tropopause height in the mid-latitudes. Thus our results suggest that such a magnitude (400m) of tropopause height rise is far from being able to account for the magnitude of jet shift found in the IPCC AR4 GCM simulations. We hypothesize that the results of Lorenz and DeWeaver (2007) are similar to those of our dry experiments with no diabatic feedback, in which the long autocorrelation time scale of the zonal index mode gives rise to an overly sensitive model response to the imposed forcing. Therefore from the results of our experiments, we conclude that the temperature gradient change near the tropopause is the most important factor responsible for the jet poleward shift, followed by the tropopause height rise, whereas the static stability change is not important.

5.4 Conclusion and discussion

In this idealized modeling study, we forced the dry model to a realistic climate and impose realistic forcings based on IPCC AR4 model projected temperature change to assess factors that are important in forcing the poleward shift of mid-latitude jet under global warming scenarios .In this study, we mainly focus on the Southern Hemisphere. Given that the timescale of the jet shift mode (the zonal index) in the dry model is much longer than that diagnosed for the real atmosphere or in GCM simulations, two different diabatic feedbacks have been imposed in the dry model runs to suppress the jet shift mode, making the timescale shorter and closer to that of the real atmosphere. Results from these three different experiments are compared to assess the robustness of the model response.

We use the multi-model ensemble mean temperature response to the A1B and A2 CO_2 emission scenarios in IPCC AR4 model simulations as the global warming forcing in this study. The temperature increases throughout the troposphere with largest increase in the tropical upper troposphere, and decreases in the stratosphere, giving rise to a strong enhanced meridional temperature gradient near the tropopause. The mid-latitude jet in the SH shifts poleward and intensifies a little in GCM runs. The response in the dry model without diabatic feedback also indicates poleward shift in the mid-latitude jets but the magnitude is much stronger.

Further experiments are conducted by separating the total forcing into two different thermal forcings: the global static stability forcing which is the global mean temperature change at each level and the temperature gradient only forcing which is the remainder. The jet response in experiments driven by the static stability forcing is quite weak, in the order of less than 1 m/s, while the zonal wind anomalies between experiments of the total forcing and the temperature gradient only forcing are very close to each other, in terms of either the distribution of wind anomalies or the magnitude of the changes. These results suggest that the changes in horizontal meridional temperature gradient rather than in the global static stability dominates the contribution to the poleward shift of mid-latitude jets. The change in temperature gradient appears to be more crucial to the change in jet latitude than the impacts of static stability change.

Based on the temperature gradient only forcing, we designed several other experiments to further investigate several questions, including whether upper or lower level thermal forcing contributes more to the jet shift; and the impact of localized static stability increase. The temperature gradient only forcing has been divided into two parts, one above 500 hPa, the other below. Results show that the zonal wind response driven by forcing below 500 hPa, which mainly consists of strong polar warming in the Northern Hemisphere, acts to drive the Northern Hemisphere jet equatorward, consistent with the results of previous studies (Geng and Sugi 2003; Yin 2005; Deser et al. 2010). These studies also suggested that the jet shift was very sensitive to the lower level baroclinicity. However, in our experiments, the response is much weaker at lower level than the response driven by the forcing at upper level, suggesting that the thermal forcing under global warming near the surface has much less important effect on the jet shift mode than that near the tropopause. This could be an interesting topic to follow up in future studies.

Other experiments based on the temperature gradient only forcing are designed to change the static stability over the tropics or over high latitudes while without modifying the change in temperature gradient above 500 hPa. Through this set of experiments, we find that the jet response and strengthening are very similar between these two different static stability change experiments. Thus we conclude that the localized static stability's change either over tropics or high latitudes has very weak impact on the poleward shift of mid-latitude jets compared with the horizontal temperature gradient anomaly. These results are also consistent with the results of Butler et al. (2010).

Apart from the dry model experiments, we have also conducted experiments incorporating two simple representations of the diabatic feedback found in Chapter 4. Results of those experiments are largely consistent with those made with the control dry model (without diabatic feedback), except that the magnitude of jet shift found in the experiments with diabatic feedback is always smaller, with the results from FEEDBACK 2 most similar to those found in IPCC AR4 GCM experiments, consistent with the expectation based on the shorter (and more realistic) autocorrelation timescale of the zonal index mode found in the experiments with diabatic feedback incorporated.

Experiments have also been conducted to examine the hypothesis of tropopause height rise discussed in the introduction. Lorenz and DeWeaver (2007) suggested that a 400 m rise of the tropopause could account for the change due to global warming in IPCC GCMs, and the tropopause height rise the most important factor responsible for the poleward shift of jet However, our results suggest that such a magnitude of tropopause height rise is not likely to be sufficient for generating the amount of jet shift projected by IPCC models. We believe that the results of Lorenz and DeWeaver (2007) are likely biased due to their model being too sensitive to imposed forcing. Therefore, different from their conclusion, our results suggest that the tropopause height rise is not the most important factor, the temperature gradient change near the tropopause is the primary reason responsible for jet shift, and the static stability change is not important.

Comparing all our results from the dry model simulations and experiments with diabatic feedbacks, the jet responses in dry model run are always much stronger than those in experiments with diabatic feedbacks (especially with FEEDBACK2). The runs with stronger jet responses also have longer timescales of the zonal index (jet shift mode). Such a dependence of the model response on the timescale is consistent with the fluctuation-dissipation theorem. Many previous studies, including Haigh et al. (2005), Lorenz and DeWeaver (2007), Simpson et al. (2009), and Butler et al. (2010, 2011), have used dry mechanistic models similar to our dry model to examine jet response to heating. Since the dry models tend to have long zonal index timescales, results concerning jet shift response based on dry models should be reassessed to see whether the modeled response is too sensitive to the forcing due to a long zonal index timescale.

Model	Daily data in	Daily data in	With or without
BCCR_BCM2_0	1	1	without
CCCMA_CGCM3_1_t47	3	3	without
CCCMA_CGCM3_1_t63	N/A	1	without
CNRM_CM3	1	1	with
CSIRO_MK3.0	1	1	with
CSIRO_MK3.5	1	1	with
GFDL_CM2.0	1	1	with
GFDL_CM2.1	1	1	with
GISS_AOM	N/A	1	without
GISS_MODEL_E_H	N/A		without
GISS_MODEL_E_R	1	1	without
IAP_FGOALS1_0_G	1	1	without
INMCM3.0	1	1	without
IPSL_CM4	1	1	without
MIROC3_2_HIRES	N/A	1	with
MIROC3_2_MEDRES	1	1	with
MIUB_ECHO_G	1	1	
MPI_ECHAM5	1	2	with
MRI_CGCM2.3.2A	1	1	without
NCAR_CCSM	N/A		with
NCAR_PCM			with
UKMO_HADCM3			with
UKMO_HADGEM1			with

Table 5.1: The IPCC AR4 models description in the SRES scenarios (A2, A1B).

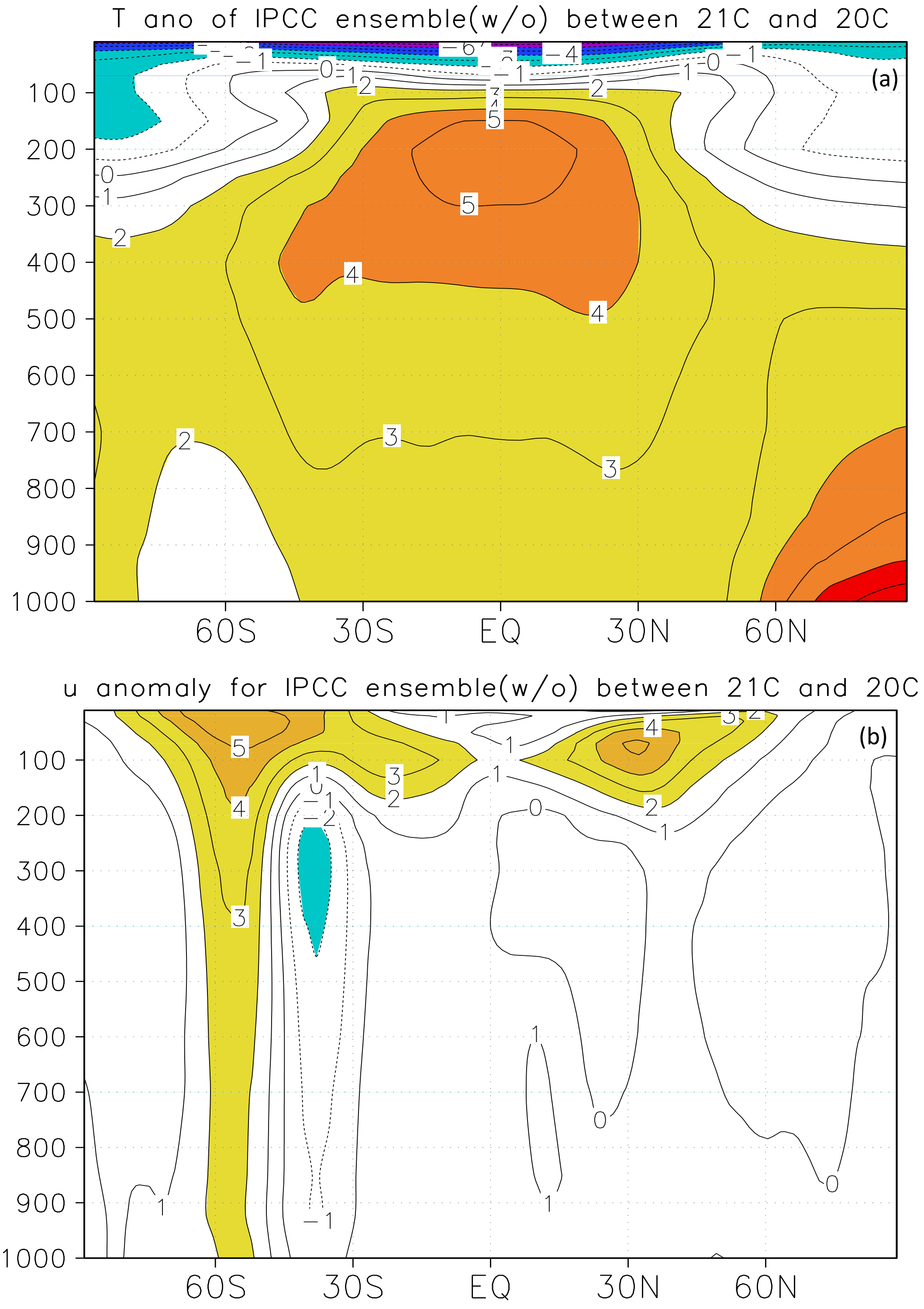

Figure 5.1: Zonal mean of temperature anomalies (a), zonal wind anomalies (b) between 2080-2100 and 1980-2000 DJF for the ensemble mean of IPCC AR4 coupled models without ozone recovery. Units: (a) K; (b) m/s (Note: anomalies larger than 2 are shaded in all panels)

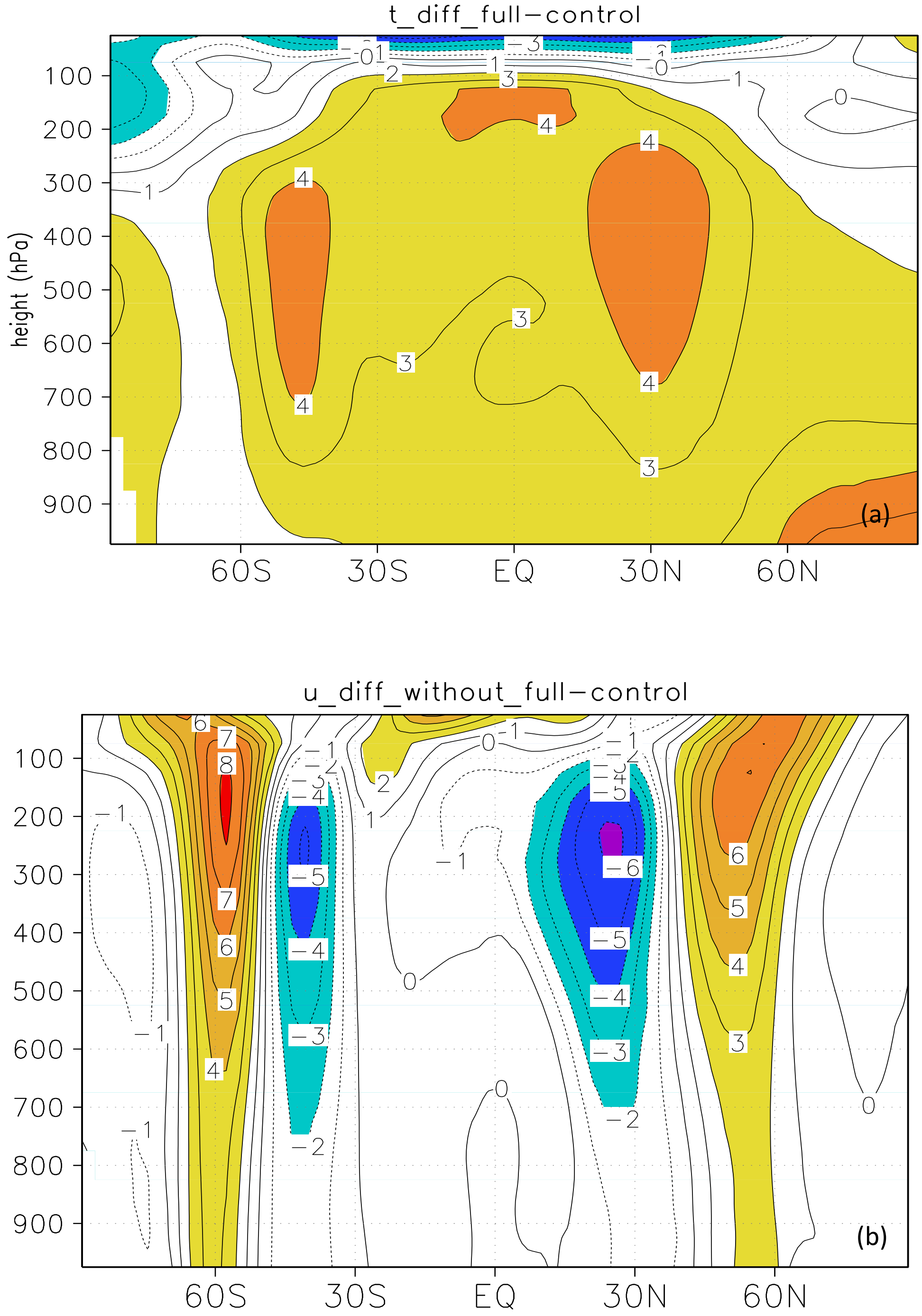
t_diff_full−control
height (hPa)
100
200
300
400
500
600
700
800
900
60S
30S
EQ
30N
60N
(a)
u_diff_without_full−control
(b)

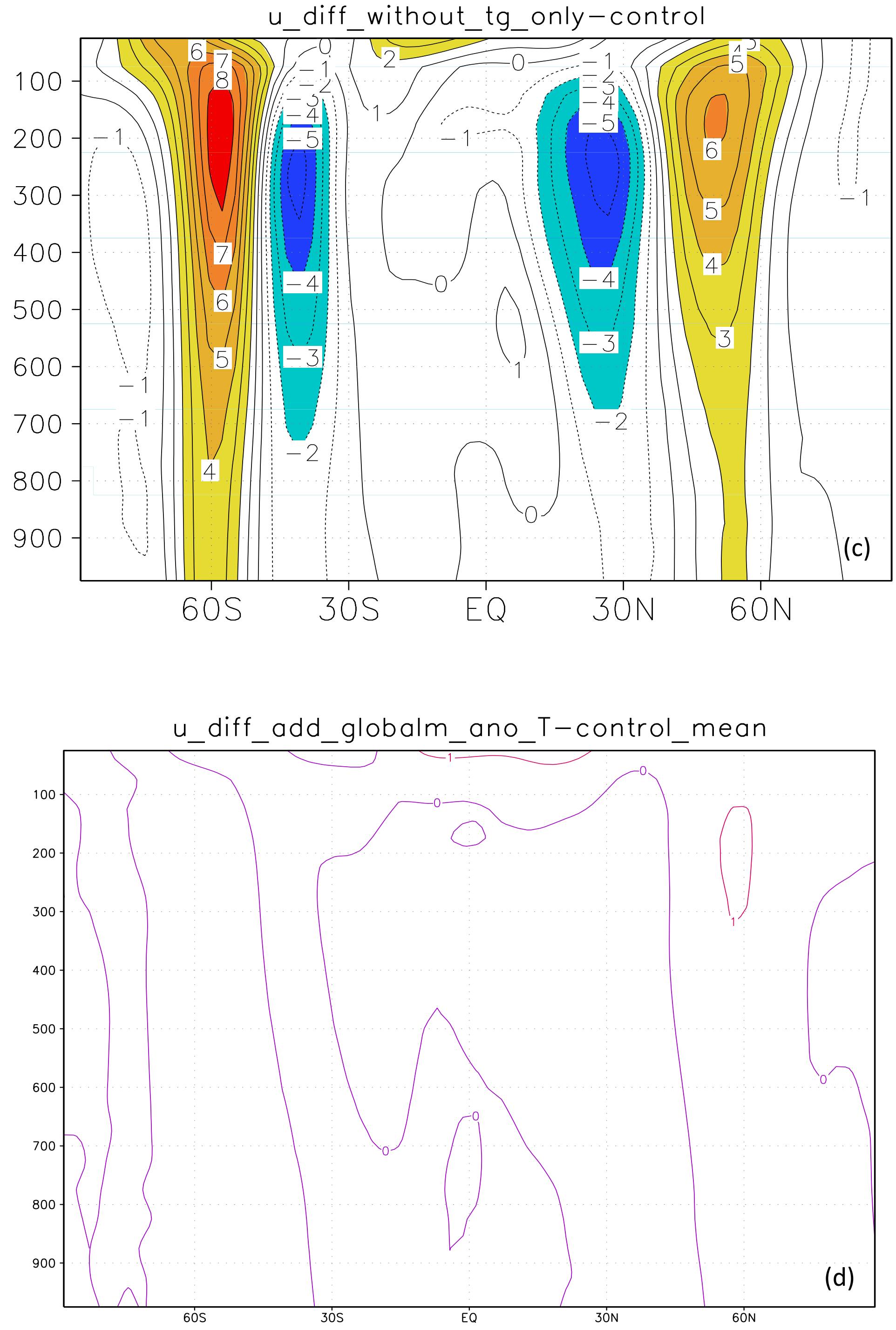

Figure 5.2: Zonal mean temperature response to global warming (a). Zonal mean zonal wind difference between global warming model run and control run, driven by (b) the total forcing, (c) the temperature gradient only forcing, and (d) the global static stability forcing. Units: m/s.

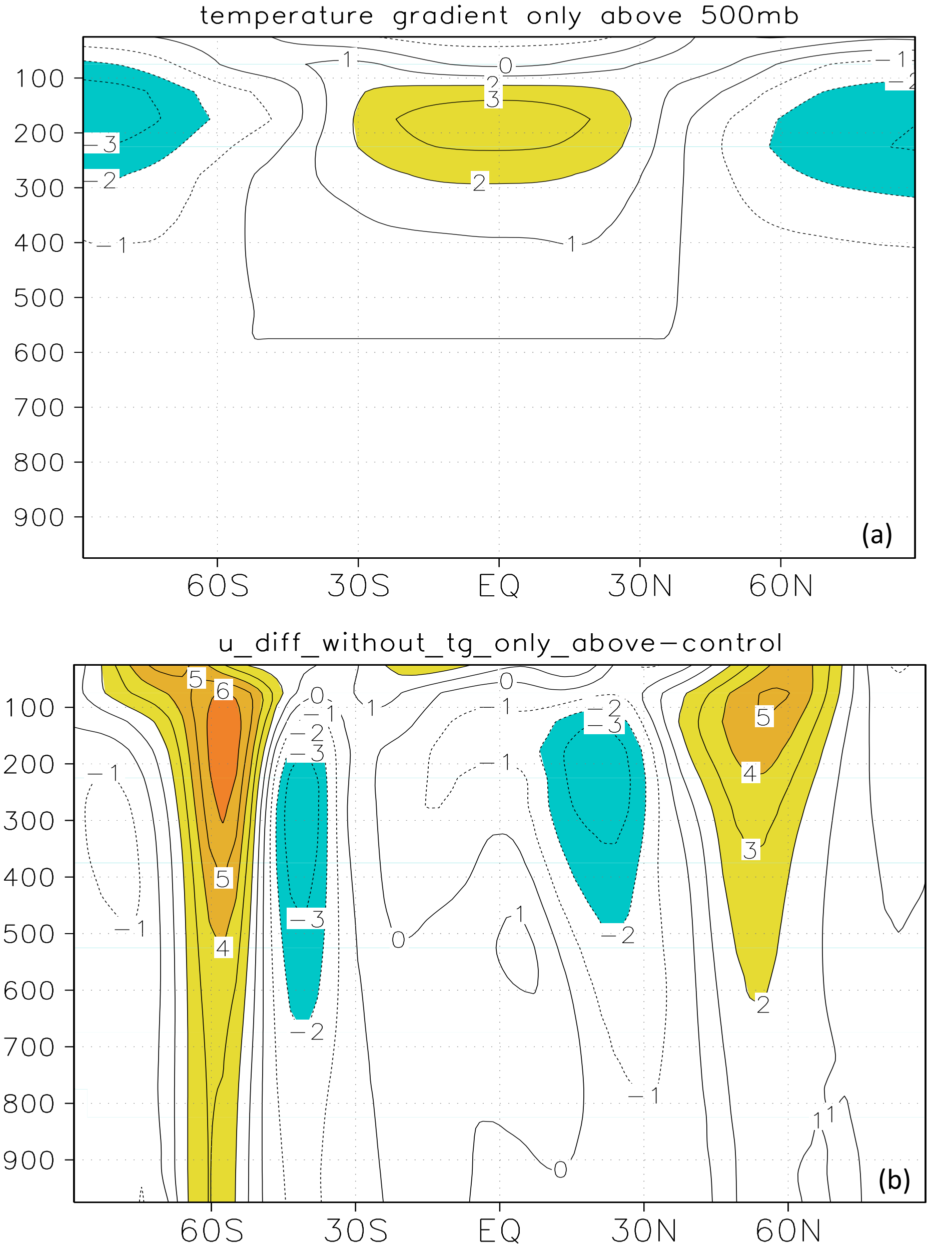

Figure 5.3: (a) Temperature gradient forcing above 500 hPa. (b) Zonal mean zonal wind anomalies between the temperature gradient only forcing and control run for dry model runs.

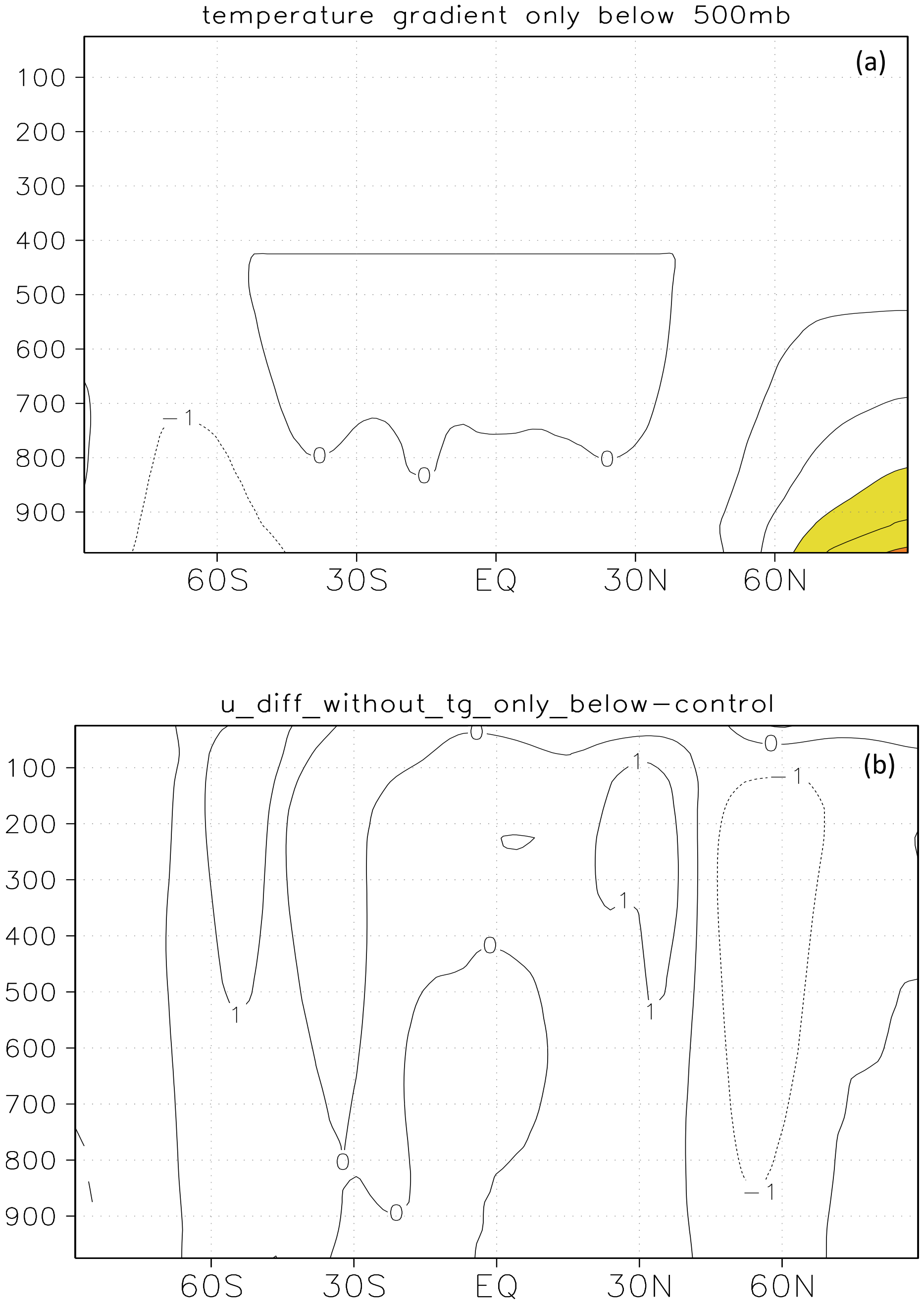

Figure 5.4: (a) Temperature gradient forcing below 500 hPa. (b) Zonal mean zonal wind anomalies between the temperature gradient only forcing and control run for dry model runs.

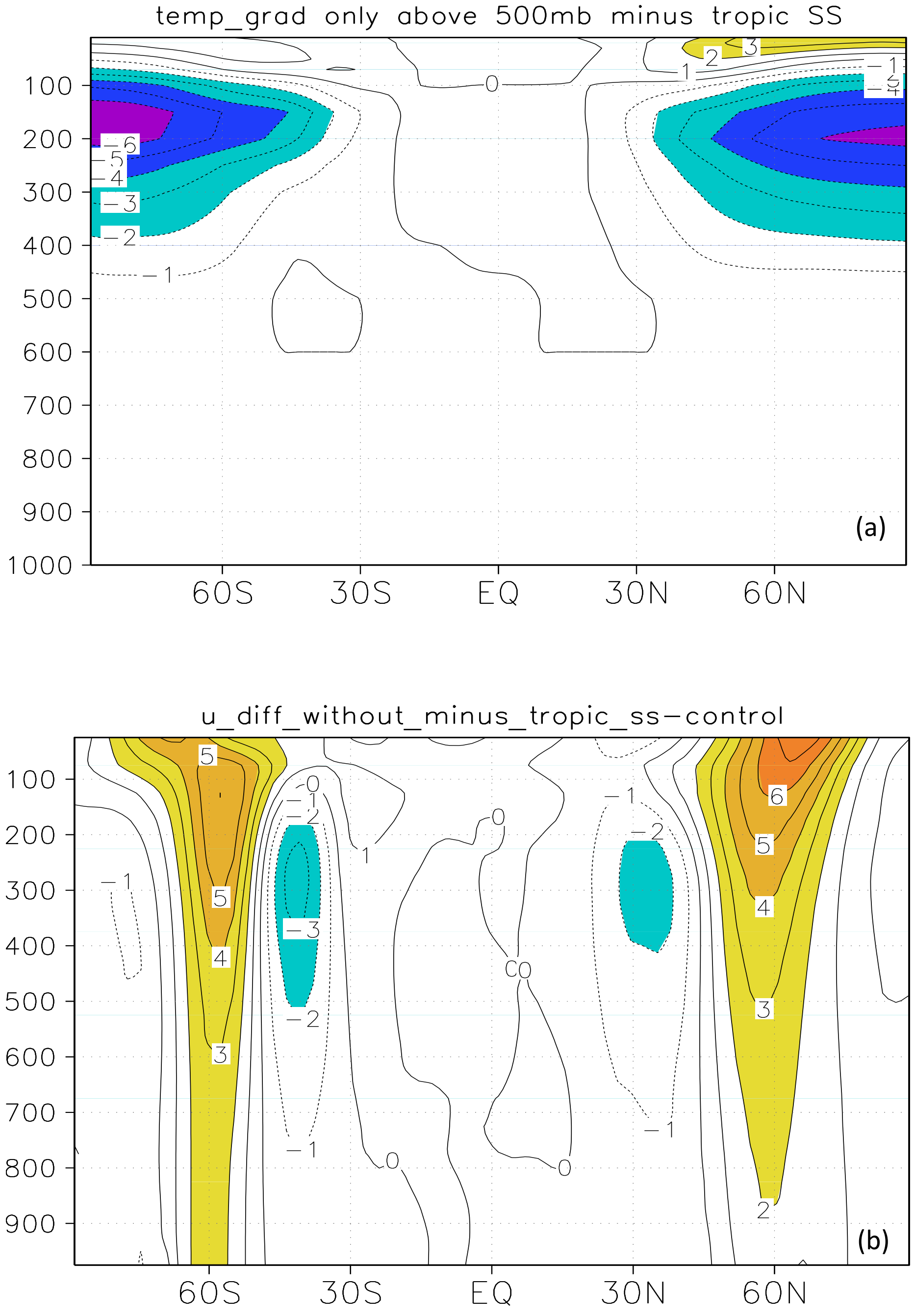

Figure 5.5: (a) Temperature gradient forcing above 500 hPa minus tropical warming (SS1 foricng). (b) Zonal mean zonal wind anomalies between the forcing shown in (a) and control run for dry model runs.

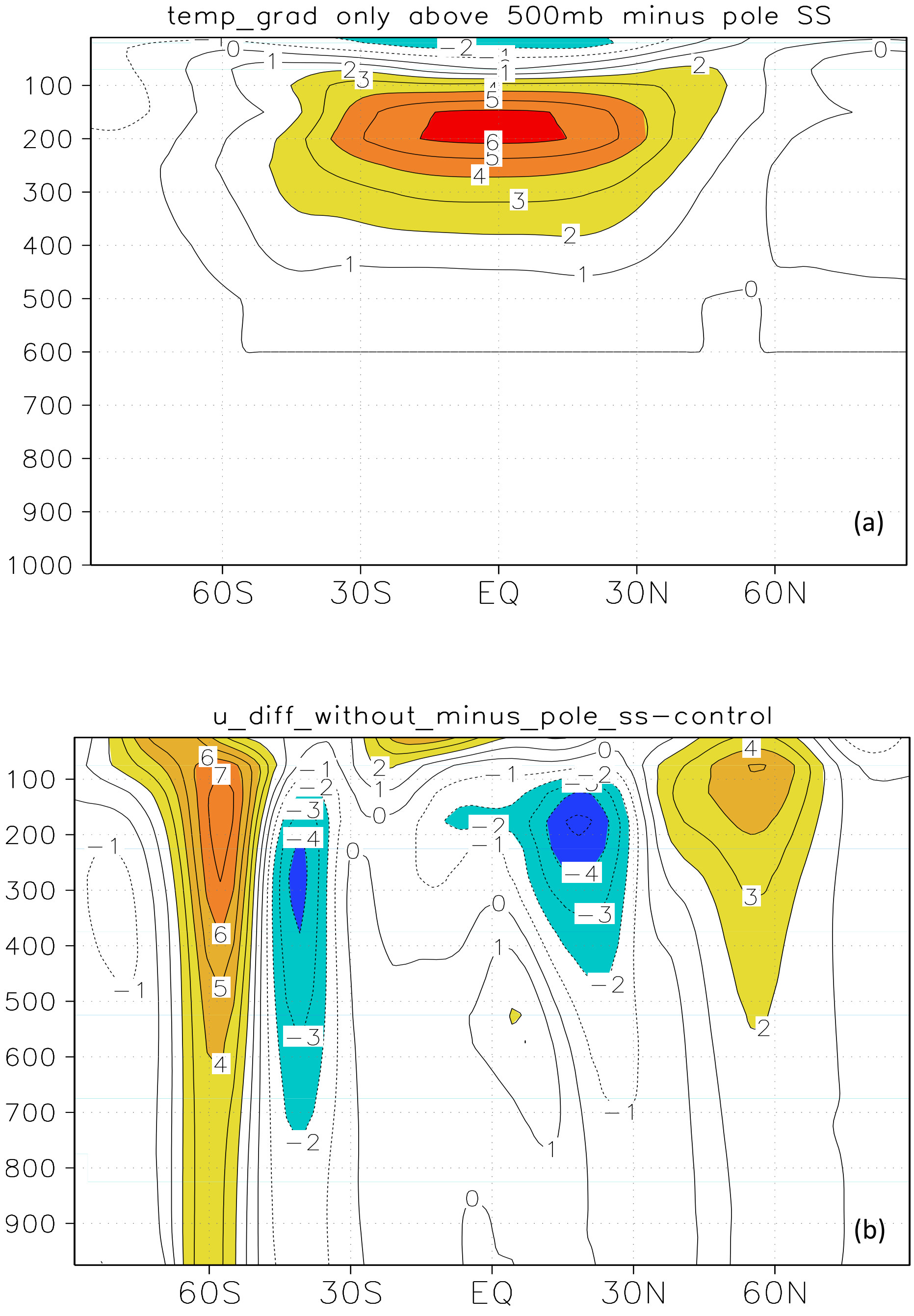

Figure 5.6: (a) Temperature gradient forcing above 500 hPa minus polar cooling (SS2 forcing). (b) Zonal mean zonal wind anomalies between the forcing shown in (a) and control run for dry model runs.

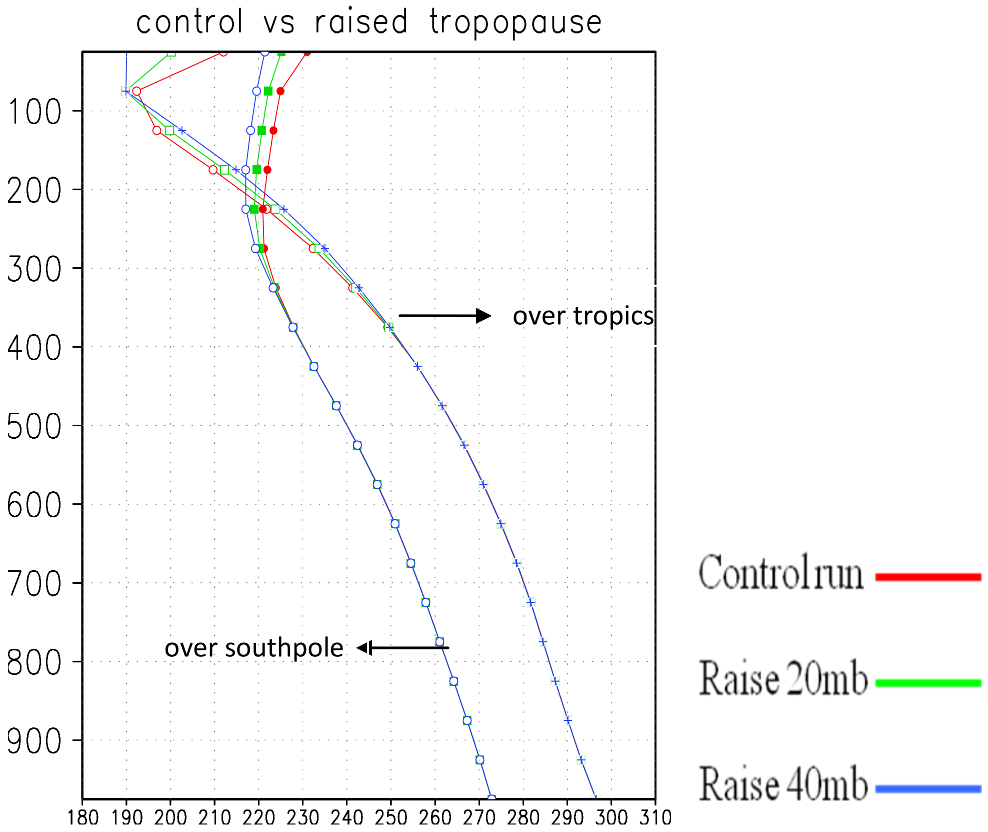

Figure 5.7: Vertical temperature profile for control run and raised tropopause cases. Units: K

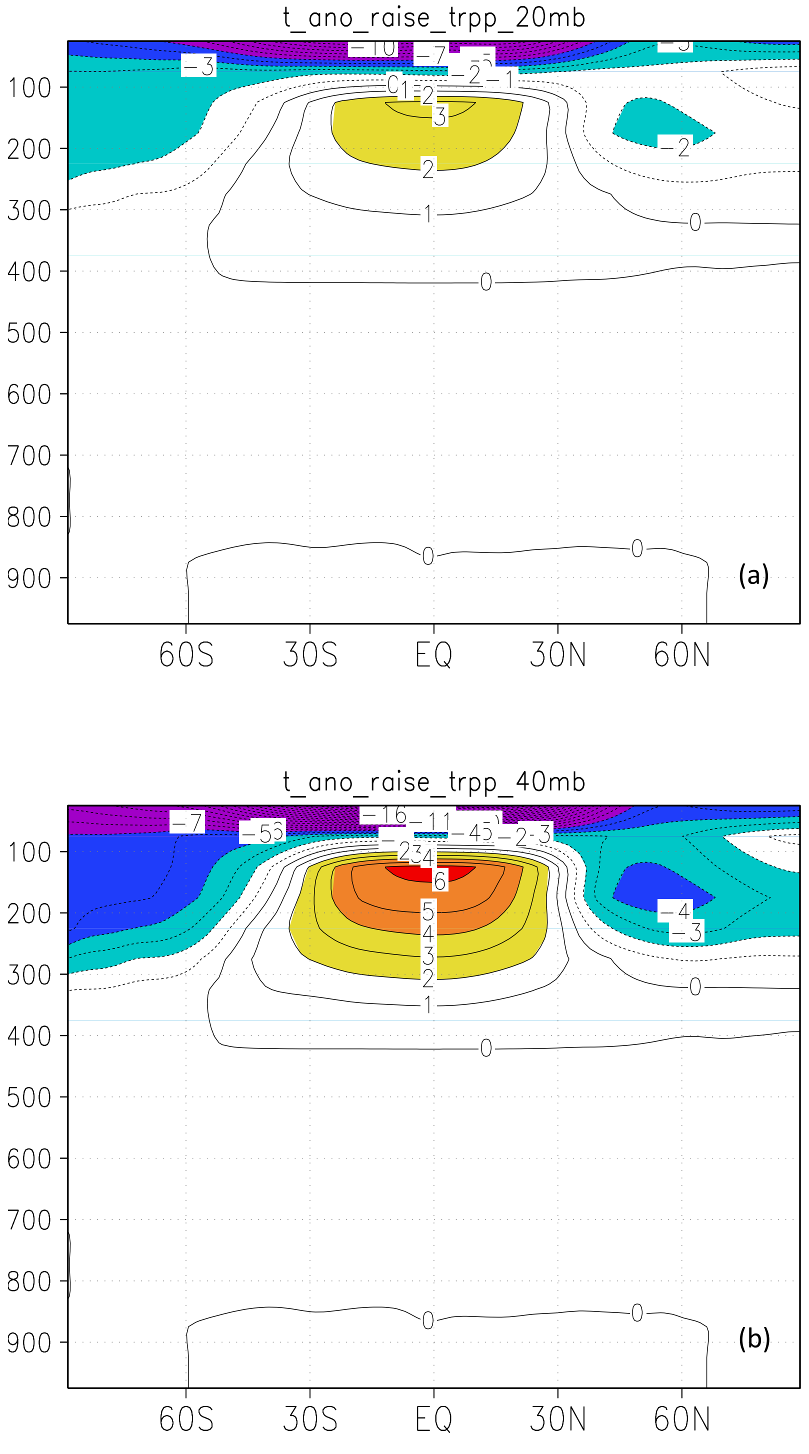

Figure 5.8: Temperature anomalies by raising tropopause height with different amplitude: (a) Raise by 20 hPa, (b) Raise by 40 hPa. Units: K

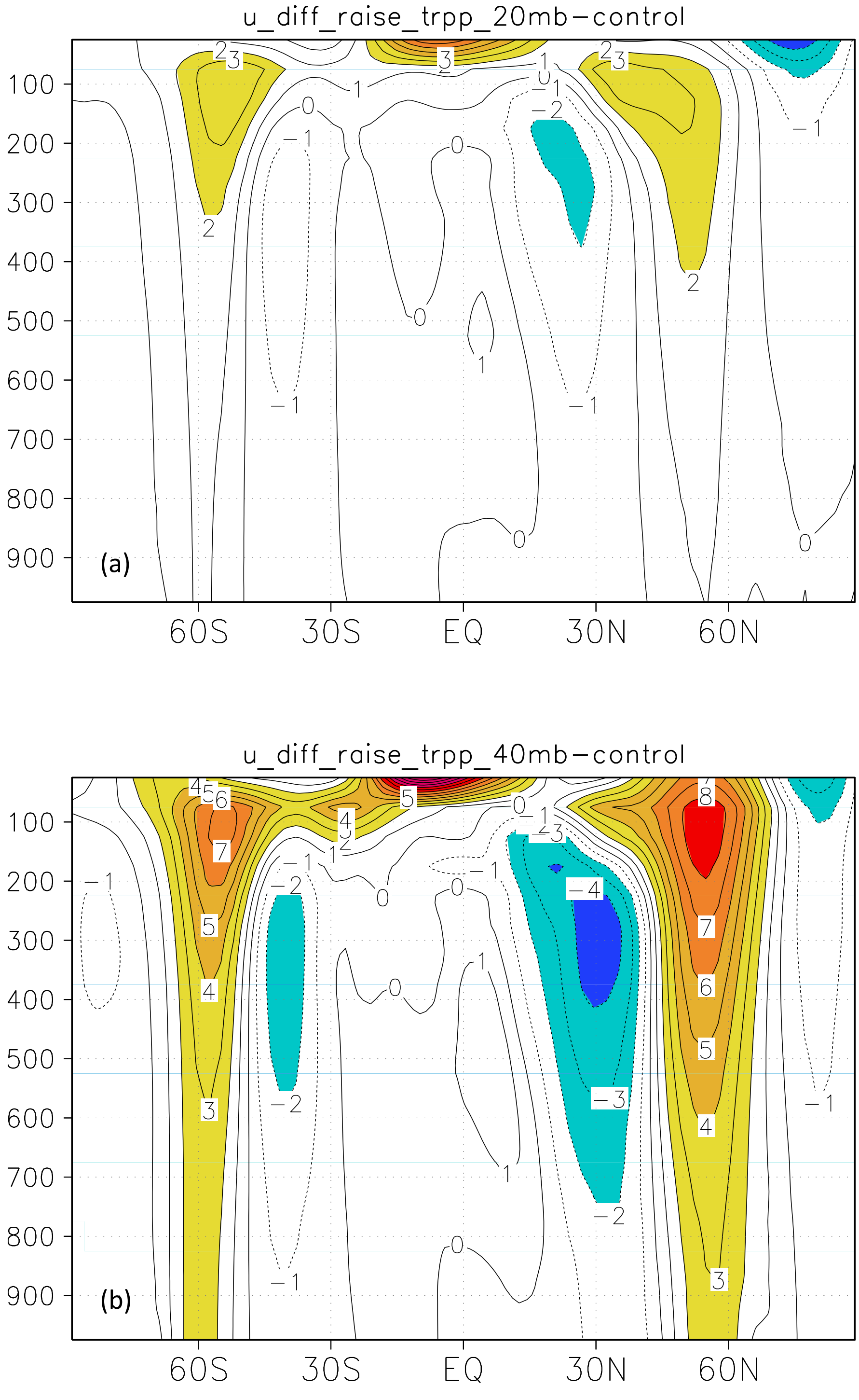

Figure 5.9: Zonal mean zonal wind differences between raising tropopause height forcing by (a) 20 hPa, (b) 40 hPa and control run. Unit: m/s

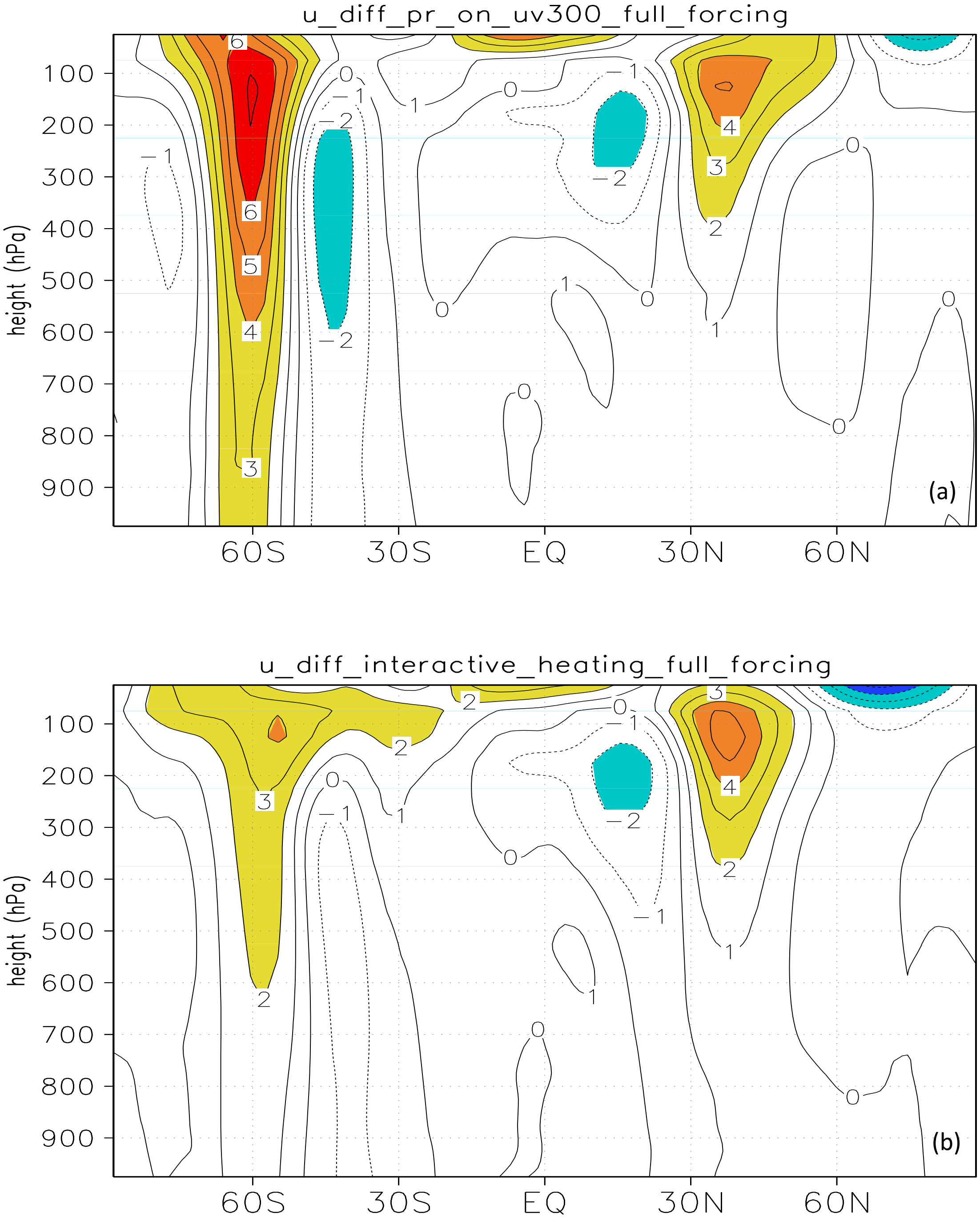

Figure 5.10: Zonal mean zonal wind anomalies between the total forcing and control run for experiments of imposing extra diabatic heating. (a) FEEDBACK 1; (b) FEEDBACK 2.

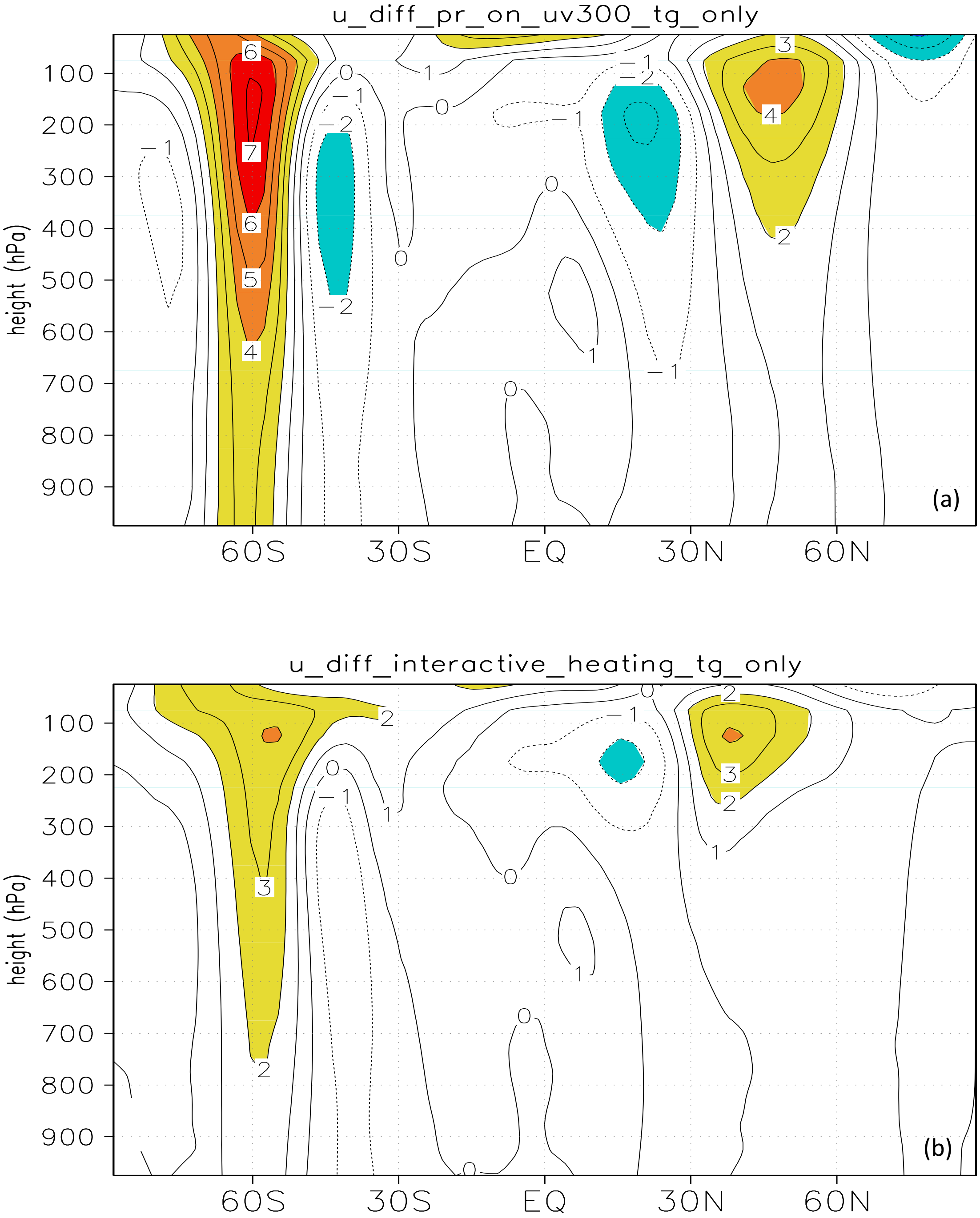

Figure 5.11: Zonal mean zonal wind anomalies between the temperature gradient only forcing and control run for experiments of imposing extra diabatic heating. (a) FEDDBACK 1; (b) FEEDBACK 2.

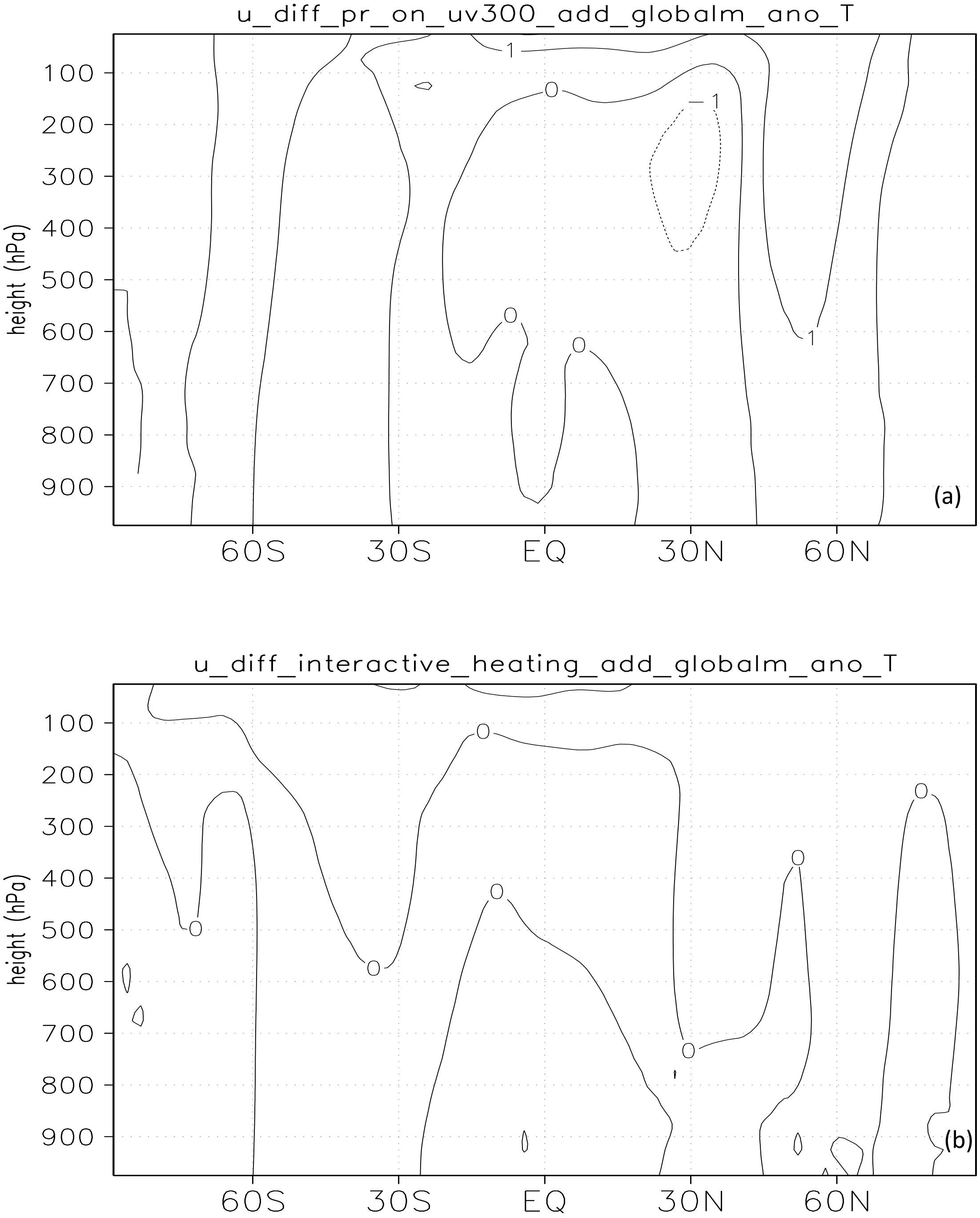

Figure 5.12: Zonal mean zonal wind anomalies between global static stability forcing and control run for experiments of imposing extra diabatic heating. (a) FEEDBACK 1; (b) FEEDBACK 2.

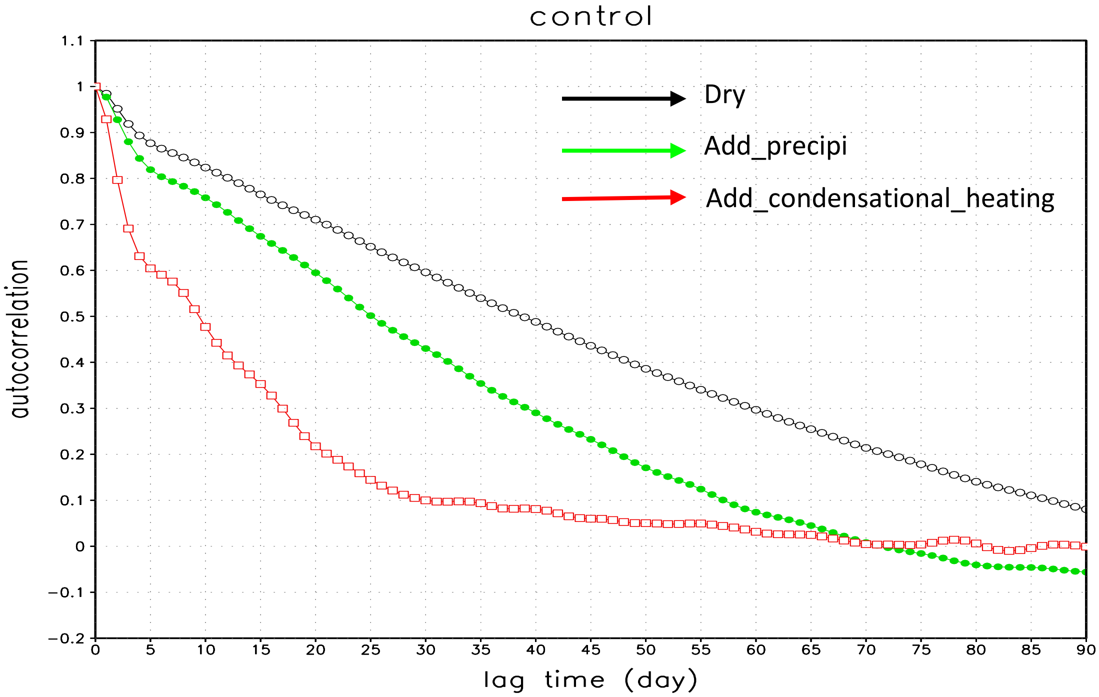

Figure 5.13: Auto-correlation of the jet shift mode in the control runs for the dry model run (black), FEEDBACK 1 (green), and FEEDBACK 2 (red).

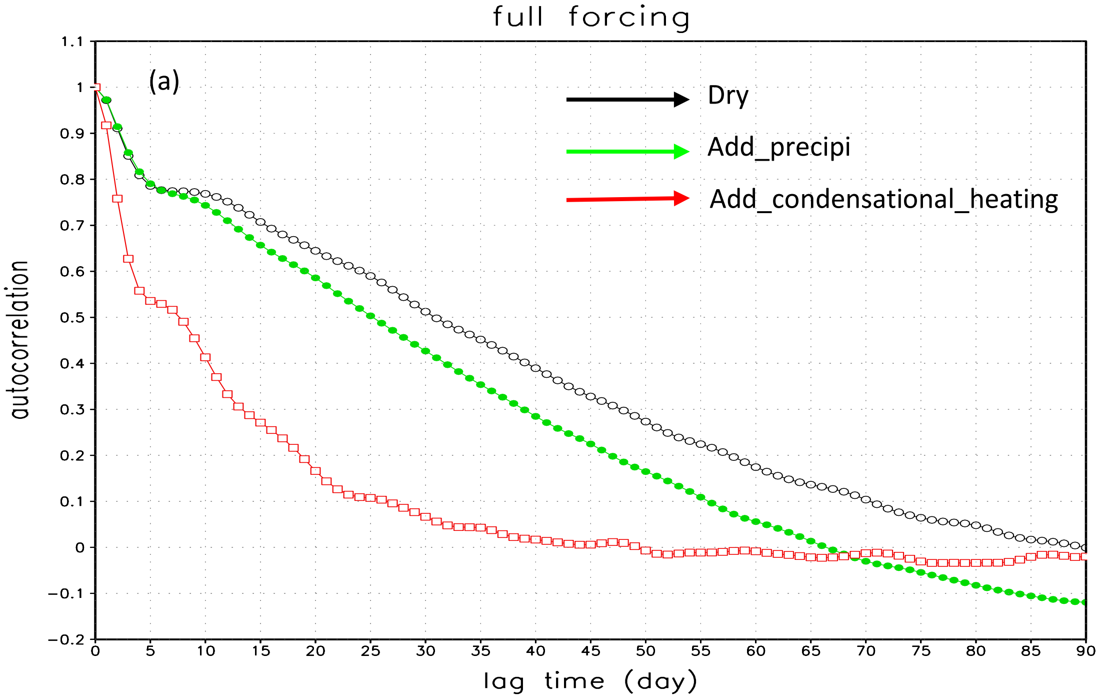
full forcing
(a)
Dry
Add_precipi
Add_condensational_heating
autocorrelation
1.1
1
0.9
0.8
0.7
0.6
0.5
0.4
0.3
0.2
0.1
0
−0.1
−0.2
0
5
10
15
20
25
30
35
40
45
50
55
60
65
70
75
80
85
90
lag time (day)

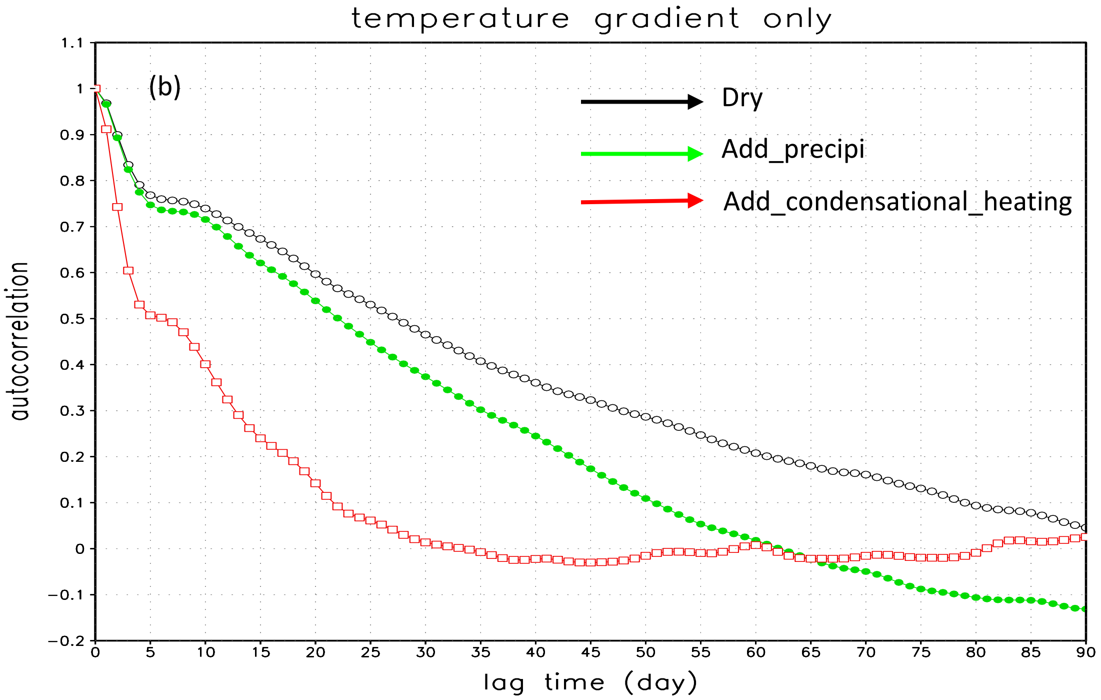
temperature gradient only
(b)
Dry
Add_precipi
Add_condensational_heating
autocorrelation
1.1
1
0.9
0.8
0.7
0.6
0.5
0.4
0.3
0.2
0.1
0
−0.1
−0.2
0
5
10
15
20
25
30
35
40
45
50
55
60
65
70
75
80
85
90
lag time (day)

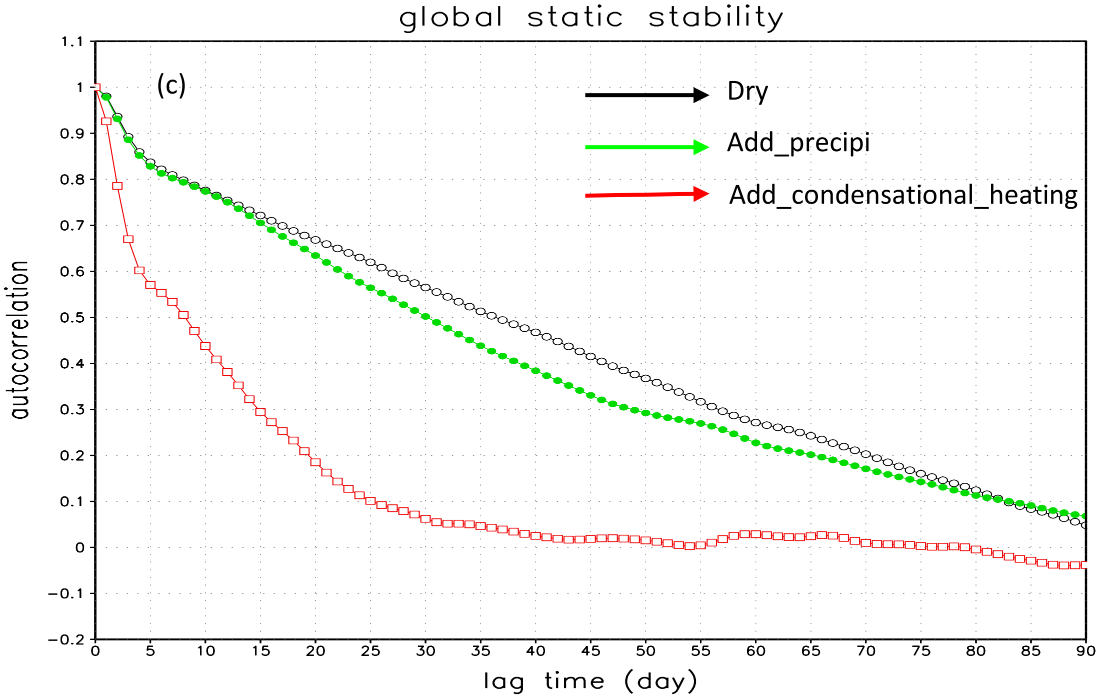

Figure 5.14: Auto-correlation as in Fig. 5.13 for runs driven by (a) the total forcing, (b) the temperature gradient only forcing, and (c) the global static stability forcing.

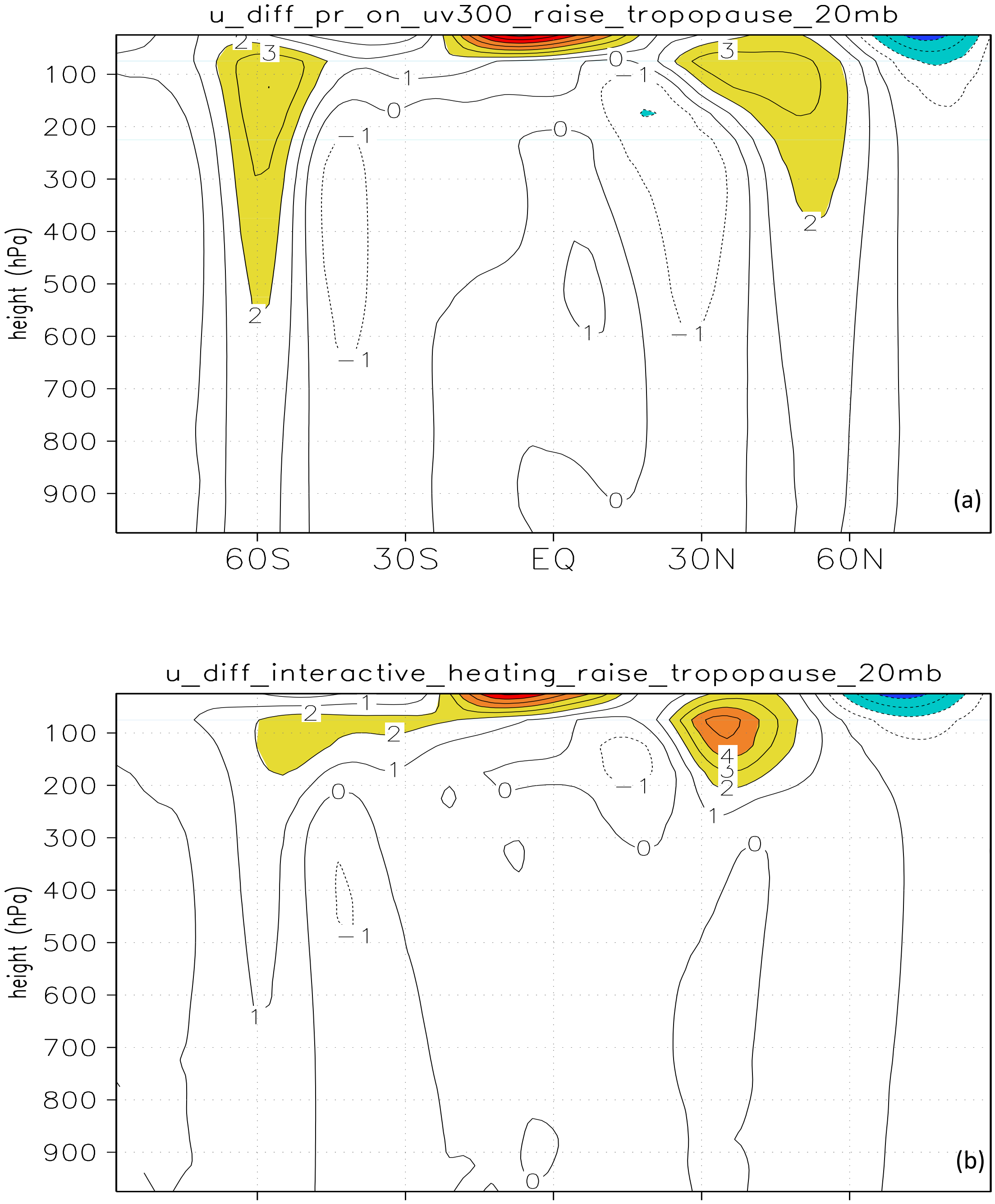

Figure 5.15: Zonal mean zonal wind anomalies between raising tropopause height 20 hPa forcing and control run for experiments of imposing extra diabatic heating. (a) FEEDBACK 1; (b) FEEDBACK 2.

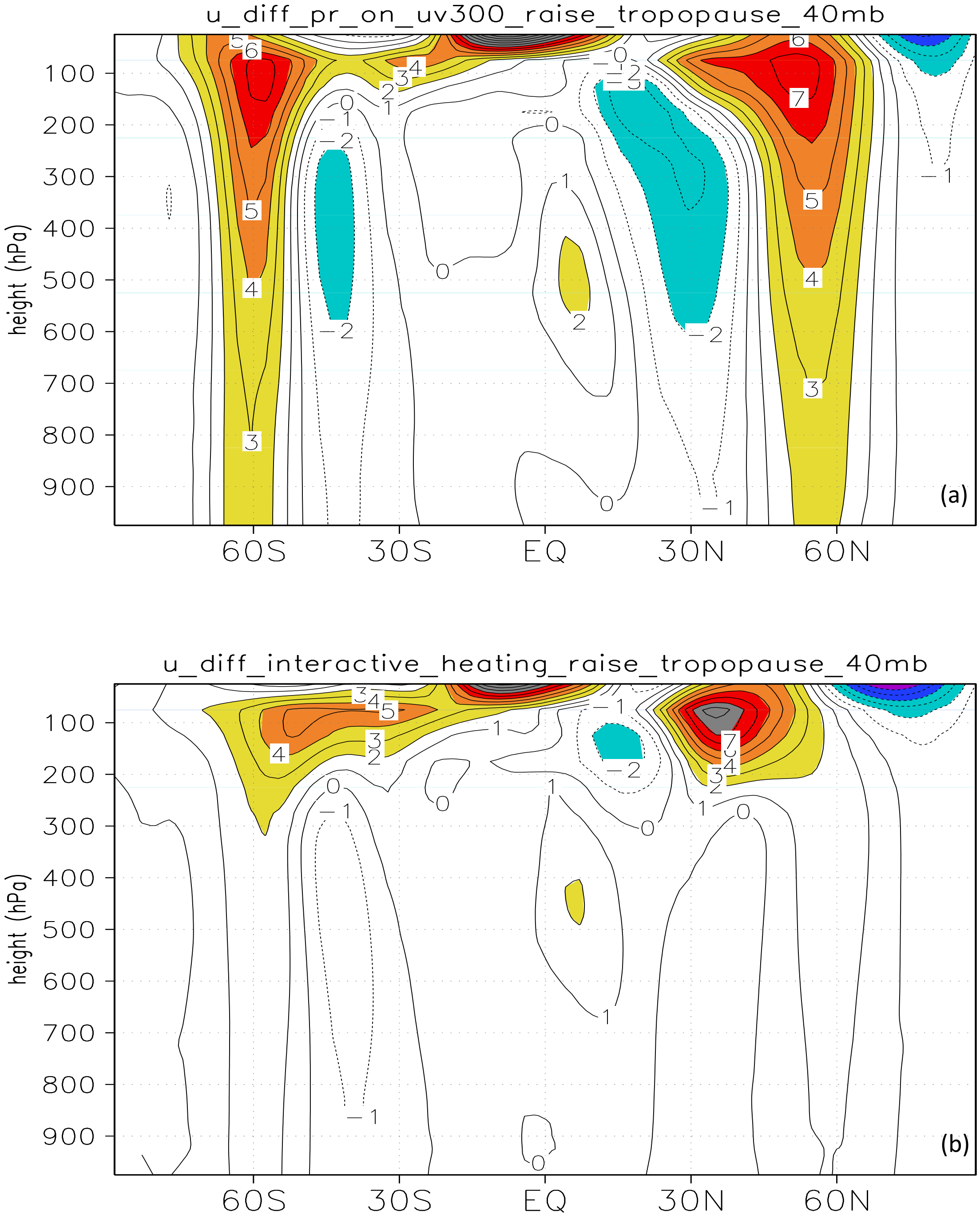

Figure 5.16: Zonal mean zonal wind anomalies between raising tropopause height 40 hPa forcing and control run for experiments of imposing extra diabatic heating. (a) FEEDBACK 1; (b) FEEDBACK 2.

Chapter 6 Conclusions and future work

6.1 Conclusions

In order to explore the reasons responsible for the projected poleward shift of the mid-latitude jets and storm tracks under global warming found in IPCC AR4 simulations, we have investigated several related problems by diagnosing observations, reanalysis data and model output from GCMs, as well as by performing numerical experiments using an idealized dry model. Here, the major conclusions based on this dissertation can be summarized by answering these questions raised in the introduction (Chapter 1).

i. Can we trust the mid-latitude jet variability and shift in the prediction of IPCC AR4 multi-model simulations? How well do the models simulate the mean state and its variability, and are the transient eddies and their variability captured well? How about the relationship between the eddies and the mean flow?

In this study, the quality of the 20th Century climate simulations made by IPCC AR4 coupled GCMs (total 28 runs from 18 models) has been examined by comparing with reanalysis data. The results suggest that the IPCC AR4 models have larger variability in both the mean flow and storm track than an old run made using the GFDL-R30 model, with the improvement being more significant for the eddy momentum fluxes. In a previous study (Reichler and Kim 2008), the significant improvement of the latest CMIP-3 generation compared to its predecessors in terms of the time-mean state of climate has been noted. In our study, apart from the improvement of mean flow variability, substantial improvements in the transient eddy variability have also been found. These improvements in the variance might be partly due to more sophisticated model parameterizations and general increase in computational resources which allow for higher model resolution.

Because of the large amount of available satellite data assimilated into the reanalysis data after 1979, we expect the reanalysis to exhibit improvements in the period after the satellite in terms of smaller biases, especially in regions with few in situ observations. Thus the NCEP reanalysis after satellite is used as a benchmark. We found that for individual mean flow field or the storm track variability, results based on the IPCC AR4 model outputs are mostly clustered around that based on the reanalysis before satellite. This suggests that the uncertainty of these coupled models in simulating either low-frequency mean flow or transient eddy variability might be at the similar level with the uncertainty of the reanalysis data before satellite relative to that after. The same conclusion is obtained for the SVD analysis studying the interaction between the mean flow and storm track variability since the model outputs and reanalysis before satellite are also clustered together. We believe that the pre-satellite reanalysis data in the Northern Hemisphere are of high quality, given the close agreement between the ERA40 and NCEP/NCAR reanalysis data. Thus pretty high confidence could be placed in climate simulation results of these IPCC AR4 coupled models, giving us more confidence on model prediction of the jet variability and shift.

ii. Why do dry model simulations frequently have an abnormal long zonal index autocorrelation timescale compared with that found in GCM simulations? What are the implications of such a deficiency? How can this deficiency be improved?

An idealized dry model (Chang 2006) constructed based on the dynamical core of the GFDL global spectral model (Held and Suarez 1994), has been used in this study. In this dry model simulations, an extremely long jet variability timescale of about 50 days is found, compared with that in CMIP3 GCMs (from 13 to 40 days) and in reanalyses (about 10-13 days). Some previous studies have also suggested this significantly biased long timescale in their idealized dry mechanistic model runs (Yu and Hartmann 1993; Polvani and Kushner 2002; Kushner and Polvani 2004; Gerber and Vallis 2007; Gerber et al. 2008). The major difference between dry models and full GCMs is the lack of moist process in dry models. Therefore, our hypothesis is that the missing diabatic heating due to moist processes in dry models is the most essential reason for having a much longer timescale than that in coupled models.

Regression analyses using reanalysis data and GPCP satellite derived precipitation showed a robust precipitation anomaly associated with the zonal index mode, When time-independent heating is imposed in our dry model based on this precipitation anomaly, the midlatitude jet is found to shift equatorward (poleward) when the extra latent heating imposed is based on poleward (equatorward) shifted eddies and jet. These results suggest that latent heat release based on a north-south shift of the jet will act to suppress this mode, suggesting that diabatic heating provides a negative feedback on mid-latitude jet variability, acting against the effects of eddy momentum forcing.

In a second series of experiments, latent heat forcing with the same structure as that discussed in the paragraph above but with a time varying amplitude based on the eddy momentum flux anomaly (FEEDBACK 1) has been imposed in the model. The results also show that the north-south jet shift mode is suppressed by adding extra latent heat due to the precipitation related with eddies. In another word, the zonal index can be damped by adding an extra diabatic forcing, which gives rise to a negative feedback against the dynamical positive feedback. This is a direct impact of diabatic forcing on zonal index variations. The very long timescale displaying in the dry model has been substantially improved in this experiment. The timescale of the jet shift mode in the extra-heating run is shorter than that of control run (about 35 days by imposing 1 × heating compared with 50 days of control run), and it gets shorter when the stronger heating is imposed (about 25 days by imposing 4 × heating).

Another way to mimic the diabatic heating in a dry model conducted in this study is to use a simple parameterization of the condensational heating in upward motion regions outside of the tropics (FEEDBACK 2). The timescale of SH zonal index is significantly reduced to around 17 days in this experiment, with the reduction more than that found in experiments with FEEDBACK 1, and the jet-shift timescale is much closer to that observed. We hypothesize that with this interactive heating, over regions where there is upward motion, the warm regions get warmer, making eddies more enhanced. Under such a circumstance, the system will become more chaotic, causing the timescale to be further reduced. This indirect impact of heating acts on top of the direct impact of diabatic heating discussed in the preceding paragraph. We believe that this is the reason why the timescale by adding FEEDBACK 2 is reduced more compared with that found in experiments using FEEDBACK 1.

Therefore, we conclude that the extra diabatic forcing provides a negative feedback on the zonal index variations, reducing the jet variability timescale. The biased long timescale found in dry models can be improved by imposing heating to mimic the diabatic feedback in the model. It can even be reduced close to that observed by using an interactive heating in dry models. Based on the recent application of the fluctuation-dissipation theorem in atmospheric sciences research, the model response due to external forcing is likely proportional to the de-correlation timescale of the model climate system. Thus, such a long timescale in the dry model could give rise to the possibility of an overly sensitive model response to imposed forcing.

iii. Based on the ensemble mean temperature change found in the IPCC AR4 model global warming prediction, several hypotheses have been suggested to explain the projected jet and storm track shift. What are the most important reasons for the poleward shift of the jets in our modeling study? Does the model response depend on the autocorrelation time scale of the zonal index mode? What are the implications of such a dependence?

Three hypotheses which could be responsible for the poleward shift of projected jets and storm track under global warming found in IPCC AR4 prediction, namely the change of meridional temperature gradient near the tropopause, the change in static stability, and the tropopause height rise, have been examined in the last part of this dissertation. Similar to the previous studies, an idealized dry mechanistic model – which is often used to understand how the mid-latitude jets respond to changes in diabatic heating under global warming – is applied in this study. But differing from their idealized experiments driven by forcings with idealized context, we make use of the temperature anomalies calculated from the IPCC AR4 prediction which is similar to the earth's atmosphere to obtain different global warming forcings. And another novel part of this study compared with previous dry modeling work is that we have explored the model response with the reasonable jet variability timescale when the diabatic feedback is imposed in the dry model.

In the first set of experiments, we find that the anomalies of horizontal temperature gradient near the tropopause, caused by warming in the troposphere and cooling in the lower stratosphere under global warming, are strongly essential to the jets shift. Regarding static stability, our experiments suggest that the change in global static stability forcing is entirely unimportant, leading to almost no wind response. Experiments also find that the localized static stability change has some impact on jets shift, but it is much weaker than the influence of temperature gradient anomalies. This result is consistent with those of Butler et al. (2010). For each experiment we conducted three cases, jet responses in dry runs, in experiments with FEEDBACK 1 and with FEEDBACK 2, and the responses in the last two cases are always weaker than that in dry runs. The case with FEEDBACK 2 resembles the results in IPCC GCMs most. This is expected based on the fluctuation-dissipation theorem, because the timescale of jet variability in experiments with diabatic feedback has been reduced, especially the one with FEEDBACK 2 is closest to that found in GCMs.

The temperature gradient only forcing then has been separated into two parts, one above 500 hPa, the other below. We find that the response driven by the upper level forcing is much stronger than the response at lower level, suggesting that the thermal forcing under global warming near the surface has much less important effect on the jet shift mode than that near the tropopause. However this result is different from those found in some previous studies (Held and Brien 1992; Geng and Sugi 2003; Yin 2005; Lu et al. 2008; Deser et al. 2010) which suggested that the jet shift was very sensitive to the lower level baroclinicity. This could be an interesting topic to follow up in future studies.

The third set of experiments we conduct is to assess the importance of the tropopause height rise to the jet shift under global warming. When we raise the tropopause uniformly at all latitudes by 20 hPa, the mid-latitude jets shift poleward a little; when it is raised by 40 hPa, jets move further poleward by almost twice the amount. But the jet response to a 40 hPa rise of tropopause height is still slightly weaker than that due to the full forcing in both dry runs and experiments with diabatic feedback, especially in the SH. This suggests that more than 40 hPa of tropopause height rise is needed to attain the same jet shift as that achieved by the full forcing. In addition we find that over 40 hPa tropopause height rise is needed for the experiments with FEEDBACK 2 to produce the amount of jet shift found in IPCC AR4 experiments. This suggests that a 400m of tropopause height rise (equivalent to about 15 hPa rise in the midlaitude tropopause), which was suggested by Lorenz and DeWeaver (2007) to be the projected tropopause lift in IPCC AR4 experiments, is far from being able to account for the magnitude of jet shift found in GCMs simulations.

Therefore from the results of our experiments, we conclude that the temperature gradient change near the tropopause is the most important factor responsible for the jet poleward shift, followed by the tropopause height rise. The static stability change is not important.

For all the experiments we have conducted, the magnitude of jet shift found in experiments with diabatic feedback is always smaller, with the results from FEEDBACK 2 resembling those found in IPCC GCMs most. It is consistent with the expectation based on the shorter autocorrelation timescale of the zonal index mode found in experiments with diabatic feedback incorporated. Therefore, we hypothesize that the results of many previous studies (e.g., Haigh et al. (2005); Lorenz and DeWeaver (2007); Simpson et al. (2009); Butler et al. (2010, 2011)) using dry mechanistic models similar to our dry model are likely biased due to their models being too sensitive to imposed forcing because of a long zonal index timescale.

6.2 What are novel in this dissertation?

In this section, we’d like to summarize what are novel in this dissertation.

i. The quality of the IPCC AR4 climate simulations has been assessed in terms of not only the mean flow but also the variability of the mean flow and storm track, and their relationship as well. Results suggest the most new generation of models have larger variance than the old ones, and the uncertainty of IPCC AR4 models in simulating either low-frequency mean flow or transient eddy variability might be at the similar level with the uncertainty of the reanalysis data before satellite relative to that after.

ii. We find that the diabatic forcing has a negative feedback on the zonal index (jet shift) mode which is similar to the effect of eddy heat flux. The abnormally long jet variability timescale found in dry models can be substantially reduced by imposing extra diabatic feedback, and can even be improved to become close to the timescale found in IPCC AR4 simulations or observations (case with FEEDBACK 2).

iii. By imposing the global warming forcing which is close to the earth's atmosphere change, even a 40 hPa rise of the tropopause height has been found to be not sufficient to support the magnitude of jet shift found in the IPCC AR4 GCM simulations in experiments with FEEDBACK 2, which is different from what suggested by Lorenz and DeWeaver (2007). They showed a 400m rise (which is equivalent to about 15 hPa) of the tropopause height due to global warming in IPCC AR4 experiments, and suggested that such a tropopause rise resulted in poleward shift of jets in their idealized experiments that is comparable to that found in IPCC GCMs. Therefore, we conclude that the tropopause height rise likely only can play a secondary role, the change of meridional temperature gradient near the tropopause is the most important factor.

iv. In this study, we discover that the jet responses are strongest in dry model runs in which the jet variability timescale is longest, and they become weaker when diabatic feedback is imposed reducing the timescale. The jet response in experiment with FEEDBACK 2, which has zonal index timescale closest to those found in CIMP3 GCM simulations, resembles that found in IPCC AR4 simulations most. This is consistent with the fluctuation-dissipation theorem: the model response is proportional to the timescale of system. Our results imply that for those previous studies examining jet shift response based on dry models similar to ours (e.g., Haigh et al. 2005; Lorenz and DeWeaver 2007; Simpson et al. 2009; and Butler et al. 2010, 2011), results should be reassessed to see if the model response is overly sensitive to the diabatic forcing due to a long zonal index timescale.

6.3 Future work

In this section, several possible extensions of this dissertation are discussed.

For the work that has been done in chapter 3, we have examined the quality of IPCC AR4 (CMIP3) model outputs, while recently the latest dataset of IPCC AR5 (CMIP5) model outputs have been released, it is of interest to assess this newest one to see if there are substantial improvements. If there are, in which aspects? We could pick one or two models to do the diagnostic analysis. Based on the difference between two generations of GCMs, it is possible and meaningful to tell what could lead to the improvement of variability in terms of mean-state climate or the transient eddies. Apart from this, it would be of interest to investigate the large differences that we found among different individual runs of one model in terms of mean flow or transient eddy variability.

In Chapter 4, it is found that the timescale of the Southern Hemisphere zonal index has been substantially reduced by imposing FEEDBACK 1 in our dry model, and it has been further reduced by adding FEEDBACK 2. The case with FEEDBACK 1 has a direct effect on jet shift mode, while the one with FEEDBACK 2 has two, the direct and indirect effects, on the zonal index. In two ways, the jet variability timescale is further reduced with FEEDBACK 2 involved. Thus, a question here is that which effect, the direct or the indirect, has more impact on the zonal index variability. It is of interest trying to separate these two effects of the diabatic feedback on timescale variations to examine how much contribution on the zonal index variations for each one.

Gerber and Vallis (2007) suggested that the timescale of the annular mode could be improved by increasing the model spatial resolution, adding asymmetries such as topography, or adjusting model parameters such as the momentum and thermal damping. The timescale can also be improved by increasing the amplitude of the stratospheric wave drag and variability (e.g., Norton 2003). It will be interesting if we can test these factors, which can improve the long timescale found in dry models, in our idealized model to see which one is most efficient, the diabatic feedback, the model resolution or the asymmetries. Meanwhile analyzing the jet variability timescale in the Northern Hemisphere can be an easiest and most direct way to see the influence of zonal asymmetries. It would be of great interests to come up with new ideas concerning how these various factors improve the jet variability timescale individually.

In Chapter 5, the meridional temperature gradient change near the tropopause due to global warming is found to be more important to the poleward shift of mid-latitude jets than the tropopause height rise. Chen et al. (2007) and Chen and Held (2007) suggested that the increased zonal winds increases the phase speeds of eddies near the tropopause or in the lower stratosphere, resulting in a poleward shift of jet and eddies. This wind increase is contributed by the increased temperature gradient near the tropopause. However our forcing involves not only enhancing the temperature gradient neat the tropopause, but also acts to raise the tropopause because of additional tropical warming. So how about the mechanism of the tropopause rise? It is of great interest to isolate the temperature changes caused by tropopause height rise from those due to radiative forcings. Or is it even meaningful to ask such a question? These are what we want to further investigate in the future work.

Bibliography

Adler, R. F., Huffman, G. J., Chang,A., Ferraro, R., Xie, P., Janowiak, J., Rudolf, B., Schneider, U., Curtis, S., Bolvin, D., Gruber, A., Susskind, J., Arkin, P. and Nelkin, E., 2003: The Version-2 Global Precipitation Climatology Project (GPCP) monthly precipitation analysis (1979–present). J. Hydrometeorol., 4, 1147–1167.

Annamalai, H., J. M. Slingo, K. R. Sperber, and K. Hodges, 1999: The mean evolution and variability of the Asian summer monsoon: Comparison of ECMWF and NCEP–NCAR reanalyses. *Mon. Wea. Rev.*, **127,** 1157–1186.

Barnes, E. A. and D. L. Hartmann, 2010d: Influence of eddy-driven jet latitude on North Atlantic jet persistence and blocking frequency in CMIP3 integrations. *J. Geophys. Res*., Vol. **37**, L23802, doi: 10.1029/2010GL045700.

Barnes, E. A. and D. L. Hartmann, 2011: Rossby-wave scales, propagation and the variability of eddy-driven jets. *J. Atmos. Sci.*, **68**, 2893–2908.

——, and L. M. Polvani, 2012: Response of the midlatitude jets and of their variability to increased greenhouse gases in the CMIP5 models. *J. Climate*, submitted.

Becker, E., and G. Schmitz, 2001: Interaction between extratropical stationary waves and the zonal mean circulation. *J. Atmos. Sci*., **58**, 462-480.

Bell, L. Thomas, 1980: Climate sensitivity from fluctuation dissipation: some simple model tests. *J. Atmos. Sci*., **37**, 1700-1707.

Blackmon, M. L., 1976: A climatological spectral study of the 500 mb geopotential height of the Northern Hemisphere. *J. Atmos.Sci.,* **33,** 1607–1623.

——, J. M. Wallace, N.-C. Lau, and S. L. Mullen, 1977: An observational study of the Northern Hemisphere wintertime circulation. *J. Atmos. Sci.,* **34,** 1040–1053.

Boville, B., 1991: Sensitivity of simulated climate to model resolution. *J. Climate*, **4**, 469-485.

Bretherton, C. S., C. Smith, and J. M. Wallace, 1992: An intercomparison of methods for finding coupled patterns in climate data. *J. Climate*., **5**, 541-560.

Branstator, G., 1992: The maintenance of low-frequency anomalies. *J. Atmos. Sci.,* **49,** 1924–1945.

——, 1995: Organization of the storm track anomalies by recurring low-frequency circulation anomalies. *J. Atmos. Sci.,* **52,** 207–226.

Butler, A. H., D. W. J. Thompson, and R. Heikes, 2010: The steady-state atmospheric circulation response to climate-like thermal forcings in a simple general circulation model. *J. Climate*, **23**, 3474-3496.

——, D. W. J. Thompson, and T. Birner, 2011: Isentropic Slopes, Downgradient Eddy Fluxes, and the Extratropical Atmospheric Circulation Response to Tropical Tropospheric Heating. *J. Atmos. Sci.*, **68**, 2292–2305.

Chan, C. J., and R. A. Plumb, 2009: The response to stratospheric forcing and its dependence on the state of the troposphere. *J. Atmos. Sci*., **66**, 2107–2115.

Chang, K. M. Edmund, 2001: GCM and observational diagnoses of the seasonal and interannual variations of the Pacific storm track during the cool season. *J. Atmos. Sci*., **58**, 1784-1800.

——, 2004: Are the Northern Hemisphere winter storm tracks significantly correlated? *J. Climate*, **17**, 4230-4244.

——, 2006: An idealized nonlinear model of the Northern Hemisphere winter storm tracks. *J. Atmos. Sci.*, **63,** 1818–1839.

——, and Y. Fu, 2002: Inter-decadal variations in Northern Hemisphere winter storm track intensity. *J. Climate*, **15**, 642-658.

——, and ——, 2003: Using Mean flow change as a proxy to infer interdecadal storm track variability. *J. Climate*, **16**, 2178-2196.

——, and S. Song, 2006: The seasonal cycles in the distribution of precipitation around cyclones in the western North Pacific and Atlantic. *J. Atmos. Sci*., **63**, 815-839.

——, and P. Zurita-Gotor, 2007: Simulating the seasonal cycle of the Northern Hemisphere storm tracks using idealized nonlinear storm-track models. *J. Atmos. Sci*., **64**, 2309-2331.

——, S. Lee, and K. L. Swanson, 2002: Storm track dynamics. *J.Climate*, **15,** 2163–2183.

Chen, G. and I. M. Held, 2007: Phase speed spectra and the recent poleward shift of Southern Hemisphere surface westerlies. *Geophys. Res. Lett*., **34**, L21805, doi: 10.1029/2007GL031200.

——, and R. A. Plumb, 2009: Quantifying the eddy feedback and persistence of the zonal index in an idealized atmospheric model. *J. Atmos. Sci*., **66**, 3707-3720.

——, I. M. Held, and W. A. Robinson (2007), Sensitivity of the latitude of the surface westerlies to surface friction, *J. Atmos. Sci*., **64**, 2899– 2915.

Deser, C., A. S. Phillips, and M. A. Alexander, 2010: Twentieth century tropical sea surface temperature trends revisited. *Geophys. Res. Lett.,* **37**, L10701, doi: 10.1029/2010GL043321.

Dymnikov, V. P., and S. K. Filin, 1985: A study of the correlations between sea-surface temperature anomalies in mid-latitudes and anomalies in heating, based on data from the First GARP Global Experiment. Reprint of the Department of Numerical Mathematics of the U.S.S.R. Academy of Sciences. [Available from Leninskij Prosp., 14; 117901 Moscow B-71.]

Engelen, R. J., I. L. Wittmeyer, and G. L. Stephens, 1998: Assessment of reanalysis hydrology and energy budgets: Water vapour and radiative fluxes. *Proc. First Int. WCRP Conf. on Reanalysis,*Silver Springs, MD, WCRP-104, WMO/TD-876, 175–178.

Feldstein, S. B., 1998: An observational study of the intraseasonal poleward propagation of zonal mean flow anomalies. *J. Atmos. Sci*., **55**, 2516-2529.

——, 2000a: Is interannual zonal mean flow variability simply climate noise? *J. Climate*, **13,** 2356–2362.

Feldstein, S. B., and S. Lee, 1996: Mechanisms of zonal index variability in an aquaplanet GCM. *J. Atmos. Sci.*, **53,** 3541–3555.

——, and ——, 1998: Is the atmospheric zonal index driven by an eddy feedback? *J. Atmos. Sci.,* **55,** 3077–3086.

——, and W. A. Robinson, 1994: Comments on “Spatial structure of ultra-low frequency variability of the flow in a simple atmospheric circulation model.” *Quart. J. Roy. Meteor. Soc.*, **120,** 739–745.

Frierson, D. M. W., I. M. Held and P. Zurita-Gotor, 2006: A gray-radiation aquaplanet moist GCM. Part I: Static stability and eddy scale. *J. Atmos. Sci*., **63**, 2548-2566.

Fyfe, J.C., 2003: Extratropical Southern Hemisphere cyclones: Harbingers of climate change? *J. Climate*, **16**, 2802-2805.

Geng, Q. and M. Sugi, 2003: Possible change of extratropical cyclone activity due to enhanced greenhouse gases and sulfate aerosols-study with a high-resolution AGCM. *J. Climate*., **16**, 2262-2274.

Gerber, E. P., and G. K. Vallis, 2005: A stochastic model for the spatial structure of annular patterns of variability and the North Atlantic Oscillation. *J. Climate*, **18,** 2102–2118.

——, and ——, 2007: Eddy–zonal flow interactions and the persistence of the zonal index. *J. Atmos. Sci*., **64**, 3296–3311.

——, S. Voronin, and L. Polvani, 2008: Testing the annular mode autocorrelation time scale in simple atmospheric general circulation models. *Mon. Wea. Rev*., **136**, 1523–1536.

Guo, Y., and E. K. M. Chang, 2010: Have the Southern Hemisphere storm tracks been strengthening after 1979? (In submission to *Climate Dynamics*)

Haigh, J. D., M. Blackburn and R. Day, 2005: The response of tropospheric circulation to perturbations in lower-stratospheric temperature. *J. Climate*., **18**, 3672-3685.

Hartmann, D. L., 1974: Time spectral analysis of mid-latitude disturbances. *Mon. Wea. Rev.*, **102,** 348–362.

——, 1995: A PV view of the zonal flow vacillation *J.Atmos. Sci.,* **52,** 2561–2576.

——, and F. Lo, 1998: Wave-driven zonal flow vacillation in the Southern Hemisphere. *J. Atmos. Sci.,* **55,** 1303–1315.

Held, I. M., 1993: Large-scale dynamics and global warming. *Bull. Amer. Meteorol. Soc.*, **74**, 228-241.

——, 2000: The general circulation of the atmosphere. *Proc. Program in Geophysical Fluid Dynamics*. Woods Hole Oceanographic Institution, Wood Hole, MA. http://gfd.whoi.edu/proceedings/2000/PDFvol2000.html

——, and A. Y. Hou, 1980: Nonlinear axially symmetric circulations in a nearly inviscid atmosphere. *J. Atmos. Sci*., **37**, 515-533.

Held, I. M. and E. O'Brien, 1992: Quasigeostrophic turbulence in a three-layer model: effects of vertical structure in the mean shear. *J. Atmos. Sci.*, **49**, 1861-1870.

——, and M. J. Suarez, 1994: A proposal for the intercomparison of dynamical cores of atmospheric general circulation models. *Bull. Amer. Meteor. Soc*., **75**, 1825-1830.

Hoskins, B. J., I. N. James, and G. H. White, 1983: The shape, propagation and mean-flow interaction of large-scale weather systems. *ibid*, **40**, 1595-1612.

Huffman G. J., Coauthors, 1997: The Global Precipitation Climatology Project (GPCP) combined precipitation datasets. *Bull. Amer. Meteor. Soc*., **78**, 5–20.

——,R. F. Adler, M. M. Morrissey, S. Curtis, R. Joyce, B. Mc-Gavock, and J. Susskind, 2001: Global precipitation at one-degree daily resolution from multisatellite observations. *J.Hydrometeor.,* **2,** 36–50.

Jakob, C. 1999: Cloud cover in the ECMWF reanalysis. *J. Climate*, **12**, 947-959.

Kageyama, M., P. J. Valdes, G. Ramstein, C. Hewitt, and U. Wyputta, 1999: Northern Hemisphere storm tracks in present day and last glacial maximum climate simulations: a comparison of the European PMIP models. *J. Climate*, **12**, 742-760.

Kalnay, E., and coauthors, 1996: The NCEP/NCAR 40-year reanalysis project. *Bull. Amer. Meteorol. Soc.*, **77**, 437-471.

Karoly, D. J., 1990: The role of transient eddies in low-frequency zonal variations of the Southern Hemisphere. *Tellus,* **42A,** 41–50.

Kellogg, W. William, 1991: Response to skeptics of global warming. *Bulletin of the Atmos. Meteo. Soc.,* Vol. **72**, Issue 4, **499-511**.

Kidson, J. W., 1985: Index cycles in the Northern Hemisphere during the Global Weather Experiment. *Mon. Wea. Rev.,* **113,** 607–623.

——, 1986: Index cycles in the Southern Hemisphere during the Global Weather Experiment. *Mon. Wea. Rev.*, **114,** 1654–1663.

——, 1988: Indices of the Southern Hemisphere zonal wind. *J.Climate*, **1,** 183–194.

——, and M. R. Sinclair, 1995: The influence of persistent anomalies on Southern Hemisphere storm tracks. *J. Climate*, **8**, 1938-1950.

Kidston, J., and E. P. Gerber, 2010: Intermodel variability of the poleward shift of the austral jet stream in the CMIP3 integrations linked to biases in 20th century climatology. *Geophys. Res. Lett.,* **37,** L09708, doi: 10.1029/2010GL042873.

Kistler, R., and coauthors, 2001: The NCEP-NCAR 50-year reanalysis: Monthly means CD-ROM and documentation. *Bull. Amer. Meteorol. Soc*., **82**, 247-267.

Kushner, P. J., I. M. Held, and T. L. Delworth, 2001: Southern Hemisphere atmospheric circulation response to global warming. *J. Climate*, **14**, 2238-2249.

Kushner, P. J., and L. Polvani, 2004: Stratosphere–troposphere coupling in a relatively simple AGCM: The role of eddies. *J. Climate*, **17**, 629–639.

——, I. M. Held, and T. L. Delworth, 2001: Southern Hemisphere atmospheric circulation response to global warming, *J. Climate,* **14**, 2238–2249.

Lanzante, J. R., 1984: A rotated eigenanalysis of the correlation between 700-mb heights and sea surface temperatures in the Pacific and Atlantic. *Mon. Wea. Rev.*, **112**, 2270-2280.

Lau, N. C., 1988: Variability of the observed midlatitude storm tracks in relation to low-frequency changes in the circulation pattern. *J. Atmos. Sci.,* **45**(19), 2718-2743.

Lee, S., and S. B. Feldstein, 1996: Mechanisms of zonal index evolution in a two-layer model. *J. Atmos. Sci.,* **53,** 2232–2246.

Leith, C. E., 1975: Climate response and fluctuation dissipation. *J. Atmos. Sci*., **32**, 2022–2026.

Lim, E.-P., and I. Simmonds, 2008: Effect of tropospheric temperature change on the zonal mean circulation and SH winter extratropical cyclones. *Climate Dyn*., **33**, 19–32, doi:10.1007/s00382-008-0444-0.

Limpasuvan, V., and D. L. Hartmann, 1999: Eddies and the annular modes of climate variability. *Geophys. Res. Lett.,* **26,** 3133–3136.

——, and ——, 2000: Wave-maintained annular modes of climate variability. *J. Climate,* **13,** 4414–4429.

Lorenz, D. J., and D. L. Hartmann, 2001: Eddy–zonal flow feedback in the Southern Hemisphere. *J. Atmos. Sci.,* **58,** 3312–3327.

——, and E. T. DeWeaver, 2007: Tropopause height and zonal wind response to global warming in the IPCC scenario integrations. *J. Geophys. Res*., **112**, D10119, doi: 10.1029/2006JD008087.

Lu, J., G. Chen, and D. M. W. Frierson, 2008: Response of the zonal mean atmospheric circulation to El Nino versus global warming. *J. Climate*, **21**, 5835-5851.

Manabe, S., 1998: Study of global warming by GFDL climate models. *Ambio,* **27,** 182–186.

——, R. J. Stouffer, M. J. Spelman, and K. Bryan, 1991: Transient response of a coupled ocean–atmosphere model to gradual changes of atmospheric CO2. Part I: Annual mean response. *J. Climate,* **4,** 785–818.

——, M. J. Spelman, and R. J. Stouffer, 1992: Transient response of a coupled ocean–atmosphere model to gradual changes of atmospheric CO2. Part II: Seasonal response. *J. Climate,* **5,** 105–126.

Metz, W., 1989: Low-frequency anomalies of atmospheric flow and the effects of cyclone-scale eddies: A canonical correlation analysis. *J. Atmos. Sci.,* **46,** 1026–1041.

Michaels, J. Patrick, 1992: Global warming: A reduced threat? *Bulletin of the Atmos. Meteo. Soc.*, Vol. **73**, Issue 10, **1563-1577**.

Nakicenovic, N., and R. Swart, 2000: Special report on emissions scenarios. *Cambridge University Press,* Cambridge

Newman, M., P. D. Sardeshmukh, and J. W. Bergman, 2000: An assessment of the NCEP, NASA, and ECMWF reanalyses over the tropical west Pacific Warm Pool. *Bull. Amer. Meteor. Soc.,* **81,** 41–48.

Nigam, S., 1990: On the structure of variability of the observed tropospheric and stratospheric zonal-mean zonal wind. *J. Atmos.Sci.,* **47,** 1799–1813.

——, C. Chung, and E. DeWeaver, 2000: ENSO Diabatic Heating in ECMWF and NCEP Reanalyses, and NCAR CCM3 Simulation. *J. Climate,***13,** 3152-3171.

Norton, W. A., 2003: Sensitivity of the Northern Hemisphere surface climate to simulation of the stratospheric polar vortex. *Geophys. Res. Lett*., **30**, 1627, doi:10.1029/2003GL016958.

Polvani, L. M., and P. J. Kushner, 2002: Tropospheric response to stratospheric perturbation in a relatively simple general circulation model. *Geophys. Res. Lett.,* **29,** L18701, doi: 10.1029/2001GL014284.

Prohaska, F., 1976: The climate of Argentina, Paraguay and Uruguay. Pp. 57-69. In: Schwerdtfeger, E. (ed.) Climate of central and south America. World survey of climatology. Elsevier, Amsterdam.

Randel, W. J., and J. L. Stanford, 1985: An observational study of medium-scale wave dynamics in the Southern Hemisphere summer. Part I: Wave structure and energetics. *J. Atmos. Sci.,* **42,** 1172–1188.

Reichler, T., and J. Kim (2008): How well do coupled models simulate today's climate? *Bull. Amer. Meteor. Soc.*, **89**, 303-311.

Ring, M. J., and R. A. Plumb, 2007: Forced annular mode patterns in a simple atmospheric general circulation model. *J. Atmos. Sci*., **64**, 3611–3626.

——, and ——, 2008: The response of a simplified GCM to axisymmetric forcings: Applicability of the fluctuation–dissipation theorem. *J. Atmos. Sci*., **65**, 3880–3898.

Robinson, W., 1991: The dynamics of the zonal index in a simple model of the atmosphere. *Tellus,* **43A,** 295–305.

——, 1994: Eddy feedbacks on the zonal index and eddy-zonal flow interactions induced by zonal flow transience. *J. Atmos. Sci*., **51**, 2553-2562.

——, 1996: Does eddy feedback sustain variability in the zonal index? *J. Atmos. Sci.,* **53,** 3556–3569.

——, 2006: On the self-maintenance of midlatitude jets. *J. Atmos. Sci.,* **63,** 2109–2122.

Senior, C. A., 1995: The dependence of climate sensitivity on the horizontal resolution of a GCM. *J. Climate*, **8**, 2860-2880.

Sheng, J., J. Derome, M. Klasa, 1998: The role of transient disturbances in the dynamics of the Pacific-north American pattern. *J. Climate*, **11**, 523-536.

Shiotani, M., 1990: Low-frequency variation of the zonal mean state of the southern-hemisphere troposphere. *J. Met. Soc. Japan*, **68**(4), 461-471.

Simpson, I. R., M. Blackburn, and J. D. Haigh, 2009: The role of eddies in driving the tropospheric response to stratospheric heating perturbations. *J. Atmos. Sci*., **66**, 1347–1365.

Son, S., and Coauthors, 2008: The impact of stratospheric ozone recovery on the Southern Hemisphere westerly jet. *Science*, **320**, 1486–1489.

Stendel, M., and K. Arpe, 1997: Evaluation of the rhydological cycle in reanalyses and observations. Max-Planck-Institut fur Meteorologie Rep. 228, 52 pp. [Available from Max-Planck-Institut fur Meteorologie, Bundesstrasse 55, 20147 Hamburg, Germany.]

Taylor, K. E., 2001: Summarizing multiple aspects of model performance in a single diagram. *J. Geophys. Res.,* **106**, No. D7, P. 7183, doi: 10.1029/2000JD900719.

Ting, M., and N. –C. Lau, 1993: A diagnostic and modeling study of the monthly mean wintertime anomalies appearing in a 100-year GCM experiment. *J. Atmos. Sci*., **50**, 2845-2867.

Trenberth, K. E., 1981a: Interannual variability of the Southern Hemisphere 500 mb flow: regional characteristics. *Mon. Wea. Rev*., **109**, 127-136.

——, 1981b: Observed Southern Hemisphere eddy statistics at 500 mb: frequency and spatial dependence. *J. Atmos. Sci*., **38**, 2585-2605.

——, 1982: Seasonality in Southern Hemisphere eddy statistics at 500 mb. *J. Atmos. Sci.*, **39**, 2507-2520.

——, and C. J. Guillemot, 1998: Evaluation of the atmospheric moisture and hydrogical cycle in the NCEP/NCAR reanalyses. *Climate Dyn.*, **14,** 213–231.

——, D. P. Stepaniak, J. W. Hurrell, and M. Fiorino, 2001: Quality of Reanalyses in the Tropics. *J. Climate*, **14,** 1499-1510.

Uppala, S.M., P.W. Kallberg, A.J. Simmons, U. Andrae, V. da Costa Bechtold, M. Fiorino, J.K Gibson, J. Haseler, A. Hernandez, G.A. Kelly, X. Li, K. Onogi, S. Saarinen, N. Sokka, R.P. Allan, E. Andersson, K. Arpe, M.A. Balmaseda, A.C.M. Beljaars, L. van de Berg, J. Bidlot, N.Bormann, S. Caires, F. Chevallier, A. Dethof, M. Dragosavac, M. Fisher, M. Fuentes, S. Hagemann, E. Hólm, B.J. Hoskins, L. Isaksen, P.A.E.M. Janssen,

R. Jenne, A.P. McNally, J.-F. Mahfouf, J.- J. Morcrette, N.A Rayner, R.W. Saunders, P. Simon, A. Sterl, K.E. Trenberth, A. Untch, D.Vasiljevic, P. Viterbo and J. Woollen 2005: The ERA-40 reanalysis. *Quart. J. Roy. Meteor. Soc*., **131**, 2961-3012.

Wallace, J.M., and D. S. Gutzler, 1981: Teleconnections in the geopotential height field during the Northern Hemisphere winter. *Mon. Wea. Rev.*, **109**, 784-812.

——, G.H. Lim, and M.L. Blackmon, 1988: Relationship between cyclone tracks, anticyclone tracks, and baroclinic waveguides. *J. Atmos. Sci.,* **45**, 439-462.

——, C. Smith, and C. S. Bretherton, 1992: Singular value decomposition of wintertime sea surface temperature and 500-mb height anomalies. *J. Climate,* **5**, 561-576.

Williams, G. P., 2006: Circulation sensitivity to tropopause height, *J. Atmos. Sci*., **63**, 1954– 1961.

Yang, X., and E. K. M. Chang, 2006: Variability of the Southern Hemisphere winter split flow—A case of two-way reinforcement between mean flow and eddy anomalies. *J. Atmos. Sci.,* **63,** 634–650.

——, and ——, 2007: Eddy-zonal flow feedback in the Southern Hemisphere winter and summer. *J. Atmos. Sci*., **64**, 3091-3112.

Yin, J. H., 2005: A consistent poleward shift of the storm tracks in simulations of 21st century climate. *Geophys. Res. Lett.,* **32,** L18701, doi: 10.1029/2005GL023684.

Yu, J. Y., and D. L. Hartmann, 1993: Zonal flow vacillation and eddy forcing in a simple GCM of the atmosphere. *J. Atmos.Sci.,* **50,** 3244–3259.